University of Lille

Faculty of Sciences and Technologies

Doctoral School 104 – Science of the Matter, of the Radiation, and of the Environment

Doctoral Thesis

by

Ana Lícia MOURA GOMES

to obtain the degree of

Doctor of the University of Lille

Discipline: Physical, analytical and theoretical chemistry

Optimization via an ultrafast spectroscopy approach of transparent and colorless dye photovoltaic cells in the visible range

Date of defense: 28 February 2025

Sophie	**FOURMENTIN-LAMOTTE** *Professor, University of Littoral-Côte d'Opale*	**President/Reviewer**
Marco	**PAOLANTONI** *Associate Professor, University of Perugia*	**Reviewer**
François-Alexandre	**MIANNAY** *Associate Professor, University of Lille*	**Supervisor**
Frédéric	**SAUVAGE** *Professor, University of Picardie Jules Vernes*	**Co-supervisor**
Abdenacer	**IDRISSI** *Professor, University of Lille*	**Co-supervisor**
Marie	**CHOËL** *Associate Professor, University of Lille*	**Examiner**
Minh-Huong	**HA-THI** *Associate Professor, Paris-Saclay University*	**Examiner**
Oleg	**KALUGIN** *Professor, Karazin Kharkiv National University*	**Examiner**

Université de Lille

Faculté des sciences et des technologies

École doctorale 104 – Science de la matière, du rayonnement et de l’environnement

Thèse

par

Ana Lícia MOURA GOMES

pour obtenir le degré de

Docteur de l’Université de Lille

Discipline : Chimie physique, analytique et théorique

Optimisation par une approche de spectroscopie ultrarapide des cellules photovoltaïques à colorant transparent et incolore dans la plage visible.

Date de soutenance: 28 Février 2025

Sophie	**FOURMENTIN-LAMOTTE** *Professeur, Université du Littoral-Côte d'Opale*	**Présidente/Rapporteur**
Marco	**PAOLANTONI** *Maître de conférences, Université de Pérouse*	**Rapporteur**
François-Alexandre	**MIANNAY** *Maître de conférences, Université de Lille*	**Directeur de Thèse**
Frédéric	**SAUVAGE** *Professeur, Université de Picardie Jules Vernes*	**Co-directeur de Thèse**
Abdenacer	**IDRISSI** *Professeur, Université de Lille*	**Co-directeur de Thèse**
Marie	**CHOËL** *Maître de conférences, Université de Lille*	**Examinatrice**
Minh-Huong	**HA-THI** *Maître de conférences, Université Paris-Saclay*	**Examinatrice**
Oleg	**KALUGIN** *Professeur, Karazin Université Nationale de Kharkiv*	**Examinateur**

Aknowledgements

This work was carried out at the *Laboratoire de Spectroscopie pour les Interactions, la Réactivité et l'Environnement* (LASIRE) at the *Université de Lille* in partnership with the *Laboratoire de Réactivité et Chimie des Solides* (LRCS). I would like to express my gratitude to both institutions for providing the necessary facilities and resources that allowed me to conduct my research. I am particularly thankful to the University of Lille for the financial support that made this doctoral work possible.

I am sincerely grateful to my supervisor, Prof. François-Alexandre Miannay, for his guidance, patience, and support throughout my research. I am also grateful to Prof. Abdenacer Idrissi and Prof. Frédéric Sauvage for their scientific insights, encouragement, and contributions to my work.

I would like to acknowledge my colleagues and coworkers, Dr. Olena Moskaieva, Dr. Yevheniia Smortsova, Artem Shagurin, and Dr. Fionnuala Grifoni, whose support and collaboration made this journey smoother and more enriching. A special thanks is extended to the administrative staff of LASIRE and LRCS for their continuous assistance, ensuring that everything ran efficiently during my time in the laboratories.

On a personal note, I am forever grateful to my family, especially my parents, siblings, and my husband, whose unwavering love and understanding were my pillars of strength throughout this journey. I also extend my thanks to my friends, whose support and encouragement were invaluable during the ups and downs of this process.

Finally, I would like to express my appreciation to the members of the thesis jury for taking the time to evaluate my work.

Abstract

This thesis covers critical elements of dye-sensitized solar cells (DSSCs), emphasizing the incorporation of transient absorption spectroscopy (TAS) as an important analytical instrument. The work opens with an examination of the photophysical properties of the D205 dye in mixed solvent systems, clarifying the impact of solvent mixture composition on absorption, emission, and relaxation dynamics. The results indicated that D205's activity in ionic liquids closely parallels its behavior in organic solvents, offering significant insights into the influence of solvent environments on DSSC performance.

The present research significantly contributes by developing Python-based TAS program for the analysis of femtosecond transient absorption data. This tool handles issues like group velocity dispersion correction and offers an effective structure for analyzing ultrafast photophysical phenomena. This software effectively evaluated the molecular dynamics of D205 in various solvents, connecting solution-phase investigations with device-level performance.

The research also evaluates the performance of dye-sensitized solar cells (DSSCs) built with innovative dye systems, such as SubPc derivatives and VG20-TBPF. Employing the conventional fabrication technique, VG20-TBPF-based cells demonstrated stable photovoltaic performance, with efficiency enhancements resulting from the incorporation of CDCA. A novel fabrication technique using thinner semiconductor layers and different dye deposition methods was investigated, resulting in highly transparent cells.

Collectively, these findings illustrate the application of TAS in linking molecular level photophysical investigations to device performance, hence improving DSSCs as a sustainable, efficient, and adaptable solar technology. This study establishes a foundation for subsequent research aimed at developing dye-sensitized solar cells (DSSCs) for diverse applications, highlighting the significance of balancing efficiency, transparency, and functionality in photovoltaic technology.

Keywords: Dye-sensitized solar cells, femtosecond spectroscopy, photophysics, ultrafast phenomena, transient absorption spectroscopy (TAS), organic solvents, D205 dye, VG20 dye.

Résumé

Cette thèse traite des éléments clés des cellules solaires sensibilisées par colorant (DSSCs), en mettant l'accent sur l'intégration de la spectroscopie d'absorption transitoire (TAS) comme un outil analytique essentiel. Le travail débute par une étude des propriétés photophysiques du colorant D205 dans des systèmes de solvants mixtes, clarifiant l'impact de la composition des mélanges de solvants sur les dynamiques d'absorption, d'émission et de relaxation. Les résultats montrent que le comportement du D205 dans des liquides ioniques est très similaire à celui observé dans des solvants organiques, offrant des informations précieuses sur l'influence des environnements de solvants sur les performances des DSSCs.

Cette recherche contribue de manière significative au développement d'un programme Python pour l'analyse des données d'absorption transitoire femtoseconde. Cet outil permet de résoudre des problèmes tels que la correction de la dispersion de la vitesse de groupe et offre une structure efficace pour analyser les phénomènes photophysiques ultrarapides. Le logiciel a été utilisé avec succès pour évaluer la dynamique moléculaire du D205 dans divers solvants, établissant un lien entre les études en phase solution et les performances des dispositifs.

La recherche évalue également les performances des cellules solaires sensibilisées par colorant (DSSCs) fabriquées avec des systèmes de colorants innovants, tels que les dérivés de SubPc et VG20-TBPF. En utilisant la technique de fabrication conventionnelle, les cellules basées sur le VG20-TBPF ont démontré des performances photovoltaïques stables, avec des améliorations d'efficacité résultant de l'ajout de CDCA. Une nouvelle technique de fabrication utilisant des couches de semi-conducteurs plus minces et des méthodes alternatives de dépôt de colorants a été explorée, conduisant à la production de cellules hautement transparentes.

En résumé, ces résultats illustrent l'application de la TAS pour établir un lien entre les études photophysiques au niveau moléculaire et les performances des dispositifs, contribuant ainsi à l'amélioration des DSSCs en tant que technologie solaire durable, efficace et adaptable. Cette étude pose les bases de recherches futures visant à développer des cellules solaires sensibilisées par colorant (DSSCs) pour diverses applications, soulignant l'importance d'un équilibre entre efficacité, transparence et fonctionnalité dans les technologies photovoltaïques.

Mots-clés : Cellules solaires à colorant, spectroscopie femtoseconde, photophysique, phénomènes ultra-rapides, spectroscopie d'absorption transitoire (TAS), solvants organiques, colorant D205, colorant VG20.

Table of content

List of Abbreviations

ACN – Acetonitrile

AM – Air Mass 1.5 Global

AVT – Average Visible Transmittance

BIPV – Building-Integrated Photovoltaics

CB – Conduction Band

CDCA – Chenodeoxycholic Acid

CI – Conical Intersection

DAS – Decay-Associated Spectra

DFT – Density Functional Theory

DMII – 1,3-Dimethylimidazolium iodide

DMSO – Dimethyl Sulfoxide

DSSC – Dye-sensitized Solar Cell

ESA – Excited-state Absorption

FE – Full Electrolyte

FF – Fill Factor

FTO – Fluorine-Doped Tin Oxide

FWHM – Full-Width Half Maximum

GSB – Ground-State Bleach

GVD – Group Velocity Dispersion

HOMO – Highest Occupied Molecular Orbital

IL – Ionic liquid

IMPS – Intensity Modulated Photocurrent Spectroscopy

IMVS – Intensity Modulated Photovoltage Spectroscopy

IR – Infrared

IRF – Instrument Response Function

J_{SC} – Short-Circuit Current Density

JV – Current-Density

MPP – Maximum Power Point

MS – Molecular Solvent

NIR – Near-Infrared

NR – Non-Redox Couple

OD – Optical Density

OOP – Object-Oriented Programming

OPV – Organic Photovoltaic

PCE – Power Conversion Efficiency

PK – Perovskite

PV – Photovoltaic

SE – Stimulated Emission

TA – Transient Absorption

TAS – Transient Absorption Spectroscopy

TBPF – Tetrabromophenylfluorone

TCO – Transparent Conducting Oxide

TCSPC – Time-Correlated Single Photon Counting

TD-DFT – Time-Dependent Density Functional Theory

THF – Tetrahydrofuran

UV – Ultraviolet

V_{OC} – Open-Circuit Voltage

List of Figures

General Introduction

The rising worldwide energy demand and the pressing necessity to combat climate change have positioned renewable energy as a priority in scientific and technological advancement. Solar energy, because of its extensive availability and sustainability, presents one of the most promising ways to address these demands. Photovoltaics (PVs) are crucial technologies that efficiently turn sunshine into electricity. Throughout the decades, photovoltaic technology has progressed markedly, transitioning from the initial silicon-based cells to sophisticated third-generation alternatives like dye-sensitized solar cells (DSSCs).

Dye-sensitized solar cells (DSSCs), pioneered by O'Regan and Grätzel in 1991 [1], embody a revolutionary method for solar energy conversion. In contrast to conventional photovoltaics, dye-sensitized solar cells (DSSCs) use molecular dyes to capture sunlight and promote electron transport, allowing for a more adaptable and economical design. This invention has established DSSCs as a significant contributor to renewable energy solutions, especially in areas where conventional silicon-based technologies face limitations. DSSCs are lightweight, semi-transparent, and operate well in diffuse and low-light conditions, rendering them suitable for various contexts, including urban areas and indoor applications.

A notable feature of DSSCs is their potential incorporation into architectural components, including windows and facades, via building-integrated photovoltaics (BIPVs) [2]. In highly populated urban environments, where conventional photovoltaic systems suffer spatial limits, dye-sensitized solar cells (DSSCs) provide a distinct advantage by turning ordinary structures into energy-generating surfaces. Transparent and semi-transparent BIPV modules, exhibiting different levels of light transmission as illustrated in Figure 2. These advancements emphasize the capability of DSSCs to integrate efficiency, sustainability, and contemporary design for urban and commercial uses.

Figure 1. BIPV examples. (a) the Heron Tower, London, UK, (b) the Graz tower in Austria, (c) the dye solar cell façade at SwissTech convention center, Lausanne, Switzerland, and (d) the Bordeaux Botanical Gardens, Jourda, France.

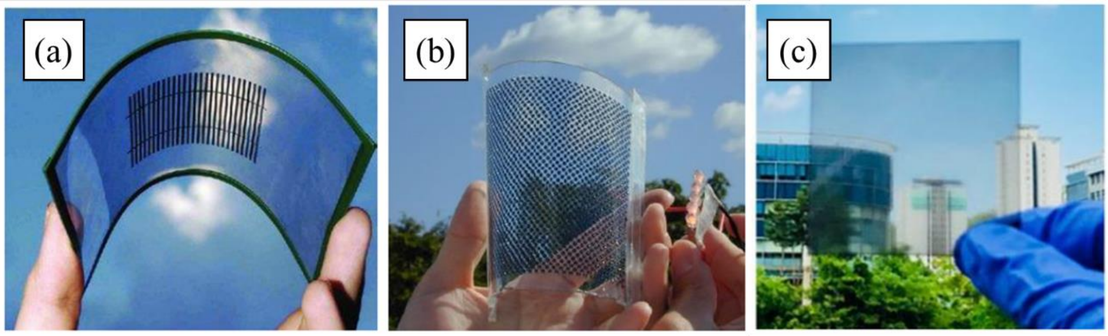

Figure 2. (a) A flexible solar cell module based on spatially segmented silver cells [3]. (b) Sphelar® module based on spherical silicon solar cells [4]. (c) A transparent substrate of a 200-μm-thick c-Si wafer, fabricated with hole-shaped light transmission windows [5].

DSSCs are progressively being included into consumer items, alongside their architectural uses. Companies such as G24 Generation (UK) and EXEGER Sweden have pioneered the creation of innovative devices powered by dye-sensitized solar cells (DSSC), including self-charging earphones, wearable technology, and backpacks equipped with integrated solar panels for off-grid power generation, as demonstrated by their DSSC charger and bag prototypes [6], [7]. Likewise, Solaronix (Switzerland) and Dyesol (Australia) have concentrated on prototypes for semi-transparent window panels, bus shelters, and terrace coverings, broadening the application of DSSCs beyond energy production to include aesthetic and functional purposes. These items illustrate the versatility of DSSC technology across several applications, including consumer electronics and sustainable infrastructure solutions.

Figure 3. G24 power limited dye-sensitized module (a), power curve charger (b), backpack (c) and duffel (d) bag with an integrated DSSC [7].

In addition to its aesthetic adaptability, DSSCs are acknowledged for their ecological advantages. In contrast to traditional silicon-based photovoltaic systems, dye-sensitized solar cells (DSSCs) are produced through less energy-demanding methods and materials, enhancing their sustainability. Moreover, their versatility in diverse lighting circumstances broadens their uses, extending from outdoor installations to energizing indoor devices and the Internet of Things (IoT). Nevertheless, these benefits are accompanied by problems. Dye-sensitized solar cells (DSSCs) presently encounter constraints in efficiency (η), durability, and scalability, which are essential for extensive commercialization.

Figure 4 illustrates the distribution of solar irradiance, emphasizing the predominance of the infrared (IR) region, which constitutes approximately 51% of the total solar energy at AM 1.5G circumstances. This observation highlights the considerable potential of solar devices that selectively capture energy from the infrared spectrum. Dye-sensitized solar cells (DSSCs) featuring tailored dyes that absorb near-infrared (NIR) light offer potential to exploit a neglected segment of the solar spectrum. Progress in organic photovoltaic (OPV) technologies has shown the viability of near-infrared (NIR) selective absorption, with devices attaining power conversion efficiencies (PCEs) that are equivalent to or surpass those targeting visible-light absorption. Lunt et al.'s innovative study on NIR-selective OPVs obtained a PCE of 1.7% and an average visible transmittance (AVT) of 56%, demonstrating the combined advantages of energy capture and transparency. Recent advancements have enhanced these parameters, with devices achieving power conversion efficiencies of 7-10% and average voltage thresholds of 30-50%, propelled by improvements in narrow-bandgap donors and non-fullerene acceptors. The developments in NIR-responsive technologies facilitate the creation of high-performance transparent photovoltaics (TPVs), broadening the use of dye-sensitized solar cells (DSSCs) for architectural and indoor uses where both transparency and efficiency are essential.

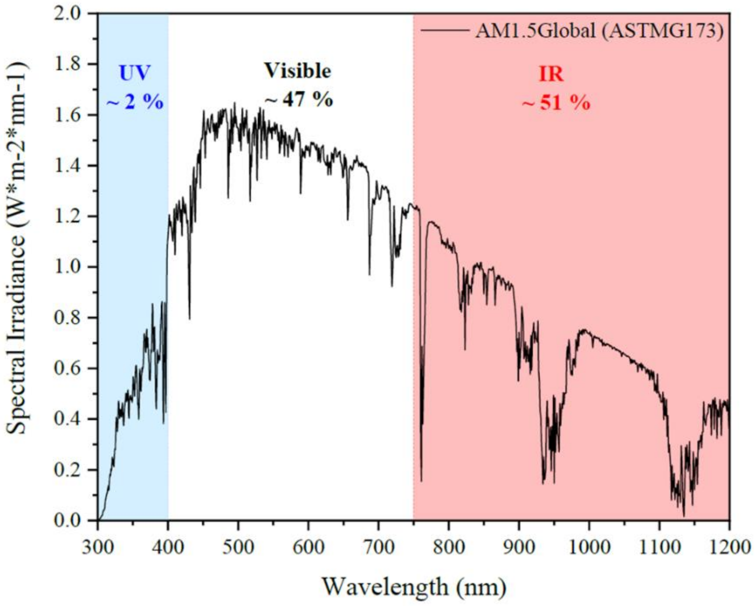

Figure 4. Evolution of the solar irradiance as a function of wavelength under A.M.1.5G conditions.

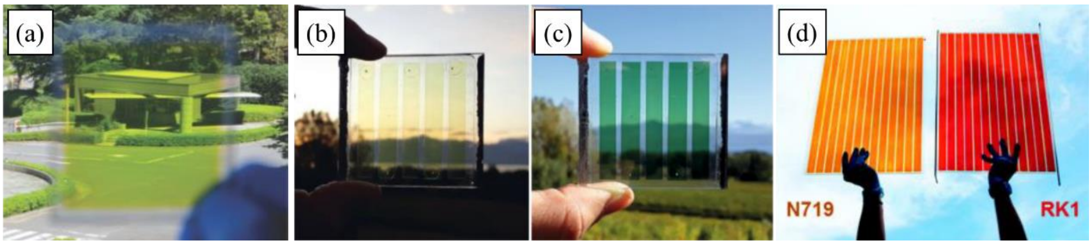

Figure 5. Semi-transparent DSSC cells and modules. (a) Y1/HSQ5 cocktail cell [8], (b) and (c) evolution of color of semitransparent NPI-based module when exposed to natural light [9], and (d) large area DSSC panels fabricated by Solaronix [10].

Recent improvements in semi-transparent dye-sensitized solar cells (DSSCs) have revealed the possibility to merge aesthetic appeal with energy production. In 2014, Han et al. developed a green-hued transparent dye-sensitized solar cell (DSSC) with a power conversion efficiency (PCE) of 3.66% and a peak transmittance of 60% at 560 nm (Figure 5a). This method utilizes the co-sensitization of a short D−π−A dye (Y1) for blue-light absorption and a squaraine dye (HSQ5) for red-light absorption, resulting in a transmittance gap in the green spectrum, suitable for semi-transparent applications. Demadrille et al. developed a photochromic semi-transparent DSSC exhibiting an average visual transmittance (AVT) of 59% in darkness, which decreases to 27% under illumination, reaching a power conversion efficiency (PCE) of 3.7% (Figure 5b).

The efficacy of DSSCs depends on the complex interaction among their components: the dye, semiconductor, electrolyte, and counter electrode. The molecular dye, functioning as the light-harvesting agent, is vital in ascertaining the device's performance. The capacity to absorb a wide range of sunlight, efficiently inject electrons into the semiconductor, and regenerate effectively within the electrolyte cycle is essential. The selection of electrolyte impacts charge transport and stability, whereas the characteristics of the semiconductor affect electron mobility and recombination rates. Enhancing these components necessitates a multidisciplinary strategy that amalgamates chemistry, materials science, and engineering.

This thesis enhances the development of DSSCs by examining a crucial element: the interplay among dyes, solvents, and device efficacy. The research commences by examining the photophysical characteristics of a particular category of dyes in mixed solvent environments. Solvents are crucial in DSSCs, affecting the solubility and adsorption of dyes as well as the efficacy of light absorption and electron transfer mechanisms. The influence of parameters like solvent polarity, viscosity, and molecular interactions on dye behavior and device stability is analyzed. This research seeks to improve the performance and longevity of DSSCs by customizing solvent conditions, facilitating their incorporation into practical applications.

The results of this research transcend the systems examined, providing insights into the wider domain of molecular photovoltaics. As DSSCs advance, they possess the capacity to transform the solar energy sector, integrating functionality, sustainability, and aesthetics. This research enhances comprehension of DSSC components and processes while contributing to the global initiative to produce efficient, cost-effective, and aesthetically adaptable renewable energy systems.

An essential element in the progression of DSSC technology is the creation and use of sophisticated analytical tools to elucidate the complex photophysical and electrical mechanisms that dictate their efficacy. A major issue in optimizing DSSCs is elucidating the interactions among charge production, transport, and recombination dynamics, which collectively determine the device's power conversion efficiency (PCE) and long-term stability. Chapter 2 of this thesis examines the application of sophisticated spectral modeling approaches and computational tools for the analysis of transient absorption spectroscopy (TAS) data. TAS is an essential method for investigating the time-resolved dynamics of photoinduced events in DSSCs, including electron injection, charge transport, and recombination. Extracting significant insights from TAS data necessitates advanced modeling methods capable of defining kinetic pathways and quantifying the timeframes of these processes. A unique software framework was created to analyze decay-associated spectra (DAS) and extract essential kinetic characteristics. This method enhances comprehension of transient processes in DSSCs and acts as an effective instrument for characterizing and refining the design of dyes, semiconductors, and electrolytes. Chapter 2 illustrates the combination of experimental spectroscopy and computational modeling, illustrating how sophisticated analytical methods can connect basic research with practical improvements in DSSC performance.

The investigation of innovative dyes is a crucial advancement in DSSC technologies, as elaborated in Chapter 3. The efficacy of DSSCs is fundamentally connected to the molecular architecture of the sensitizing dye, which dictates light absorption, electron injection, and dye regeneration. This chapter examines two novel dye systems: SubPc derivatives and VG20-TBPF. SubPc dyes, characterized by their adjustable photophysical properties and structural adaptability, offer a promising opportunity to enhance the absorption spectrum of dye-sensitized solar cells (DSSCs), especially within the visible and near-infrared regions of solar radiation. These dyes can enhance current sensitizers, facilitating the creation of dual or co-sensitized systems that optimize solar energy capture. Conversely, VG20-TBPF dyes provide a distinctive blend of energy efficiency and aesthetic adaptability, rendering them suitable for semi-transparent DSSCs employed in building-integrated photovoltaics (BIPVs). These dyes enable a compromise between performance and design, allowing DSSCs to function as both energy generators and architectural features. To fully harness the potential of these innovative dyes, it is essential to tackle issues such chemical stability, compatibility with device components, and scalability for extensive applications. Chapter 3 examines these matters, providing a comprehensive assessment of the photophysical characteristics, device efficacy, and application prospects of these sophisticated dye systems.

The primary objective of this thesis is to tackle the significant obstacles encountered in DSSC research and development, encompassing both fundamental photophysical investigations and practical device implementations. Chapter 1 lays the foundation by examining the interplay between D205 dye and their solvent environment, a crucial element affecting light absorption, electron injection, and dye regeneration. The solvent qualities of polarity, viscosity, and hydrogen bonding capacity significantly influence the efficacy of sensitizing dyes, and this chapter offers a thorough examination of these effects. Chapter 1 clarifies the connection between solvent dynamics and dye efficacy, establishing a foundation for enhancing the molecular environment of DSSCs, hence facilitating increased efficiency and stability.

Chapter 2 expands on this basis by presenting advanced computational techniques for the analysis of transient processes in DSSCs. These tools expand our comprehension of the underlying mechanics and offer practical insights for optimizing device performance. Identifying and quantifying bottlenecks, such as fast recombination or inadequate electron transport, is essential for informing the design of next-generation DSSCs. This chapter illustrates the significance of multidisciplinary methodologies, integrating empirical data with theoretical modeling to establish a comprehensive framework for dyes and devices study.

Ultimately, Chapter 3 expands the frontiers of DSSC research by exploring innovative dye systems that fulfill both technical and aesthetic criteria. The use of sophisticated dyes such as SubPc and VG20-TBPF underscores the capability of DSSCs to go beyond conventional applications, facilitating their deployment in aesthetically pleasing and multifunctional energy solutions. This chapter's findings highlight the adaptability of DSSCs, illustrating their capability to satisfy the varied requirements of contemporary energy systems, ranging from high-efficiency solar panels to semi-transparent modules for architectural incorporation. This thesis together contributes significantly to the study of DSSCs by addressing essential gaps in comprehension and developing the technology for practical applications. This research adopts a comprehensive approach to enhancing DSSC performance by examining the interaction between dye chemistry, device physics, and practical design factors. The findings derived from this research have ramifications not just for dye-sensitized solar cells (DSSCs) but also for the wider fields of photovoltaics and renewable energy.

Chapter 1: Investigation of D205 Dye Behavior in Acetonitrile-Butanol Solvent Mixtures: Photophysical Properties and Performance Analysis

This chapter constitute the first part of a tryptic dedicated to the understanding of the solar cells. Here is the first part consisting in a wide investigation of the photodynamic of an organic photosensitizer commonly used in dyes-sensitized-solar-cells. To explore the effect of the mixture of acetonitrile and butanol on the photophysics of the indole dye D205 used in solar cells, a wide range of spectroscopic techniques were employed. Steady-state UV−visible absorption and emission spectroscopy allowed to characterize the dependence of their maxima emission and absorbance on the mixture composition as well as to quantify their fluorescence quantum yield. Transient absorption spectroscopy was supplemented by TCSPC measurements to quantify the time relaxation of the excited states.

1. Introduction

In the study and development of efficient DSSCs, the electrolyte and sensitizer stand out as key components for the cell's performance [11]. Therefore, scientists primarily focus on these two components to improve the efficiency of solar cells. The nature of the environment (polarity, hydrogen bond formation ability, dipole-dipole interactions, viscosity, etc.), the processes occurring in the excited state (increase in the proportion of non-radiative processes), and the structural characteristics of the sensitizers can pose challenges in the development of high-efficiency solar cells [12], [13]. This study proposes an investigation into the photophysical behavior of the D205 sensitizer in a simulated electrolyte solution (acetonitrile-butanol), analyzing its photophysics in isolation, outside the DSSC working conditions.

The fabrication of a DSSC using D205 as a dye sensitizer was reported in the literature in 2008, recording a significant efficiency of 7.18% [14]. D205 is an organic dye belonging to the class of indoline and its structure is shown in Figure 6. To promote good performance in a photovoltaic cell, an organic sensitizer needs to have donor, acceptor and π-bridge moieties. In the structure of D205, the triphenylethylene and indoline cores represent the donor moiety. The π -bridge and acceptor parts, in this case, are the two rhodanine rings. The carboxyl functions as the anchoring group [14], [15].

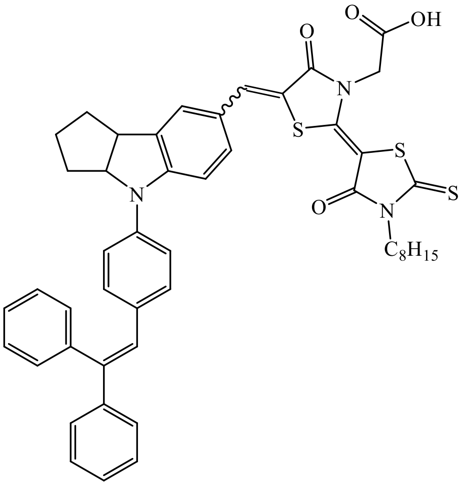

D205

Figure 6. Chemical structure of D205.

The influence of solvents properties on dye photophysics can affect the match between the dye adsorption spectrum and the solar spectrum, disturbing the DSSC performance. In the literature, it is possible to find many works where some dye's optical properties were investigated using different types of solvents, searching to understand better the solvatochromic effect and how the solvent properties (polarity and H-bond donor ability) will influence it [15], [16]. Prieto *et al.* [17] analyzed the photophysical properties of the dye pyrromethene 597 (PM597) in a wide variety of solvents and the resulting changes in the absorption and fluorescence bands, Stokes shift, and quantum yield values. The authors notified that both absorption and fluorescence bands were shifted toward lower wavelengths by increasing the solvent polarity (isooctane λ_{Max}^{Abs} = 527.5 nm / λ_{Max}^{Em} = 569.0 nm and 2,2,2-trifluoroethanol λ_{Max}^{Abs}= 521.6 nm / λ_{Max}^{Em}= 561.2 nm). This hypsochromic effect usually reduces the chromophore dipole moment upon excitation. Through quantum mechanical calculations, it is confirmed that the dipole moment of the PM597 molecule in the ground state is located in the short molecular axis. As the polar solvent stabilized the ground state better than the excited state, the S_0-S_1 energy gap in this environment was bigger than in the apolar solvent, explaining the observed blue shift. The fluorescence quantum yields and lifetimes of the dye in different solvents were also analyzed in this study. When comparing the environments, these parameters increase in polar solvents. In other to identify the solvent parameter that was affecting more the absorption and fluorescence bands, a Multiparameter Regression Analysis was employed. The dye's absorption and fluorescence wavenumbers were correlated to the solvent polarity/polarizability, H-bond-donor, and electron-releasing abilities. The results showed that the dominant coefficient affecting the photophysical behavior of the dye is the one related to the polarity/polarizability of the solvent.

Lohse *et al.* [18] also studied the relationship between the photophysics of dyes and solvent characteristics by performing steady-state spectroscopy. A proportionality was found between Stokes-shift and solvent polarity, indicating that the dipole moment of the dye increases under photoexcitation, leading to higher stability of the excited state in polar solvents. Also, Time Correlated Single Photon Counting tests revealed an inverse proportionality between fluorescence lifetime and solvent polarity, indicating a considerable influence of hydrogen bonds on the system dynamics.

Another interesting study by Smortsova *et al.* [12] investigates the behavior of indoline photosensitizers of the same class than D205 in a benchmark of sixteen solvents. As in the previous examples, the bands related to the S_0-S_2 and S_0-S_1 energy transitions in the absorption spectrum and the band related to the S_0-S_1 transition in the emission spectrum showed changes in their positions for different solvent types. By using Lippert-Mattaga, Kamlet-Taft and Catalan solvatochromic scales, they evidenced that the spectroscopic behaviors of the indoline dyes were dominated by the polarity of the solvents but however, they observed the influence of the H-bond donor and acceptor abilities of the solvents. Such changes are related to the solvents hydrogen bonding ability since polar solvents better stabilize the excited state of the dye molecule with a higher dipole moment than the ground state. The study also highlights that the red-shift shown in the alcohol's spectrum bands is even more pronounced, including when compared to solvents that have similar or even higher dielectric constants. The bathochromic in the absorption spectrum of indoline dyes may be beneficial for their application in DSSC by shifting the absorption spectrum in the near infra-red region. On the other hand, the sharp stabilization of the excited state in alcohols, for example, can lead to a downshift in the S_1 excited state energy level. Since the electron injection process in DSSCs depends on the difference between the energy levels of the excited state of the dye and the conduction band of the semiconductor, the sharp energy reduction of S_1 may be undesirable.

Analyzing the behavior of the sensitizer in contact with the electrolyte in the DSSC structure is crucial to understanding the efficiency of energy conversion. This study involves investigating the chemical and physical interactions between the sensitizer and the electrolyte, the stability of the sensitizer under working conditions, as well as the charge transfer kinetics. This is essential knowledge for optimizing the performance of DSSCs and improving the durability and efficiency of photovoltaic devices [19], [20]. A suitable electrolyte fulfills its function of carrying electrons between the cathode and anode, providing good conductivity within the DSSC. A typical liquid electrolyte has a redox couple in its composition, along with other additives, including an organic solvent to carry out the exchange of electrons during the cell's operating process [21]. The highest reported efficiency for a traditional DSSC using a typical electrolyte, with a low viscosity solvent such as ACN and iodide/triiodide as the redox mediator, is 11.18% [22]. However, both the solvent and the redox pair have limitations, such as corrosive behavior when in contact with the cell's metal substrates. Therefore, different electrolyte formulations have been developed and tested with the aim of improving performance and increasing long-term stability, reducing unwanted phenomena such as corrosion and leakage, problems that represent a bottleneck in the production of these devices [23], [24].

In order to improve cell performance, liquid electrolytes based on organic solvents are used due to their advantages such as low viscosity, high conductivity, simple preparation methods and the great connectivity of the electrode/electrolyte interface. Acetonitrile (ACN) is a popular choice for DSSC production, and its use has resulted in the highest efficiency device ever reported (>14%) [25]. However, this organic solvent has inherent stability problems due to its low boiling point and rapid evaporation when exposed to stressful conditions. Therefore, solvent mixtures, selected for their physical and chemical properties, are used to obtain optimal performance from DSSCs. For example, the final electrolyte can be optimized by adding a solvent with a higher boiling point to ACN [21].

Long-term stability is one of the main challenges encountered in the production of DSSC. As an alternative to solving this issue, ionic liquids (ILs) have been studied. A simple definition for them could be: organic salts that are liquid at ambient temperature. Their promising characteristics such as chemical and thermal stability, moderate ionic conductivity and minimal vapor pressure have led to the elimination of the risk of leakage through the cell channel and consequently to the production of the first stable cell ever demonstrated [26]. On the other hand, features such as high viscosity and cost of purification of ILs may limit their application in DSSC. Therefore, to take advantage of their beneficial electrolyte properties and, at the same time, outweigh properties inconvenient to cell production and operation, ILs can be mixed with molecular solvents (MS) such as acetonitrile (ACN), γ-butyrolactone (γ-BL), propylene carbonate (PC), etc. The choice of MS to compose the mixture targets such characteristics as a wide electrochemical window, relatively high dielectric constant, low viscosity, wide liquid state temperature range, and non-toxicity [16], [27], [28].

It is possible to find reported in the literature several studies involving indoline dyes, but their photophysics are not yet fully understood, especially when these molecules are surrounded by a mixture such as IL-MS. Maity *et al.* [13] investigated the photophysics of the D149 dye in a mixture of the ionic liquid 1-butyl-3-methylimidazolium tetrafluoroborate ($BmimBF_4$) and acetonitrile. Steady-state and femtosecond transient absorption spectroscopies were performed on solutions with different molar fractions of $BmimBF_4$ and ACN. The absorption spectrum showed the maximum absorption wavelength, which is related to the S_0-S_1 transition, decreases with increasing IL mole fraction (λ_{Max}^{Abs} = 542 nm in $BmimBF_4$, while λ_{Max}^{Abs} = 531 nm in acetonitrile). Considering that the dielectric constant values of the solvents $BmimBF_4$ and ACN are 0.57 and 0.71, respectively, reducing the polarity of the medium leads to a red shift in the absorption spectrum. On the other hand, the emission spectrum behaves oppositely. The maximum emission positions show a blue shift with decreasing polarity of the solvent mixture (λ_{Max}^{Em} = 644 nm in $BmimBF_4$, while λ_{Max}^{Em} = 665 nm in acetonitrile). Furthermore, the Stokes shift decreases with an increasing IL mole fraction. In analyzing four different time components describing the D149 relaxation, the authors relate the largest time component τ_4 to the excited state relaxation. Although, in general, the value of this component increases with increasing IL molar fraction, an initial decrease of τ_4 was observed in the regions corresponding to $\chi_{IL} < 0.1$. A similar initial decrease is also observed on the curve relating quantum yield values and IL molar fraction. The authors also mention divergences in the IL-MS mixture polarity values. When considering the solvatochromic polarity parameter (E_N^T), $BmimBF_4$ shows higher polarity than ACN, in contrast to what the dielectric constant values indicate. Also, according to a previous study by Manchini et al., the E_N^T values for the $BmimBF_4$-ACN mixture increase with increasing IL molar fraction, which highlights the difficulties in describing the polarity of the medium when it comes to IL.

Considering all the particular features presented by the IL-MS mixture, this chapter aims to clearly understand the photophysics of indoline dyes, avoiding the controversies brought by the presence of IL in the system. Thus, the mixture between 1-butanol (BuOH) and acetonitrile was chosen to compose the solution of D205, the indoline dye used in this study. The solvent BuOH was chosen due to the presence of the hydroxyl group in its structure, besides being a compound commonly found at low cost.

This chapter presents a comprehensive photochemical characterization of D205 in BuOH/ACN mixtures using a variety of spectroscopic techniques. The investigations are divided into two parts: (i) steady-state spectroscopy and (ii) time-resolved spectroscopy. The first part covers steady-state spectroscopic characterization, including Raman spectroscopy, UV-visible, and fluorescence spectroscopies. In the second part, two time-resolved spectroscopic techniques are employed to gain insight into the photodeactivation processes occurring in D205 systems: (i) time-correlated single-photon counting fluorescence and (ii) femtosecond transient absorption using the pump-probe technique. Through these characterizations, a comprehensive understanding of the photochemical processes following D205 excitation will be achieved, allowing identification of the solvent properties that govern the behavior of this sensitizer.

2. Experimental study of the photophysical behavior of D205 in acetonitrile and butanol mixtures

As mentioned above, the main motivation for this study is to understand the photophysical behavior of D205 in conventional solvent mixtures and identify which solvent properties is dominating the spectroscopic properties. The study conducted previously showed some particularities of the system D205 in IL-ACN mixture. When the molar fraction of the IL was between 0 and 0.20, the maximum absorption wavelength significantly decreased, while the maximum emission wavelength and the Stokes shift reached their peaks. At the same time, there was a minimum in the relative quantum yield and the excited state lifetimes. Furthermore, in a high IL content, the excited state relaxation times were correlated with viscosity, whereas in a low content, it was the solvent polarity that influenced the behavior of the excited state relaxation times. With a mixture composition of about 0.10, the photophysical properties of the studied IL-ACN mixtures indicated a transition between situations where solvation was dominated by ions and by the solvent.

Ionic liquids are considered complex due to their diverse composition and particular properties. They can be considered as ionic salt that are liquid at ambient temperature. They consist in different cation-anion pairs, each with its unique characteristics, such as melting points, viscosity and solubility, which can make predicting their behavior a challenge. Their non-traditional properties, such as remaining liquid over a wide temperature range and their intricate molecular interactions, further complicate studies involving them. Therefore, in order to eliminate such variables and focus only on conventional solvent properties, a simpler mixture (BuOH-ACN) was used here.

The overall objective is to analyze whether the behavior of the dye in mole fractions of BuOH less than 0.2 resembles the behavior observed for the same dye in the same mole fractions, but in IL. To achieve this, Raman, UV-Vis, Fluorescence, Time-Correlated Single Photon Counting (TCSPC) and Transient Absorption (TA) spectroscopic analyses were performed on D205 solutions containing different mole fractions of BuOH and ACN.

2.1. Steady-state spectroscopy investigations

2.1.1. Molecular interactions in BuOH-ACN mixtures studied by Raman Spectroscopy

To further elucidate the molecular interactions and dynamics inside the chosen BuOH/ACN mixture, FT-Raman analysis was employed. Raman spectroscopy is a powerful technique for investigating molecular vibrations and can provide detailed information on the structural and electronic interactions present in the mixed solvent systems. This part specifically focuses on understanding the vibrational characteristics and intermolecular interactions in BuOH/ACN mixtures varying molar fractions. FT-Raman spectra were recorded with a Bruker IFS 66 V spectrometer. The 1064 nm radiation of a Nd laser was used for excitation with a laser power of 250 mW. Between 10000 and 40000 interferograms were recorded. The spectral resolution was set at 1 cm^{-1}. By analyzing the Raman spectra, we aim to identify and characterize the significant vibrational modes and their dependence on the composition of the mixture.

Raman analysis was conducted on twelve samples of BuOH-ACN mixtures with different molar fractions. The main bands identified in the normalized spectra are shown in Figure 7. Two main bands were investigated, the O-H and C≡N vibration modes of BuOH and ACN. The Raman spectrum of BuOH is characterized by a shoulder around 3250 cm^{-1} alongside a main peak (Figure 7a). As the mole fraction of BuOH (X_{BuOH}) decreases, these two contributions become more distinct, suggesting that the O-H group experiences two different environments: one resembling that in pure BuOH and another where BuOH interacts with ACN molecules. This indicates the inhomogeneous distribution of BuOH molecules in the mixture.

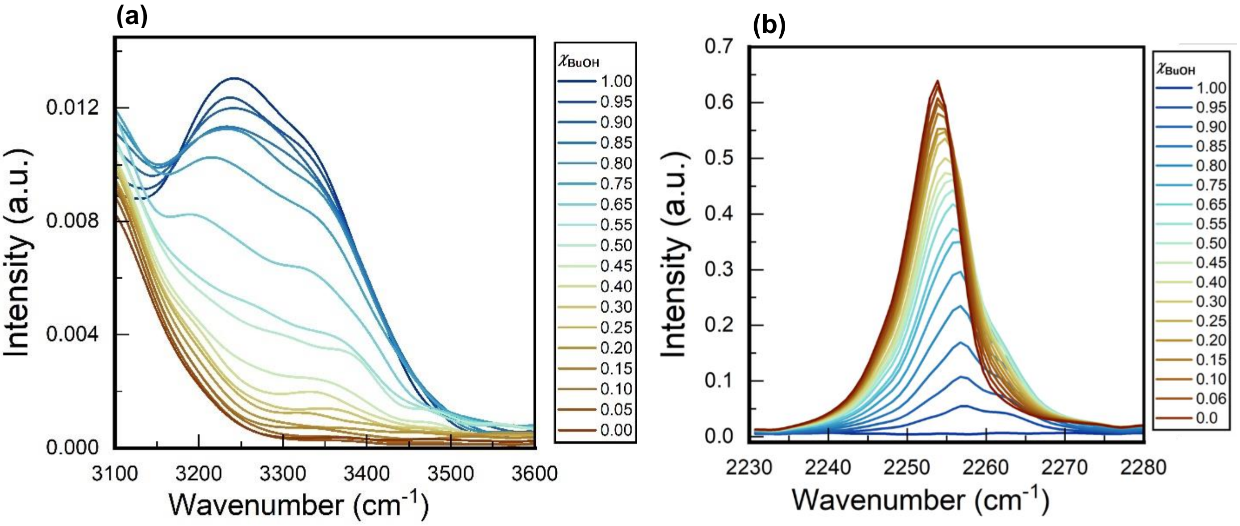

Figure 7. Main bands observed in the normalized Raman spectra of BuOH/ACN mixtures with different molar fractions. (a) shoulder at 3250 cm^{-1} characteristic of the O-H vibration mode and (b) Band at around 2253 cm^{-1} corresponding to C≡N vibration mode.

As X_{BuOH} increases, the position of the C≡N vibration mode shifts slightly to higher wavenumbers (Figure 7b), indicating a weakening of the dipole-dipole interactions. Notably, for X_{BuOH} values higher than 0.5, a shoulder appears on the high-frequency side of the C≡N vibration mode (around 2260 cm^{-1}), which suggests the formation of hydrogen bonds between ACN and BuOH. The persistence of the low-frequency peak indicates that, even at these X_{BuOH} values, dipole-dipole interactions remain significant. This provides further evidence of the inhomogeneous distribution of ACN molecules in the mixture [29]–[31].

2.1.2. Experimental dependence of the UV-Vis absorption and emission spectra on the solvent's mole fractions

The UV-Vis absorption steady-state measurements were recorded with a CARY 3500 spectrometer (Agilent) in the 300 to 800 nm spectral range. Fluorescence steady-state spectra were acquired with a FluoroMax-3 spectrofluorometer (Jobin-Yvon-Horiba) in the 480 to 850 nm range with an excitation wavelength at 470 nm. The bandpass was set at 2 and 3 nm in excitation and emission, respectively. A correction for the wavelength-dependent response of the instrument was applied. The excitation spectrum of the lamp

(λ_{Max}^{Ex} = 467 nm) and the Raman water band (λ_{Max}^{Em}= 350 nm) were checked every time the spectrofluorometer was used to ensure the correct functioning of the excitation and emission monochromators. A set of 10 mm Quartz fluorescence cells SUPRASIL from Hellma with screw cap and septum were used. D205 has been excited at its maximum absorption wavelength, pumping the S_0-S_1 band selectively. All the fluorescence spectra intensities, presented in wavenumbers for the analysis, have been corrected by λ^2.

For the fluorescence quantum yields measurements, the reference dye has been chosen with an absorption and fluorescence spectra in the same spectral window than D205, and the concentration of the samples have been set to an optical density < 0.1 to avoid the effect of an internal filter and reabsorption. A Nile blue solution with a known fluorescence quantum yield in ethanol (Φ_{fluo} = 0.27) was used as a reference [32].

The D205 dye was theoretically investigated using time-dependent density functional theory (TD-DFT) [15]. The study demonstrated that the S_1 excited state of D149 exhibits charge transfer character, with the dominant transition occurring from the HOMO to the LUMO. In this system, the HOMO is delocalized over the donor moiety, including the indoline nitrogen, while the LUMO is centered around the rhodanine rings. This behavior was confirmed by Smortsova et al. in their work on D149. Dr. Smortsova also performed DFT calculations in her PhD manuscript, using functionals that were selected for their favorable time/performance ratio for aromatic molecules. The M06HF functional from the Truhlar group, paired with the 6-31G basis set, was used to calculate the geometry and visualize the frontier orbitals. TD-DFT calculations for D149 were then performed with several functionals, including B3LYP, PBE0, M062X, M06HF, M05, MN15, and wB97XD, all with the 6-31+G(d) basis set.

Dr. Smortsova explained that the changes in the dipole moment of indoline dyes, which are strongly suggested by solvatochromism analysis, are directly linked to the redistribution of electron density upon photoexcitation. Figure 8, extracted from her manuscript, illustrates the four molecular orbitals potentially involved in the $S_0 \rightarrow S_1$ transition: the highest occupied molecular orbital (HOMO), the second highest occupied molecular orbital (HOMO-1), the lowest unoccupied molecular orbital (LUMO), and the second lowest unoccupied molecular orbital (LUMO+1). In the HOMO, the electron density is primarily localized on the triphenylethylene, indoline, and one rhodanine ring moieties, while in the LUMO, the electron density is transferred to the rhodanine rings. The character of the HOMO-1 and LUMO+1 orbitals is less pronounced but similar to the HOMO and LUMO.

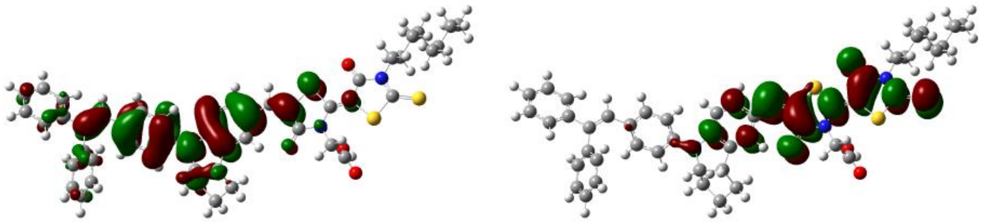

(a) HOMO 218

(b) LUMO 219

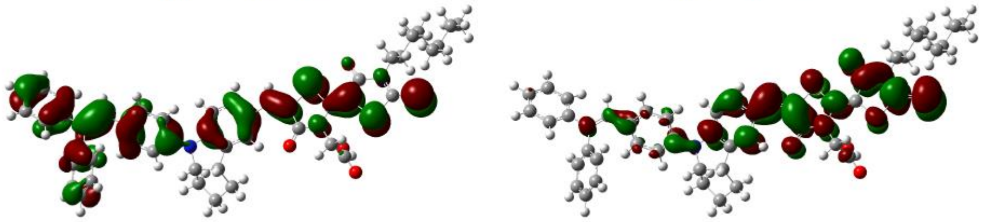

(c) HOMO-1 217

(d) LUMO+1 220

Figure 8. D205 orbitals, calculated with M06HF/6-31G level of theory. Iso-value=0.02 was used to visualize the isosurfaces of electron density [15].

Therefore, intramolecular charge transfer is expected to occur in the D205 dye as well. Importantly, the octyl chain does not participate in the transition, which is typical due to its saturated nature. Instead, the octyl chain acts to space the dye from the semiconductor, reducing the likelihood of charge recombination. A crucial observation is that the electron density, although transferred from donor to acceptor, does not directly reach the anchor group, -COOH. This may limit the potential of D205 as a sensitizer for DSSCs.

The absorption and emission steady-state spectra of D205 solutions with different molar fractions of BuOH are shown in Figure 9. The spectroscopic characteristics of D205 in various BuOH/ACN mixtures are presented in Table 1. The absorption spectra show two main peaks corresponding to two different transitions; the most intense matches the transition S_0-S_1 and the less intense in the high-frequency region S_0-S_2. The S_0-S_2 absorption bands are assigned to π–π^* transitions. The energy difference between these absorption bands is also reasonably high to assign them to different electronic transitions and not vibronic levels. As expected, the S_0-S_2 transition is located in the short-wavelength region due to its higher energy [33]. The photosensitizer D205 follow the Kasha-Vavilov rule: whatever is the excited state you populate while exciting the sample, fluorescence always arise from the lowest in energy singlet excited state $S_1 \rightarrow S_0$ [34].

The D205 absorption and emission spectra performed in this chapter are consistent with the general trends reported in literature. The dye absorbs light up to 650 nm (D205 has the highest red-shifted spectrum compared to other indoline derivatives) and exhibits a significant Stokes shift. The absorption band has a weak vibronic shoulder. The experimental results show that the S_0-S_1 band is red-shifted in pure BuOH (λ_{Max}^{Abs} = 531 nm) compared to the band in pure acetonitrile (λ_{Max}^{Abs} = 524 nm) (Figure 9a). The S_0-S_1 D205 spectral band shows dependence on the amount of BuOH in the binary mixture, while the S_0-S_2 band does not show any significant shift. It can be explained by the fact that the electron density distributions in the S_0 and S_2 states lead to the same total dipole moment of the molecule. The positions of the maximum emission wavelength show the overall blueshift (Figure 9b) while decreasing the mixture polarity (λ_{Max}^{Em} = 650 nm in pure acetonitrile and λ_{Max}^{Em} = 633 nm in 1-butanol).

The relationship between hydrogen bond dynamics and electronic spectra is that strengthening hydrogen bonds will lead to the relative spectra red-shifting. On the other hand, weakening the hydrogen bond can cause the electronic spectra to shift towards blue [35]. In fact, when comparing alcohols and aprotic solvents, a red-shift is expected in the steady-state absorbance and fluorescence spectra, even if the aprotic solvent has a similar or even higher dielectric constant than the alcohol [15]. When the absorption spectra were analysed, a red-shift was indeed observed as the mole fraction of BuOH increased, which can be explained by the reduction in the energy level of the excited state (S_1) following an additional stabilization of the dye's excited state in BuOH, a protic solvent, compared to ACN, a polar aprotic solvent. However, the opposite happens with the emission spectrum, where we observe a blueshift occurring with increasing BuOH molar fraction (Figure 10).

This results from the complex effects of the interactions between the solvents and D205. The redshift in absorption indicates that BuOH, being polar, stabilizes the excited state of the dye better compared to ACN, resulting in a reduction in absorption energy. However, for emission, the blueshift suggests that the stability of the excited state during emission is lower in BuOH than in ACN. A possible hypothesis is that, while BuOH stabilizes the excited state during absorption, it does not do the same during emission. BuOH, being a polar protic solvent, can stabilize the excited state through hydrogen bonding, which affects the electronic density and distribution in excited states. Relaxation dynamics can change with the type of solvent, and BuOH can modify the energy of the excited state from which emission occurs, resulting in a shorter wavelength. In addition, solvent-specific interactions and differences in the way D205 relaxes after absorption may contribute to these observed effects [36], [37]. Therefore, it is expected that this complex interplay of different factors, which influence the energy levels of the ground and excited states of D205 in opposite ways, will result in a red shift in the absorption spectrum.

To quantify the polarity of ACN and BuOH, several polarity scales can be applied, each highlighting specific solvent interactions. Among the most commonly used scales for assessing solvent polarity in photophysical studies, the solvatochromic polarity parameter, E_N^T, combines the effects of a solvent's polarity and hydrogen-bonding capabilities on solvatochromic dyes, providing a single metric that can be especially useful for understanding solvent effects on photophysical properties

Table 1. Spectroscopic properties of D205 in BuOH/ACN mixtures for various molar fractions of 1-butanol (χBuOH): maximum absorption and emission wavelengths (λ^{max}, in nm) and wavenumbers ($\tilde{\nu}^{max}$, in cm^{-1}), Stokes shift ($\Delta\nu_{Stokes}$, in cm^{-1}) defined as the difference of maximum wavenumbers for absorption and emission, fluorescence quantum yield Φ_{fluo}. Nile Blue in ethanol was used as a standard (Φ_{fluo} = 0.27) [32]. Solvent properties: dielectric constant ε [38].

χ_{BuOH}	λ_{abs}^{max}	λ_{em}^{max}	$\tilde{\nu}_{abs}^{max}$	$\tilde{\nu}_{em}^{max}$	$\Delta\nu_{Stokes}$	ε	Φ_{fluo}
0 (ACN)	524	650	19084	15385	3699	35.95	0.102
0.05	525	648	19048	15432	3616	34.11	0.1
0.1	525	649	19048	15408	3639	32.62	0.097
0.14	526	649	19011	15408	3603	31.11	0.096
0.2	527	648	18975	15432	3543	29.65	0.093
0.3	527	647	18975	15456	3519	27.09	0.091
0.4	527	646	18975	15480	3495	25	0.086
0.5	528	645	18939	15504	3436	23.17	0.073
0.6	528	644	18939	15528	3411	21.63	0.063
0.65	528	643	18939	15552	3387	20.33	0.062
0.7	529	642	18904	15576	3327	19.25	0.064
0.8	529	641	18904	15601	3303	18.48	0.062
0.9	530	640	18868	15625	3243	18.1	0.058
1 (BuOH)	531	633	18832	15798	3035	17.15	0.056

While ACN is highly polar and aprotic (with reduced hydrogen bonding capabilities), BuOH, as a polar protic solvent, offers both hydrogen-bond donating and accepting abilities. In the context of photophysical studies, the solvatochromic polarity parameter (E_N^T) is a key metric for interpreting the Stokes shift. The E_N^T for BuOH and ACN are 0.586 and 0.460, respectively. As the BuOH content in a solvent mixture increases, the effective E_N^T also raises, enhancing both polarity and hydrogen-bond donating ability. This increased E_N^T can stabilize the excited state of the D205 more than its ground state, thereby reducing the energy gap between absorption and emission, and consequently, the Stokes shift expressed in wavenumbers.

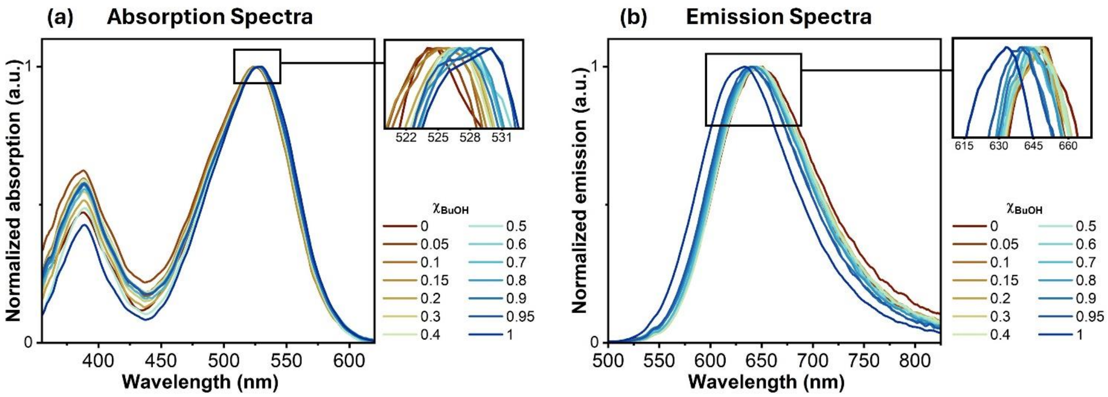

Figure 9. Steady-state normalized absorption (a) and emission (b) spectra of D205 in BuOH-ACN mixtures for various BuOH molar fractions.

It is possible to observe a linear correlation between the maximum absorption wavelength and the BuOH molar fraction in the mixture and the dielectric constant (Figure 10). The equations that can describe the mathematical relationship between these two quantities are described below (Equations 1 and 2).

$$\lambda_{Max}^{Ex} = 5.7111 \cdot \chi_{BuOH} + 524.89 \;\; (R^2 = 0.94) \tag{1}$$

$$\lambda_{Max}^{Ex} = -0.2947 \cdot \varepsilon + 534.87 \;\; (R^2 = 0.93) \tag{2}$$

Compared to λ_{Max}^{Abs}, the maximum emission wavelength demonstrates a more complex correlation with the molar fraction of 1-butanol in the binary mixture and the dielectric constant, as denoted by equations 3 and 4.

$$\lambda_{Max}^{Em} = -12.098 \cdot \chi_{BuOH}^{2} + 1.3955 \cdot \chi_{BuOH} + 648.93 \; (R^2 = 0.94) \tag{3}$$

$$\lambda_{Max}^{Em} = -0.0513 \cdot \varepsilon^{2} + 3.3113 \cdot \varepsilon + 595.72 \; (R^2 = 0.88) \tag{4}$$

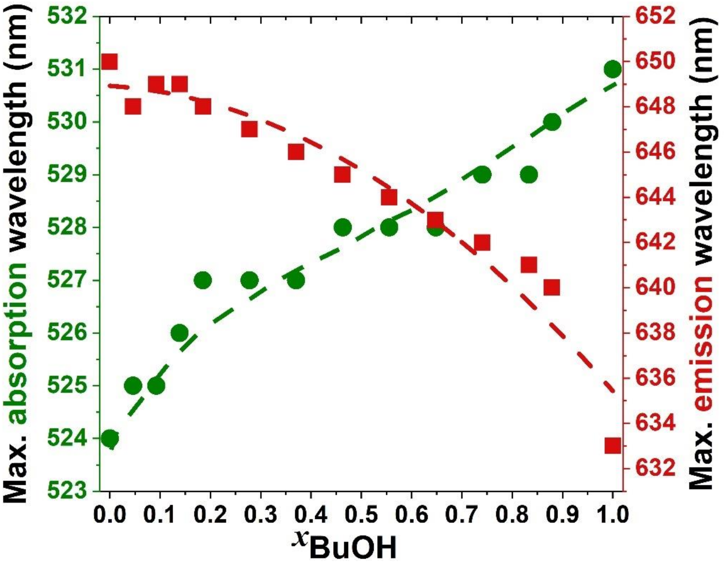

Figure 10. Change of D205 absorption and emission maxima against the BuOH mole fraction in the BuOH-ACN binary solvent mixture.

It is necessary to consider that in DSSC, the electron injection efficiency from the dye in the S_1 state into the conduction band of the semiconductor depends on the energy difference between these two energy levels. This means that the composition of the solvent in the electrolyte is crucial to optimize the spectroscopic characteristics of the sensitizer. To limit this stabilization processes of the S_1 state, we can already, from now, identify two solvent properties responsible for this fact: the H-bond donor ability and the polarity induce the reduction of the energy of the S_1 state according to our results.

This delicate interplay of energy levels highlights the importance of understanding other critical factors that influence dye performance as a sensitizer. One such factor is the fluorescence quantum yield, which provides significant insights into the photophysical behavior of the dye. It is also well-known that a high fluorescence quantum yield dye will also be a photosensitizer with high performance. Indeed, a high fluorescence quantum yield usually goes together with a long fluorescence lifetime inducing that the electron remains for a longer time in the S_1 excited state, increasing in this way the probability of the electron injection into the semi-conductor band. A simple definition of the fluorescence quantum yield is the ratio of the number of photons emitted divided by the number of photons absorbed [39]. Fluorescence quantum can also be expressed in terms of radiative and non-radiative rate constants:

$$\Phi_{\mathrm{fluo}} = \frac{\mathrm{k}_{\mathrm{rad}}}{\mathrm{k}_{\mathrm{rad}} + \mathrm{k}_{\mathrm{nrad}}} \tag{5}$$

where $\mathrm{k}_{\mathrm{rad}}$ is the rate constant of the radiative process and $\mathrm{k}_{\mathrm{nrad}}$ is the rate constant of the sum of the non-radiative processes, which involves constants of internal conversion and intersystem crossing. The fluorescence quantum yield can be related to the fluorescence lifetime:

$$\tau_{\mathrm{fluo}} = \frac{1}{k_{rad} + k_{non-rad}} \tag{6}$$

$$\Phi_{\mathrm{fluo}} = \frac{\tau_{\mathrm{fluo}}}{\tau_{\mathrm{rad}}} \tag{7}$$

The lifetime of the fluorophore in the absence of non-radiative processes is called the radiative lifetime and is given by:

$$\tau_{\mathrm{rad}} = \frac{1}{\mathrm{k}_{\mathrm{rad}}} = \frac{\tau_{fluo}}{\Phi_{fluo}} \tag{8}$$

Considering all the formulas presented above, we can obtain a formula for calculating the constant of non-radiative processes:

$$\mathrm{k}_{\mathrm{nrad}} = \frac{k_{rad}\,(1-\Phi_{fluo})}{\Phi_{fluo}} \tag{9}$$

Fluorescence quantum yield is a crucial characteristic of luminophores, providing information's on the relaxation processes occurring in the dye system from its excited state to the ground state. The fluorescence quantum yields of D205 in mixtures were measured using the reference method. With this method, the reference compound absorption and emission spectra must be measured in addition to those of the studied compound. The compilation of quantum yields of reference compounds are published [23]. Importantly, the fluorescence spectra of the reference and the studied compounds must be in the same spectral window and the concentration of the samples must be low (OD < 0.1) to avoid self-absorption effects. Finally, all the requirements being satisfied, the quantum yield of the compound studied was calculated using Equation 9:

$$\Phi_{sample}^{fluo}(\lambda_{exc}) = \Phi_{ref}^{fluo}(\lambda_{exc}) \cdot \frac{\int_0^\infty I_{sample}^{fluo}(\lambda_{exc};\lambda_{fluo})\, d\lambda_{fluo}}{\int_0^\infty I_{ref}^{fluo}(\lambda_{exc};\lambda_{fluo})\, d\lambda_{fluo}} \cdot \frac{1-10^{-A_{ref}(\lambda_{exc})}}{1-10^{-A_{sample}(\lambda_{exc})}} \cdot \frac{n_{solvent\,sample}^2}{n_{solvent\,ref}^2} \tag{9}$$

where the integrals represent the areas under the corrected emission spectra of the sample and the reference, respectively. A correction for the absorbance of the sample and the reference solutions at the excitation wavelength is also provided with the second ratio. Nile blue in ethanol ($\Phi_{fluo} = 0.27$) has been used as reference.

The fluorescence quantum yields of D205 in the various mixtures are all very weak (between 0.06 and 0.1) and it is difficult to identify an obvious trend. However, it should be noticed that the albeit minor changes of the fluorescence quantum yields observed in Figure 11 (around 30 % downfall for Φ_{fluo} between $X_{BuOH} = 0.4$ and $X_{BuOH} = 0.55$) can be compared to a transition between a set of two main plateaus values : (i) a first plateau with a $\Phi_{fluo} = 0.1$-0.09 for the molar fraction region X_{BuOH}=0-0.4 and (ii) a second plateau Φ_{fluo} =0.06-0.055 for the molar fraction region X_{BuOH}=0.55-1. To summarize, adding butanol induces a fluorescence quenching of around 30 %.

One trend should anyway be emphasized: the decrease of the quantum yield of D205 while increasing the BuOH molar fraction (Figure 11). The weaker signal in BuOH indicates that this solvent may open non-radiative pathways for the deactivation of D205 when compared to pure acetonitrile. The relatively low Φ_{fluo} of the dye can also be attributed to its flexible structure. Molecule fragments are linked by single covalent bonds, allowing significant conformational flexibility. Moreover, the nature of the double bond connecting the indoline and rhodanine fragments can change upon photoexcitation, potentially allowing rotation about this bond axis in the excited state. Smortsova *et al.* [12] reported that a decrease in the dipolarity and polarizability of the solvent decreases Φ_{fluo} of the indoline dyes, while the solvent's basicity and acidity weaken the fluorescence of D205. These observations are in good agreement with our data showing that as the molar fraction of BuOH increases, there is a decrease in polarity and an increase in the system's acidity. However, it is necessary to study these phenomena in more detail. As the mole fraction of BuOH increases, so does the viscosity, which can inhibit the internal movements of the molecular fragments, thereby reducing the proportion of non-radiative processes.

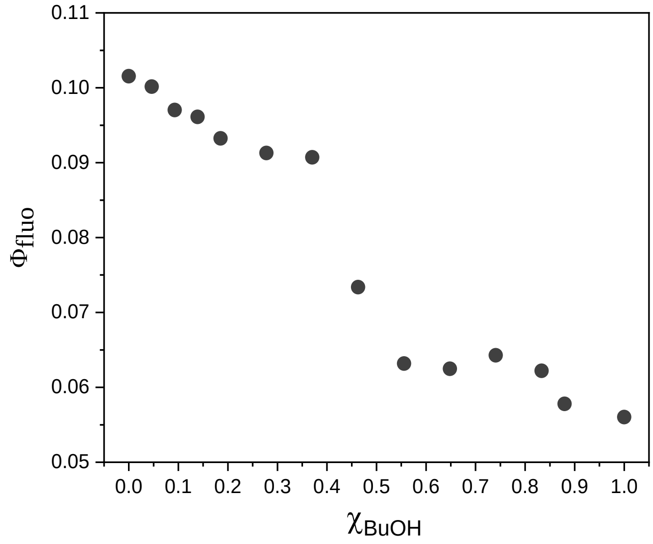

Figure 11. Change of fluorescence quantum yield value against the molar fraction of the 1-butanol in the BuOH/ACN binary solvent mixture.

The weak fluorescence quenching of D205 we observed while adding BuOH has already been evidenced by El-Zohry *et al.* for another very close sensitizer D149 [40], [41]. During the adsorption process of the dye on TiO_2, deprotonation of the carboxylic anchor group of the dye occurs and the carboxylate group binds via 2 titanium atoms. But the free proton should be transferred and recombined with one oxygen of some neighboring TiO_2. It has been shown that this close proton can dramatically quench the fluorescence of D149 sensitizer [40]. El-Zohry *et al.* exhibited that protons coming from protic solvent or from neighboring dyes can quench the excited state of D149. They evidenced that rhodanine moieties of D149 are responsible for the fluorescence quenching by external proton. These protons can come from solvent. Both dynamic and static quenching processes are occurring in indoline dyes in protic solvent [41].

2.2. Time-resolved spectroscopic characterization of D205

2.2.1. Characterization of the fluorescence lifetimes of D205 using Time-Correlated Single Photon Counting technique (TCSPC)

The fluorescence decays of D205 in ACN/BuOH mixtures of the samples were acquired using Time-Correlated Single Photon Counting (TCSPC) techniques. This technique is considered as a conventional method for time-resolved fluorescence using electronic detection. Here the time resolution is determined by electronic means (only by the choice of the detector).

The excitation source is provided by a mode-locked laser diode (467 nm, 4 MHz). A set of OD grey filters (1.5 and 0.04) were applied to attenuate the excitation beam power and to maintain the Poisson statistics of the count's distribution. A FT-200 PicoQuant spectrometer was used to perform fluorescence signal acquisition. A HAMAMATSU cooled microchannel plate photomultiplier tube was used as the detector, with signals recorded by a PicoHarp 300 TCSPC card. A single-grated monochromator placed after the emission polarizer 0.5 mm slits provided 4 nm spectral resolution. The overall temporal resolution of the setup was characterized by the Instrument Response Function (IRF), measured by placing a LUDOX solution in the sample holder and recording the scattered excitation light to get the time profile of the excitation pulse. The IRF full-width half maximum (FWHM) was measured to be 80 ps. All the system was checked before each experiment, recording the fluorescence decays of C153 in MeOH and ACN at 530 nm, giving both a mono-exponential decay ($\chi^2 = 1.01$) with times in good agreement with literature, 4.03 ns and 5.62 ns respectively [42].

The fluorescence decays were analysed with multiexponential models (Equation 10) using FluoFit PicoQuant software [43].

$$F(t) = \int_0^t IRF(t') \sum_{i=1}^{n} A_i \exp\left(-\frac{t-t'}{\tau_i}\right) dt' \tag{10}$$

where $IRF(t')$ is the instrument response function, n is the number of exponential components, A_i and τ_i are the pre-exponential factors and lifetimes of i-th exponential component. The iterative reconvolution procedure was followed, applying Poisson distribution weighing. The quality of the fits was estimated by visual inspection of the weighted residues and autocorrelation function $Res(\tau)$ of residues, as well as the reduced chi-squared value $\chi^2_{Red} < 1.1$.

The TCSPC technique involved exciting the sample with a low-intensity picosecond laser diode that operates at a high frequency (4 MHz). The 80 picoseconds time-resolution of the setup allows processes and phenomenon of this time order to be studied. The fluorescence decays were measured for pure solvents, specifically BuOH and acetonitrile ACN, as well as for 12 different solutions of D205 varying molar fractions of these solvents. The varying molar fractions allow for the investigation of how different solvent compositions affect the fluorescence lifetimes of the photosensitizer D205.

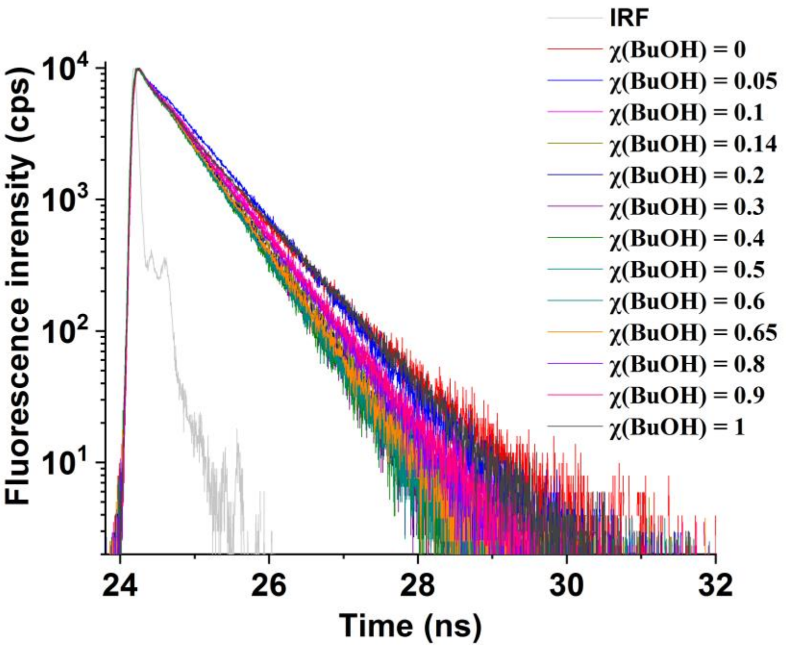

Figure 12. Fluorescence decays of D205 in BuOH/ACN mixtures excited at 467 nm for various BuOH molar fractions from 0 to 1. IRF has an FWHM of 80 ps. All the measurements decays were recorded at the maximum emission wavelengths of the corresponding steady-state emission spectra of the solutions with a 4 nm spectral resolution.

The fluorescence decays of D205 in the mixtures are plotted in Figure 12. It can be difficult to highlight any obvious trend in the decay's evolution with the different mixtures just by examining Figure 12. Therefore, we will need to analyze the data and fit the fluorescence decays deconvoluting the IRF in order to extract the typical time-components of D205 in the various mixtures. These fluorescence decays can be fitted following a bi-exponential function. Table 2 stores the fitting parameters of the fluorescence decays. The two time-components extracted for the decay are of hundreds of picoseconds. The first time-component τ_1, in the range of 500-700 ps, has the highest amplitude in all the decays. The second time-component τ_2, between 60-200 ps, has the weakest amplitude.

To identify significant trends in the evolution of fluorescence time-resolved characteristics with varying mixture compositions, the average fluorescence lifetimes of D205 were calculated, along with the rate constants for radiative and non-radiative processes. These data are presented in Table 3.

Table 2. The fitting parameters of the fluorescence decays of D205 in the binary mixtures varying BuOH molar fractions obtained using multiexponential functions, relative contributions (Ai, normalized to the sum of positive components), and time-components (τ_i, ps). Excitation and emission wavelengths were set to 467 nm and maximum emission bands.

X_{BuOH}	A_1	τ_1 (ps)	A_2	τ_2 (ps)	A_3	τ_3 (ps)	χ^2
0	427.9 ± 4.1	752.61 ± 4.5	455.29 ± 8.2	358.39 ± 6.1	324.6 ± 28.3	65.13 ± 6.7	0.914
0.05	1092.3 ± 6.2	631.68 ± 2.6	415.4 ± 26.2	93.97 ± 7.0	-	-	0.924
0.1	1213.4 ± 6.4	572.61 ± 2.1	431.0 ± 24.4	99.01 ± 6.6	-	-	0.932
0.14	1203.2 ± 6.6	540.46 ± 2.1	445.1 ± 25.0	96.73 ± 6.4	-	-	0.939
0.2	1193.5 ± 6.4	520.43 ± 1.9	499.8 ± 25.5	87.64 ± 5.3	-	-	0.941
0.3	1178.1 ± 6.3	499.20 ± 5.5	467.8 ± 23.1	95.52 ± 5.5	-	-	0.939
0.4	1231.4 ± 7.0	497.43 ± 2.0	563.8 ± 26.4	91.80 ± 5.0	-	-	1.047
0.5	1197.6 ± 6.3	504.53 ± 1.9	523.8 ± 21.0	111.58 ± 5.1	-	-	0.937
0.6	1246.8 ± 7.2	511.40 ± 2.1	552.2 ± 24.1	111.29 ± 5.6	-	-	1.062
0.65	1213.9 ± 6.5	525.14 ± 1.9	609.3 ± 22.4	110.00 ± 4.6	-	-	0.934
0.8	1120.9 ± 6.2	576.52 ± 2.2	631.2 ± 21.3	123.96 ± 4.8	-	-	0.954
0.9	1183.2 ± 6.2	595.78 ± 2.2	770.5 ± 22.0	124.12 ± 4.0	-	-	0.926
1	1191.4 ± 6.6	698.31 ± 2.6	1045.6 ± 22.4	160.13 ± 3.82	-	-	0.983

When analyzing Table 3, it is evident that the average fluorescence lifetimes (τ_{fluo}) of D205 are consistently sub-nanosecond, ranging between 400 and 500 ps. This relatively fast fluorescence lifetime can be attributed to a combination of structural characteristics and environmental influences. Specifically, El-Zohry *et al.* [44] proposed a twisting mechanism for the non-radiative deactivation of the donor unit in indoline dyes, involving torsion and pyramidalization of the middle ethylene group. According to their model, these conformational changes in the excited state allow the system to access a conical intersection (CI), leading to ultrafast non-radiative deactivation (Figure 13). The twisting of the bond in the donor fragment, particularly in the triphenylethylene group, induces a CI between the excited state and the ground state, facilitating rapid deactivation of the excited population. This mechanism likely contributes to the observed short fluorescence lifetimes of D205.

Table 3: Average fluorescence lifetimes (τ_{fluo}, ps), radiative and non-radiative relaxation rate constants (10^8 s^{-1}) and the ration between of D205.

X_{BuOH}	τ_{fluo} (ps)	k_{rad} (10^8 s^{-1})	k_{nrad} (10^8 s^{-1})	k_{nrad}/k_{rad}
0	419.4	2.4	21.4	8.8
0.05	483.1	2.1	18.6	9.0
0.1	448.0	2.2	20.2	9.3
0.15	420.9	2.3	21.5	9.4
0.2	392.3	2.4	23.1	9.8
0.3	384.3	2.4	23.7	10.0
0.4	369.7	2.3	24.7	10.6
0.5	384.5	1.9	24.1	12.7
0.6	388.2	1.6	24.1	14.9
0.65	386.3	1.6	24.3	15.1
0.8	413.1	1.5	22.7	15.1
0.9	409.3	1.4	23.0	16.2
1	446.7	1.3	21.1	16.9

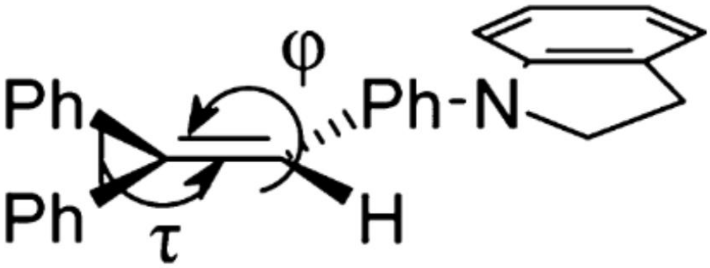

Figure 13. Scheme of the reduced donor unit of indoline dyes showing the torsion (φ) and pyramidalization (τ) angles in the middle ethylene group. Taken from El-Zohry *et al.* [44].

Moreover, interactions between D205 and the solvent molecules may play a crucial role in modulating the fluorescence lifetimes. The effect of adding BuOH to the mixture is not immediately apparent in the fluorescence decay characteristics. It was observed that fluorescence quantum yields were quenched with the addition of BuOH, which would typically lead to a shortening of the average fluorescence lifetimes as the BuOH molar fraction increases. However, no significant trend was observed when plotting τ_{fluo} against the BuOH molar fraction. To better understand the changes induced by the addition of BuOH and to explain the apparent inconsistency between the fluorescence lifetimes and quantum yields, the evolution of radiative and non-radiative processes with increasing XBuOH was evaluated. Therefore, the rate constants for both radiative (k_{rad}) and non-radiative (k_{nrad}) processes were calculated using the average fluorescence lifetimes (τ_{fluo}) and fluorescence quantum yields (both obtained with the same excitation wavelength of 467 nm). These data are presented in Table 3 and Figure 14 illustrates the evolution of the k_{nrad}/k_{rad} ratio as X_{BuOH} increases.

Considering the radiative rate constants (k_{rad}) evolution while adding BuOH to the mixture, it can be noted that, although the values fluctuate somewhat, a significant decrease (~ 48%) of k_{rad} occurs. The radiative constants remain lower than the pure ACN value for all mixture compositions. This result is consistent with the observed evolution of the fluorescence quantum yield. Regarding the evolution of the non-radiative rate constants, k_{nrad}, it is important to note that their value remains relatively stable, with a maximum variation of ± 10-15 %, as BuOH is added to the mixture. This result suggests that non-radiative deactivation pathways of D205 stay dominant in any case.

The evolution of k_{rad} while adding BuOH to the mixture is in favor of the fact that adding protic solvent to ACN induces a decrease of the radiative pathways for the deactivation of the excited population of D205. This quenching may be due to the Hydrogen bonding confirming the hypothesis advanced by El-Zohry [40], [41], [44]–[46], Smortsova [12] and Maity [13] on the importance of the hydrogen bonds.

It should also be emphasized that the dominant deactivation processes in D205 are non-radiative, as the k_{nrad} values are an order of magnitude larger than the k_{rad} values. This dominance of non-radiative pathways may be attributed to the ease with which the dye undergoes conformational changes in its excited state, a characteristic that is central to D205. To further support this conclusion, the evolution of the k_{nrad}/k_{rad} ratio is shown in Figure 14. It can be observed that this ratio doubles as X_{BuOH} increases from 0 to 1, indicating that non-radiative rate constants significantly outweigh radiative rate constants across all mixture compositions.

The results from the fluorescence time-resolved experiments can be summarized in three main points. First, the observed Φ_{fluo} and k_{rad} evolution with X_{BuOH} confirmed what El-Zohry and Smortsova already mentioned concerning the fluorescence quenching of D205 in protic solvent due to hydrogen bonding donor abilities of BuOH. Second, the domination of the non-radiative rate constants over the radiative ones confirms the hypothesis of El-Zohry about the conformational twisting of indoline dye in the excited state allowing the excited population to access a conical intersection through which an ultrafast non-radiative deactivation is possible.

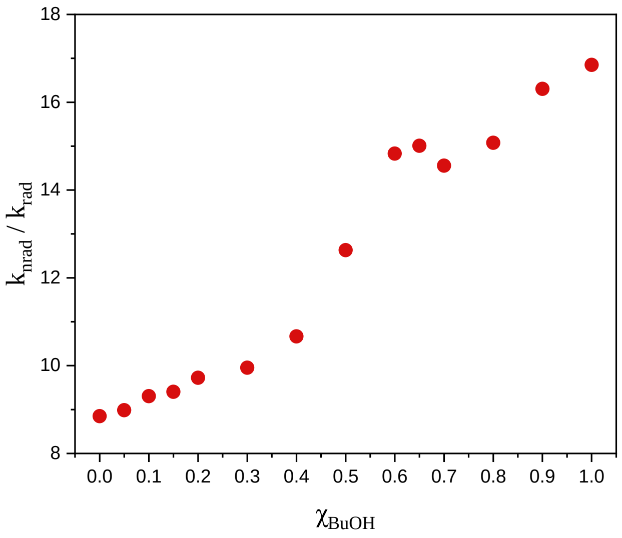

Figure 14. Ratio between the constants k_{rad} and k_{nrad} of the D205 samples in ACN/BuOH with different butanol mole fractions.

This means that the non-radiative pathways are always preferentially taken by the excited population of D205 during its deactivation and all of this is allowed by the conformation changes of the molecule while excited. Finally, the evolution of the $k_{non-rad}/k_{rad}$ ratio obviously show the increasing domination of the non-radiative deactivation while adding BuOH to the mixture.

All these results a in complete agreement with our group's previous findings (Smortsova and Maity), showing that the addition of protic solvent to the mixture induces an increase of the non-radiative deactivation pathways for D205. Based on our previous work and the literature, such as El-Zohry 's studies, two main properties of the solvent can now be identified as governing the photodynamics of D205: hydrogen-bond donor/acceptor abilities.

2.2.2. Femtosecond Transient Absorption Spectroscopy Analysis of D205 Dye: Dynamics of Excited-State Relaxation and Solvent Effects

In this final part of the chapter, an overview of the photodynamic deactivation of D205 will be provided, examining whether it corroborates the previous results obtained from steady-state and time-resolved fluorescence. Femtosecond Transient Absorption Spectroscopy (TAS) is based on excitation-induced electronic transitions, offering detailed information on the dynamics of excited-state relaxation and photochemical reactions. By recording the time evolution of the excited D205 absorption in ACN/BuOH solutions at various wavelengths, the reaction pathways can be mapped, providing insights into the underlying mechanisms on timescales ranging from femtoseconds to approximately 6 ns. The investigations enabled the establishment of a correlation between the solvent mole fraction and the time components associated with different molecular dynamics. The tests were performed using a 488 nm pump with a probe in the visible range. The spectra at different times were extracted using the Surface Xplorer software, then processed and adjusted using the FemtoFit software. Following the adjustments, kinetic graphs and decay-associated spectra were also obtained.

To characterize the effect of the mixture composition on the excited-state decay pathways of the indole dye D205 with higher resolution than that provided by TCSPC, transient absorption spectra were measured. Figure 15a shows the 3D TAS obtained for the indole dye dissolved in ACN. It reflects the time and wavelength dependence of three main features: (i) the ground state bleach (GSB), which appears at 522 nm as a negative signal at the absorption wavelengths of the indole dye D205's ground state. This reflects the depletion of ground-state molecules due to excitation to higher energy states; (ii) the excited state absorption (ESA), which appears as a positive signal at wavelengths where the excited state of the indole dye D205 absorbs light; and (iii) the stimulated emission (SE), which appears as a negative peak around 650 nm at wavelengths where the excited D205 would fluoresce.

The intensity of the GSB increases slowly at early times (below 8.33 ps) and then rises more quickly with increasing delay time, before eventually returning to zero around 2 ns. The diffuse ESA contribution is seen as a positive diffuse signal at a range wavelengths between 580 nm and 750 nm where the excited state of the indole dye D205 absorbs light. This absorption represents transitions from the excited state (likely S1 or higher) to even higher electronic states. The ESA contribution splits into two main regions based on wavelength: shorter-wavelength ESA contribution shows an initial increase in intensity and reaches a maximum around 6 ps, followed by a decrease at longer delay times. Additionally, it shifts slightly toward shorter wavelengths as time progresses, which could indicate structural relaxation in the excited state. While the longer-wavelength ESA contribution is more diffuse. Its intensity decreases over time and even becoming negative around 1 ps. The rapid intensity decrease suggests a fast relaxation or deactivation process in the excited state, possibly due to internal conversion or vibrational relaxation within the excited state. The SE emerges at early times and shifts progressively toward longer wavelengths, indicating that the excited state is relaxing to a slightly lower-energy configuration before emission. This shift may be explained by structural relaxation, as the molecule adjusts its geometry after excitation to a more stable configuration. The SE signal diminishes in intensity faster than the ESA signal, suggesting that non-radiative decay mechanisms are dominant, causing the excited state to deactivate primarily through pathways other than photon emission.

The time evolution of the TAS of the indole dye D205 in neat BuOH is illustrated in Figure 16. The time evolution of the three main futures, namely, the GSB, the ESA and SE, are illustrated in these figures. The intensity of the GSB contribution gradually increases and takes a longer time to return to zero compared to that in ACN. The positive ESA contribution initially appears broad and diffuse, spanning a wide range of wavelengths. As delay time advances, the ESA splits into two distinct components: one at higher wavelengths and one at lower wavelengths, with the higher wavelength component exhibiting a stronger intensity.

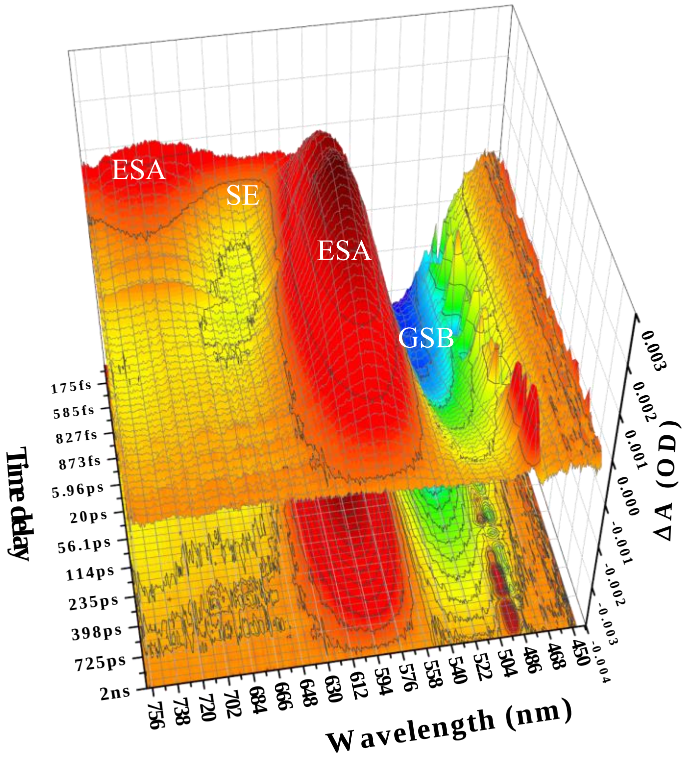

Figure 15. 3D Transient Absorption Spectrum of D205 in neat ACN showing excited-state absorption (ESA), stimulated emission (SE), and ground-state bleach (GSB) dynamics over time delay between the pump and the probe lasers and wavelength. The projection of the 3D plot onto the base XY-plane (wavelength vs. time) also is shown, allowing for quick visualization of key features over the entire time-wavelength range. The red for positive ΔAbsorbance, blue for negative indicates the direction and intensity of absorbance changes in the projection.

After 45 ps delay time, these two components become well-resolved, separated by a dip caused by the onset of the SE contribution (though it remains positive). At this point, the intensity of the high-wavelength component starts to exceed that of the low-wavelength one. With additional delay, the intensity of the short-wavelength ESA component increases and shifts toward lower wavelengths, while the intensity of the high-wavelength component gradually decreases, reaching zero by 207 ps. Meanwhile, the SE contribution, which is characterized by a low negative intensity, slowly diminishes over time. The short-wavelength ESA component, however, remains visible, with its intensity decreasing at a slower rate than that of the SE. The slow return of the GSB signal to zero indicates that the ground state repopulates gradually, suggesting that the excited states may be decaying over extended time scales. This slow recovery can imply a preference for non-radiative pathways as we can see later the radiative (SE) contribution is minimal or diminishes quickly, leaving longer-lived non-radiative decay processes in effect. Indeed, the SE component is characterized by a weak negative intensity and fades over time. This supports the interpretation that radiative decay does not play a dominant role in the relaxation of the excited state. Instead, the system likely relaxes predominantly via non-radiative pathways, where energy is eventually dissipated through conformation changes of the large flexible indole dye D205 rather than as emitted photons. In addition, the persistence of ESA at short wavelengths further supports the dominance of non-radiative processes. On top of that, the high-wavelength ESA component decays and approaches zero only after 207 ps. This relatively long-lived ESA behavior, combined with the low SE intensity, strengthens the interpretation that non-radiative pathways dominate the relaxation process, with energy gradually dissipated through internal conversion or other non-radiative channels instead of radiative pathways.

The behavior of the transient absorption spectra shape of D205 as a function of the BuOH-ACN molar fractions, indicates a gradual transition from that resembling its behavior in ACN to that in BuOH. The main changes are occurring in the range of xBuOH around 0.3.

The interpretation of the mixture dependence of the shape of the TAS can be summarized as follows: the indole dye D205 is a large flexible molecule, and the shifts observed in the ESA and SE regions, in the BuOH-ACN mixtures, over time likely reflect structural reorganization within the excited state. Following excitation, D205 undergoes conformational adjustments that stabilize the excited state. This stabilization is indicated by the shifts in ESA and SE to slightly different wavelengths. The rapid decay of the SE signal, combined with the persistence of the ESA, suggests that non-radiative processes play a key role in the excited-state deactivation.

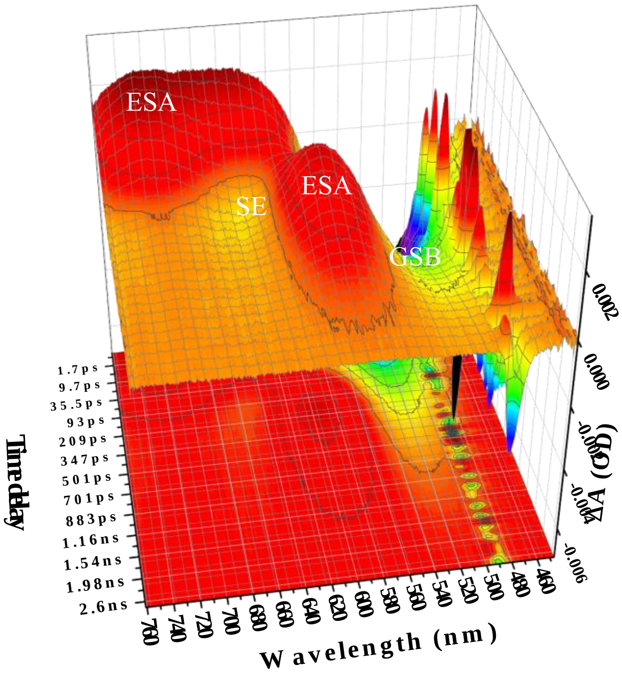

Figure 16. 3D Transient Absorption Spectrum of D205 in neat BuOH showing excited-state absorption (ESA), stimulated emission (SE), and ground-state bleach (GSB) dynamics over time delay between the pump and the probe lasers and wavelength. The projection of the 3D plot onto the base XY-plane (wavelength vs. delay time) also is shown, allowing for quick visualization of key features over the entire time-wavelength range. The red for positive ΔA absorbance, blue for negative indicates the direction and intensity of absorbance changes in the projection.

Furthermore, the global fit of the TAS suggests that the dynamic of photo excitation of the indole dye D205 in the BuOH-ACN mixtures is characterized by three relaxation times. The two faster relaxation times have features that are associated with the solvation dynamics and are not discussed in this paper. The mixture dependence of the longest time $\tau 1$ is visualized in Figure 17. It is associated with the excited state relaxation to the ground state, being equal to 282 ps and 655 ps in ACN and BuOH, respectively. These relaxation times are similar to those reported in the literature in the same neat solvents [12], [15], [47]. When adding BuOH to ACN ,This relaxation time goes through a shallow minimum at xBuOH = 0.3 and noticeably increases for further increase of the BuOH content.

Table 4. TA spectra global fit parameters: lifetime components of samples with different BuOH molar fractions.

χ_{BuOH}	FWHM (ps)	A1	τ_1 (ps)	A2	τ_2 (ps)	A3	τ_3 (ps)
0	0.15	-4.67E-04	282.5	1.12E-03	1.06	3.16E-04	0.50
0.05	0.13	-7.28E-04	278.6	4.60E-04	1.76	1.03E-03	0.45
0.1	0.14	-1.16E-03	285.3	1.59E-03	1.16	7.39E-04	0.54
0.15	0.073	-1.04E-03	265.1	1.84E-03	1.28	1.13E-03	0.29
0.2	0.09	-8.55E-04	265	1.44E-03	0.14	1.08E-04	1.89
0.3	0.07	-2.19E-04	329.1	1.30E-03	1.48	1.51E-04	0.13
0.4	0.08	-4.38E-04	337.6	1.95E-03	2.15	1.46E-04	0.14
0.5	0.09	-4.05E-04	361.4	1.82E-03	4.07	3.99E-04	0.30
0.6	0.08	-8.25E-04	365.6	2.20E-03	7.38	1.51E-03	0.58
0.7	0.08	-9.95E-04	372.1	2.91E-03	9.45	7.59E-04	0.48
0.8	0.97	-1.64E-03	394.0	5.74E-03	15.23	8.41E-04	1.02
0.9	0.06	-3.02E-04	515.2	1.23E-03	22.49	7.43E-04	0.46
1	0.06	2.20E-04	655.2	1.93E-03	36.24	-3.76E-04	0.46

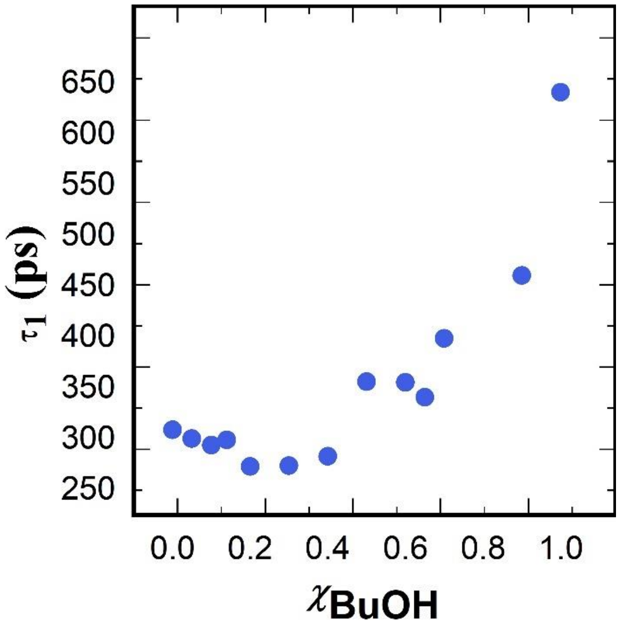

Figure 17. Evolution of the excited state lifetime related to the BuOH molar fraction.

Although the τ_{fluo} obtained at TCSPC are of the same order magnitude, the mixture dependence of the slowest relaxation times τ_1 (determined by TCSPC technique) and τ_1 (determined by TAS) seems to be different. This can be associated with the fact the time-resolution is bigger in the case of the TCSPC (80 ps) with respect to that in the TA experiment (~200 fs). This makes the later more sensitive to short time dynamics that can be missed by the former [48], [49]. Besides, the TCSPC is primary sensitive to the emissive excited state while the TA measures the excited state independently of its radiative and non-radiative character). Despite the difference between the techniques used to measure these relaxation times, their dependence as a function of the mixture composition reflects, to some extent, the fact that the non-radiative deactivation process of the indole dye D205 is at its maximum in the molar fraction between 0.3 and 0.5.

3. Conclusions

The effect of the mixture composition on the D205 photo physics was studied by analyzing the shapes of its absorption and emission spectra and by measuring both the Stokes Shift and the quantum yield. The results indicate that as the BuOH content in the mixture increases, changes in the local structure descriptors—particularly hydrogen donating and accepting bonding capacity and solvent polarity—lead to a red shift in the absorption maximum (7 nm) and a blue shift in the fluorescence maximum (17 nm). Additionally, both the Stokes shift and quantum yield decrease. The rate of change in these spectral properties is nonlinear, with each parameter responding uniquely to shifts in the mixture balance, transitioning from the polarity-dominated environment of acetonitrile to that of butanol. These findings also suggest that non-radiative decay is the primary relaxation pathway for the excited state of D205.

This stationary spectroscopic study of the D205 photo physics in the mixture was complemented by analyzing the dynamics of the excited state relaxation using both TCSPC and transient absorption time resolved spectroscopy. The obtained relaxation times, τ_1 and τ_{fluo} by the two technics are comparable to those in the two neat liquids. Their mixture composition dependence shows the same trend, namely, the relaxation time undergo a minor change in the lower BuOH content below 0.3 and it increases noticeably for further increase of the BuOH content. The weak contribution of the stimulated emission, the increase of the relaxation times $\tau 1$ and τ_{fluo} are indications of the dominance of the non-radiative process in the relaxation of the excited state. These illustrates how mixture composition, particularly the polarity and hydrogen-bonding ability of BuOH, significantly impacts the relaxation dynamics of D205's excited state as compared to the effect of ACN.

In conclusion, these results highlight that studying the photophysics of dyes in mixtures of molecular or ionic liquids reveals unique transitional behaviors. Key photophysical parameters—such as absorption and emission maxima, quantum yield, Stokes shift, and excited-state relaxation time—shift progressively from being influenced primarily by the characteristics of one component (e.g., polarity, hydrogen bonding capability, dipole-dipole interactions, or stacking) to those of the other component as the mixture composition changes.

4. General Introduction and Chapter 1 References

[1] B. O’Regan and M. Grätzel, “A low-cost, high-efficiency solar cell based on dye-sensitized colloidal TiO2 films,” *Nature*, vol. 353, no. 6346, pp. 737–740, Oct. 1991, doi: 10.1038/353737a0.

[2] E. Biyik *et al.*, “A key review of building integrated photovoltaic (BIPV) systems,” *Engineering Science and Technology, an International Journal*, vol. 20, no. 3. Elsevier, pp. 833–858, Jun. 01, 2017, doi: 10.1016/j.jestch.2017.01.009.

[3] E. Franklin, V. Everett, A. Blakers, and K. Weber, “Sliver solar cells: High-efficiency, low-cost PV technology,” *Adv. Optoelectron.*, vol. 2007, no. 1, p. 035383, Jan. 2007, doi: 10.1155/2007/35383.

[4] M. Biancardo *et al.*, “Characterization of microspherical semi-transparent solar cells and modules,” *Sol. Energy*, vol. 81, no. 6, pp. 711–716, Jun. 2007, doi: 10.1016/j.solener.2006.10.009.

[5] K. Lee *et al.*, “Neutral-Colored Transparent Crystalline Silicon Photovoltaics,” *Joule*, vol. 4, no. 1, pp. 235–246, Jan. 2020, doi: 10.1016/j.joule.2019.11.008.

[6] P. D. Sekaran and R. Marimuthu, “An Extensive Analysis of Dye-Sensitized Solar Cell (DSSC),” *Brazilian J. Phys.*, vol. 54, no. 1, pp. 1–10, Feb. 2024, doi: 10.1007/s13538-023-01375-w.

[7] S. Garcia Mayo, “Dye-Sensitized Solar Cells: the future of consumer electronics?,” 2021, Accessed: Nov. 28, 2024. [Online]. Available: https://urn.kb.se/resolve?urn=urn:nbn:se:hig:diva-36993.

[8] Z. Yin *et al.*, “Graphene-Based materials for solar cell applications,” *Advanced Energy Materials*, vol. 4, no. 1. John Wiley & Sons, Ltd, p. 1300574, Jan. 01, 2014, doi: 10.1002/aenm.201300574.

[9] Q. Huaulmé *et al.*, “Photochromic dye-sensitized solar cells with light-driven adjustable optical transmission and power conversion efficiency,” *Nat. Energy*, vol. 5, no. 6, pp. 468–477, Jun. 2020, doi: 10.1038/s41560-020-0624-7.

[10] D. Joly *et al.*, “Metal-free organic sensitizers with narrow absorption in the visible for solar cells exceeding 10% efficiency,” *Energy Environ. Sci.*, vol. 8, no. 7, pp.

2010–2018, Jul. 2015, doi: 10.1039/c5ee00444f.

[11] F. Grifoni *et al.*, “Toward Sustainable, Colorless, and Transparent Photovoltaics: State of the Art and Perspectives for the Development of Selective Near-Infrared Dye-Sensitized Solar Cells,” *Advanced Energy Materials*, vol. 11, no. 43. John Wiley & Sons, Ltd, p. 2101598, Nov. 01, 2021, doi: 10.1002/aenm.202101598.

[12] Y. Smortsova *et al.*, “Solvatochromic effects on a class of indoline derivatives organic photosensitizers: About the influence of hydrogen-bond acceptor and donor abilities parameters,” *J. Mol. Liq.*, vol. 245, pp. 76–84, Nov. 2017, doi: 10.1016/j.molliq.2017.06.052.

[13] N. Maity, P. Piatkowski, K. Polok, F. A. Miannay, and A. Idrissi, “Effect of the Mixture Composition of BmimBF4-Acetonitrile on the Excited-State Relaxation Dynamics of a Solar-Cell Dye D149: An Ultrafast Transient Absorption Study,” *J. Phys. Chem. C*, vol. 125, no. 32, pp. 17841–17852, Aug. 2021, doi: 10.1021/acs.jpcc.1c05008.

[14] D. Kuang, S. Uchida, R. Humphry-Baker, S. M. Zakeeruddin, and M. Grätzel, “Organic dye-sensitized ionic liquid based solar cells: Remarkable enhancement in performance through molecular design of indoline sensitizers,” *Angew. Chemie - Int. Ed.*, vol. 47, no. 10, pp. 1923–1927, Feb. 2008, doi: 10.1002/anie.200705225.

[15] Y. Smortsova, “Dye sensitized solar cells effciency improvement: optimization of the electrolyte using ionic liquids/molecular solvents mixture and study of the photodynamic properties of organic indolinic derivative dyes,” Universit_e de Lille, 2018.

[16] N. Maity, “Characterization of the polarity, reorientation dynamics and photophysics of indoline based solar cell dyes in ionic liquid-molecular solvent mixtures: steadystate UV-visible, EPR, time resolved fluorescence, femtosecond transient absorption and optical K,” Université de Lille, 2022.

[17] J. B. Prieto, F. L. Arbeloa, V. M. Martínez, T. A. López, and I. L. Arbeloa, “Photophysical properties of the pyrromethene 597 dye: Solvent effect,” *J. Phys. Chem. A*, vol. 108, no. 26, pp. 5503–5508, Jul. 2004, doi: 10.1021/JP0373898/ASSET/IMAGES/LARGE/JP0373898F00007.JPEG.

[18] P. W. Lohse *et al.*, “Ultrafast photoinduced relaxation dynamics of the indoline

dye D149 in organic solvents," *Phys. Chem. Chem. Phys.*, vol. 13, no. 43, pp. 19632–19640, Oct. 2011, doi: 10.1039/C1CP22429H.

[19] I. Benesperi, H. Michaels, and M. Freitag, "The researcher's guide to solid-state dye-sensitized solar cells," *Journal of Materials Chemistry C*, vol. 6, no. 44. Royal Society of Chemistry, pp. 11903–11942, Nov. 15, 2018, doi: 10.1039/c8tc03542c.

[20] S. V. Raksha, V. I. Kondrashin, E. A. Pecherskaya, and K. O. Nikolaev, "Functional Materials for Dye-sensitized Solar Cells," vol. 7, no. 4, p. 4062, 2015, Accessed: Jan. 31, 2023. [Online]. Available: https://essuir.sumdu.edu.ua/handle/123456789/44480.

[21] H. Iftikhar, G. G. Sonai, S. G. Hashmi, A. F. Nogueira, and P. D. Lund, "Progress on electrolytes development in dye-sensitized solar cells," *Materials*, vol. 12, no. 12. Multidisciplinary Digital Publishing Institute, p. 1998, Jun. 21, 2019, doi: 10.3390/ma12121998.

[22] M. K. Nazeeruddin *et al.*, "Combined experimental and DFT-TDDFT computational study of photoelectrochemical cell ruthenium sensitizers," in *Renewable Energy: Four Volume Set*, vol. 2–4, no. 48, American Chemical Society, 2018, pp. 227–251.

[23] P. Wang *et al.*, "Stable new sensitizer with improved light harvesting for nanocrystalline dye-sensitized solar cells," *Adv. Mater.*, vol. 16, no. 20, pp. 1806–1811, Oct. 2004, doi: 10.1002/adma.200400039.

[24] A. Yella *et al.*, "Porphyrin-sensitized solar cells with cobalt (II/III)-based redox electrolyte exceed 12 percent efficiency," *Science (80-.).*, vol. 334, no. 6056, pp. 629–634, Nov. 2011, doi: 10.1126/science.1209688.

[25] M. K. Nazeeruddin *et al.*, "Conversion of Light to Electricity by zyx cis-XzBis(zyxwv 2,2'-bipyridyl-4,4'-dicarboxylate)ruthenium(11) Charge-Transfer Sensitizers (X zyxw = C1-, Br-, I-, CN-, and SCN-) on Nanocrystalline Ti02 Electrodes," *J. Am. Chem. SOC. zyxw*, vol. 115, no. Ii, pp. 6382–6390, 1993.

[26] N. Papageorgiou *et al.*, "The Performance and Stability of Ambient Temperature Molten Salts for Solar Cell Applications," *J. Electrochem. Soc.*, vol. 143, no. 10, pp. 3099–3108, Oct. 1996, doi: 10.1149/1.1837171.

[27] L. A. Santa-Cruz *et al.*, “Effect of heterocyclic nitrogen ionic liquid additives on the rate of backreaction in DSSCS: An electrochemical characterization,” *J. Sci. Adv. Mater. Devices*, vol. 6, no. 3, pp. 483–487, Sep. 2021, doi: 10.1016/J.JSAMD.2021.05.007.

[28] D. Kuang, S. Uchida, R. Humphry-Baker, S. M. Zakeeruddin, and M. Grätzel, “Organic Dye-Sensitized Ionic Liquid Based Solar Cells: Remarkable Enhancement in Performance through Molecular Design of Indoline Sensitizers,” *Angew. Chemie*, vol. 120, no. 10, pp. 1949–1953, 2008, doi: 10.1002/ange.200705225.

[29] J. R. Reimers and L. E. Hall, “The solvation of acetonitrile,” *J. Am. Chem. Soc.*, vol. 121, no. 15, pp. 3730–3744, 1999, doi: 10.1021/ja983878n.

[30] O. Quinet, B. Champagne, and V. Rodriguez, “Experimental and theoretical investigation of the Raman and hyper-Raman spectra of acetonitrile and its derivatives,” *J. Chem. Phys.*, vol. 124, no. 24, p. 244312, 2006, doi: 10.1063/1.2208350.

[31] K. L. Rowlen1 and J. M. Harris, “Raman Spectroscopic Study of Solvation Structure in Acetonitrile/Water Mixtures,” *Anal. Chem.*, vol. 63, no. 10, pp. 964–969, 1991, doi: 10.1021/ac00010a006.

[32] A. M. Brouwer, “Standards for photoluminescence quantum yield measurements in solution (IUPAC technical report),” *Pure Appl. Chem.*, vol. 83, no. 12, pp. 2213–2228, Aug. 2011, doi: 10.1351/PAC-REP-10-09-31/MACHINEREADABLECITATION/RIS.

[33] M. Fakis, P. Hrobárik, E. Stathatos, V. Giannetas, and P. Persephonis, “A time resolved fluorescence and quantum chemical study of the solar cell sensitizer D149,” *Dye. Pigment.*, vol. 96, no. 1, pp. 304–312, Jan. 2013, doi: 10.1016/J.DYEPIG.2012.07.025.

[34] J. C. Del Valle and J. Catalán, “Kasha’s rule: A reappraisal,” *Phys. Chem. Chem. Phys.*, vol. 21, no. 19, pp. 10061–10069, 2019, doi: 10.1039/c9cp00739c.

[35] Y. Zhang, Y. Duan, and T. Wang, “Excited-state hydrogen-bonding dynamics of camphorsulfonic acid doped polyaniline: A theoretical study,” *Phys. Chem. Chem. Phys.*, vol. 16, no. 47, pp. 26261–26265, Nov. 2014, doi: 10.1039/c4cp04267k.

[36] N. Sharma, S. K. Jain, and R. C. Rastogi, “Excited-state dipole moments of indoles using solvatochromic shift methods: An experimental and theoretical study,” *Bull. Chem. Soc. Jpn.*, vol. 76, no. 9, pp. 1741–1746, 2003, doi: 10.1246/bcsj.76.1741.

[37] T. Le Bahers, T. Pauporté, G. Scalmani, C. Adamo, and I. Ciofini, “A TD-DFT investigation of ground and excited state properties in indoline dyes used for dye-sensitized solar cells,” *Phys. Chem. Chem. Phys.*, vol. 11, no. 47, pp. 11276–11284, 2009, doi: 10.1039/b914626a.

[38] C. Wohlfahrt, “Static Dielectric Constants of Pure Liquids and Binary Mixtures,” in *Landolt-Börnstein – Group IV Physical Chemistry*, O. Madelung, Ed. 2002.

[39] C. Albrecht, “Joseph R. Lakowicz: Principles of fluorescence spectroscopy, 3rd Edition,” *Anal. Bioanal. Chem. 2007 3905*, vol. 390, no. 5, pp. 1223–1224, Jan. 2008, doi: 10.1007/S00216-007-1822-X.

[40] A. M. El-Zohry and B. Zietz, “Concentration and solvent effects on the excited state dynamics of the solar cell dye D149: The special role of protons,” *J. Phys. Chem. C*, vol. 117, no. 13, pp. 6544–6553, Apr. 2013, doi: 10.1021/jp400782g.

[41] A. M. El-Zohry and B. Zietz, “Electron Dynamics in Dye-Sensitized Solar Cells Influenced by Dye-Electrolyte Complexation,” *J. Phys. Chem. C*, vol. 124, no. 30, pp. 16300–16307, Jul. 2020, doi: 10.1021/acs.jpcc.0c03436.

[42] N. Boens *et al.*, “Fluorescence lifetime standards for time and frequency domain fluorescence spectroscopy,” *Anal. Chem.*, vol. 79, no. 5, pp. 2137–2149, Mar. 2007, doi: 10.1021/ac062160k.

[43] PicoQuant, *FluoFit: User’s Manual and Technical Data*, Version 4. .

[44] A. M. El-Zohry, D. Roca-Sanjuán, and B. Zietz, “Ultrafast twisting of the indoline donor unit utilized in solar cell dyes: Experimental and theoretical studies,” *J. Phys. Chem. C*, vol. 119, no. 5, pp. 2249–2259, Feb. 2015, doi: 10.1021/JP505649S/SUPPL_FILE/JP505649S_SI_001.PDF.

[45] A. El-Zohry, A. Orthaber, and B. Zietz, “Isomerization and aggregation of the solar cell dye D149,” *J. Phys. Chem. C*, vol. 116, no. 50, pp. 26144–26153, Dec. 2012, doi: 10.1021/jp306636w.

[46] A. M. El-Zohry, S. Agrawal, F. De Angelis, M. Pastore, and B. Zietz, “Critical

Role of Protons for Emission Quenching of Indoline Dyes in Solution and on Semiconductor Surfaces," *J. Phys. Chem. C*, vol. 124, no. 39, pp. 21346–21356, Oct. 2020, doi: 10.1021/acs.jpcc.0c07099.

[47] J. Sobuš, J. Karolczak, D. Komar, J. A. Anta, and M. Ziółek, "Transient states and the role of excited state self-quenching of indoline dyes in complete dye-sensitized solar cells," *Dye. Pigment.*, vol. 113, pp. 692–701, Feb. 2015, doi: 10.1016/j.dyepig.2014.10.008.

[48] R. Berera, R. van Grondelle, and J. T. M. Kennis, "Ultrafast transient absorption spectroscopy: Principles and application to photosynthetic systems," *Photosynthesis Research*, vol. 101, no. 2–3. Springer, pp. 105–118, Sep. 04, 2009, doi: 10.1007/s11120-009-9454-y.

[49] A. Maciejewski *et al.*, "Transient absorption experimental set-up with femtosecond time resolution. Femto- and picosecond study of DCM molecule in cyclohexane and methanol solution," in *Journal of Molecular Structure*, Nov. 2000, vol. 555, no. 1–3, pp. 1–13, doi: 10.1016/S0022-2860(00)00582-2.

[50] J. E. Ikpesu, S. E. Iyuke, M. Daramola, and A. O. Okewale, "Synthesis of improved dye-sensitized solar cell for renewable energy power generation," *Solar Energy*, vol. 206. Pergamon, pp. 918–934, Aug. 01, 2020, doi: 10.1016/j.solener.2020.05.002.

[51] N. I. A. Shukor *et al.*, "A Green Approach to Natural Dyes in Dye-Sensitized Solar Cells," *Sensors (Basel).*, vol. 23, no. 20, p. 8412, Oct. 2023, doi: 10.3390/s23208412.

[52] D. Javiya *et al.*, "Studies and comparison of natural dye-sensitized solar cells and thin-film solar cells," in *Materials Today: Proceedings*, Jan. 2023, vol. 73, pp. 545–549, doi: 10.1016/j.matpr.2022.10.222.

[53] C. L. Lee, W. H. Lee, and C. H. Yang, "High efficiency of dye-sensitized solar cells based on ruthenium and metal-free dyes," *Int. J. Photoenergy*, vol. 2013, no. 1, p. 250397, Jan. 2013, doi: 10.1155/2013/250397.

[54] S. Rahman *et al.*, "Research on dye sensitized solar cells: recent advancement toward the various constituents of dye sensitized solar cells for efficiency enhancement and future prospects," *RSC Advances*, vol. 13, no. 28. Royal Society

of Chemistry, pp. 19508–19529, Jun. 28, 2023, doi: 10.1039/d3ra00903c.

[55] B. S. Arslan *et al.*, “Optimization of fabrication parameters for efficient dye-sensitized solar cells based on dyes containing benzothiadiazole, indoline, and their co-sensitization,” *Electrochim. Acta*, vol. 458, p. 142523, Aug. 2023, doi: 10.1016/j.electacta.2023.142523.

[56] L. J. G. W. van Wilderen, C. N. Lincoln, and J. J. van Thor, “Modelling Multi-Pulse Population Dynamics from Ultrafast Spectroscopy,” *PLoS One*, vol. 6, no. 3, p. e17373, 2011, doi: 10.1371/JOURNAL.PONE.0017373.

[57] G. Nass Kovacs *et al.*, “Three-dimensional view of ultrafast dynamics in photoexcited bacteriorhodopsin,” *Nat. Commun. 2019 101*, vol. 10, no. 1, pp. 1–17, Jul. 2019, doi: 10.1038/s41467-019-10758-0.

[58] T. D. Green and K. L. Knappenberger, “Relaxation dynamics of Au25L18 nanoclusters studied by femtosecond time-resolved near infrared transient absorption spectroscopy,” *Nanoscale*, vol. 4, no. 14, pp. 4111–4118, Jun. 2012, doi: 10.1039/c2nr31080e.

[59] M. Fakis, E. Stathatos, G. Tsigaridas, V. Giannetas, and P. Persephonis, “Femtosecond decay and electron transfer dynamics of the organic sensitizer d149 and photovoltaic performance in quasi-solid-state dye-sensitized solar cells,” *J. Phys. Chem. C*, vol. 115, no. 27, pp. 13429–13437, Jul. 2011, doi: 10.1021/jp201143n.

[60] I. H. M. Van Stokkum, D. S. Larsen, and R. Van Grondelle, “Global and target analysis of time-resolved spectra,” *Biochimica et Biophysica Acta - Bioenergetics*, vol. 1657, no. 2–3. Elsevier, pp. 82–104, Jul. 09, 2004, doi: 10.1016/j.bbabio.2004.04.011.

[61] M. Ziólek, M. Lorenc, and R. Naskrecki, “Determination of the temporal response function in femtosecond pump-probe systems,” *Appl. Phys. B Lasers Opt.*, vol. 72, no. 7, pp. 843–847, 2001, doi: 10.1007/S003400100587/METRICS.

[62] J. S. Beckwith, C. A. Rumble, and E. Vauthey, “Data analysis in transient electronic spectroscopy–an experimentalist’s view,” *International Reviews in Physical Chemistry*, vol. 39, no. 2. Taylor & Francis, pp. 135–216, Apr. 02, 2020, doi: 10.1080/0144235X.2020.1757942.

[63] S. Ito *et al.*, “High-conversion-efficiency organic dye-sensitized solar cells with a novel indoline dye,” *Chem. Commun.*, no. 41, pp. 5194–5196, 2008, doi: 10.1039/b809093a.

[64] E. Rohwer *et al.*, “Ultrafast Photodynamics of the Indoline Dye D149 Adsorbed to Porous ZnO in Dye-Sensitized Solar Cells,” *ChemPhysChem*, vol. 14, no. 1, pp. 132–139, Jan. 2013, doi: 10.1002/CPHC.201200715.

[65] V. Novelli, N. Barbero, C. Barolo, G. Viscardi, M. Sliwa, and F. Sauvage, “Electrolyte containing lithium cation in squaraine-sensitized solar cells: Interactions and consequences for performance and charge transfer dynamics,” *Phys. Chem. Chem. Phys.*, vol. 19, no. 40, pp. 27670–27681, Oct. 2017, doi: 10.1039/c7cp04340f.

[66] S. Singh, Z. H. Khan, M. B. Khan, P. Kumar, and P. Kumar, “Quantum dots-sensitized solar cells: a review on strategic developments,” *Bulletin of Materials Science*, vol. 45, no. 2. Springer, pp. 1–13, Jun. 01, 2022, doi: 10.1007/s12034-022-02662-z.

[67] F. Matteocci *et al.*, “Wide bandgap halide perovskite absorbers for semi-transparent photovoltaics: From theoretical design to modules,” *Nano Energy*, vol. 101, p. 107560, Oct. 2022, doi: 10.1016/j.nanoen.2022.107560.

[68] W. Naim *et al.*, “Transparent and Colorless Dye-Sensitized Solar Cells Exceeding 75% Average Visible Transmittance,” vol. 15, p. 59, 2023, doi: 10.1021/jacsau.1c00045.

[69] A. Ebenezer Anitha and M. Dotter, “A Review on Liquid Electrolyte Stability Issues for Commercialization of Dye-Sensitized Solar Cells (DSSC),” *Energies*, vol. 16, no. 13. Multidisciplinary Digital Publishing Institute, p. 5129, Jul. 03, 2023, doi: 10.3390/en16135129.

[70] A. Agrawal, S. A. Siddiqui, A. Soni, and G. D. Sharma, “Advancements, frontiers and analysis of metal oxide semiconductor, dye, electrolyte and counter electrode of dye sensitized solar cell,” *Solar Energy*, vol. 233. Pergamon, pp. 378–407, Feb. 01, 2022, doi: 10.1016/j.solener.2022.01.027.

[71] B. K. Korir, J. K. Kibet, and S. M. Ngari, “A review on the current status of dye-sensitized solar cells: Toward sustainable energy,” *Energy Science and*

Engineering, vol. 12, no. 8. John Wiley & Sons, Ltd, pp. 3188–3226, Aug. 01, 2024, doi: 10.1002/ese3.1815.

[72] M. Grätzel, “Dye-sensitized solar cells,” *J. Photochem. Photobiol. C Photochem. Rev.*, vol. 4, no. 2, pp. 145–153, Oct. 2003, doi: 10.1016/S1389-5567(03)00026-1.

[73] J. Wu *et al.*, “Counter electrodes in dye-sensitized solar cells,” *Chemical Society Reviews*, vol. 46, no. 19. Royal Society of Chemistry, pp. 5975–6023, Oct. 02, 2017, doi: 10.1039/c6cs00752j.

[74] G. Richhariya, A. Kumar, A. K. Shukla, K. N. Shukla, and B. C. Meikap, “Effect of Different Counter Electrodes on Power Conversion Efficiency of DSSCs,” *Journal of Electronic Materials*, vol. 52, no. 1. Springer, pp. 60–71, Jan. 01, 2023, doi: 10.1007/s11664-022-09973-1.

[75] N. A. Karim, U. Mehmood, H. F. Zahid, and T. Asif, “Nanostructured photoanode and counter electrode materials for efficient Dye-Sensitized Solar Cells (DSSCs),” *Solar Energy*, vol. 185. Pergamon, pp. 165–188, Jun. 01, 2019, doi: 10.1016/j.solener.2019.04.057.

[76] C. I. Oprea *et al.*, “Role of energy level alignment in solar cells sensitized with a metal-free organic dye: A combined experimental and theoretical approach,” *Phys. Status Solidi Appl. Mater. Sci.*, vol. 208, no. 10, pp. 2467–2477, 2011, doi: 10.1002/pssa.201127083.

[77] J. Lungu *et al.*, “Heterocyclic azodyes as pigments for dye sensitized solar cells - A combined experimental and theoretical study,” *J. Optoelectron. Adv. Mater.*, vol. 12, no. 9, pp. 1969–1975, 2010.

[78] L. Zhang and J. M. Cole, “Dye aggregation in dye-sensitized solar cells,” *J. Mater. Chem. A*, vol. 5, no. 37, pp. 19541–19559, Sep. 2017, doi: 10.1039/C7TA05632J.

[79] F. Xu, T. T. Testoff, L. Wang, and X. Zhou, “Cause, Regulation and Utilization of Dye Aggregation in Dye-Sensitized Solar Cells,” *Mol. 2020, Vol. 25, Page 4478*, vol. 25, no. 19, p. 4478, Sep. 2020, doi: 10.3390/MOLECULES25194478.

[80] A. F. Buene, D. M. Almenningen, A. Hagfeldt, O. R. Gautun, and B. H. Hoff, “First Report of Chenodeoxycholic Acid–Substituted Dyes Improving the Dye Monolayer Quality in Dye-Sensitized Solar Cells,” *Sol. RRL*, vol. 4, no. 4, p.

1900569, Apr. 2020, doi: 10.1002/solr.201900569.

[81] X. Jiang, T. Marinado, E. Gabrielsson, D. P. Hagberg, L. Sun, and A. Hagfeldt, "Structural Modification of organic dyes for efficient coadsorbent-free dye-sensitized solar cells," *J. Phys. Chem. C*, vol. 114, no. 6, pp. 2799–2805, Feb. 2010, doi: 10.1021/JP908552T/SUPPL_FILE/JP908552T_SI_005.TIF.

[82] P. Boyce, N. Eklund, S. Mangum, C. Saalfield, and L. Tang, "Minimum acceptable transmittance of glazing," *http://dx.doi.org/10.1177/14771535950270030201*, vol. 27, no. 3, pp. 145–152, Sep. 1995, doi: 10.1177/14771535950270030201.

[83] N. Kutlu, "Investigation of electrical values of low-efficiency dye-sensitized solar cells (DSSCs)," *Energy*, vol. 199, p. 117222, May 2020, doi: 10.1016/j.energy.2020.117222.

[84] S. Sarker, H. W. Seo, and D. M. Kim, "Calculating current density-voltage curves of dye-sensitized solar cells: A straight-forward approach," *J. Power Sources*, vol. 248, pp. 739–744, Feb. 2014, doi: 10.1016/j.jpowsour.2013.09.101.

[85] M. E. Ragoussi, M. Ince, and T. Torres, "Recent Advances in Phthalocyanine-Based Sensitizers for Dye-Sensitized Solar Cells," *European J. Org. Chem.*, vol. 2013, no. 29, pp. 6475–6489, Oct. 2013, doi: 10.1002/EJOC.201301009.

[86] M.-E. Ragoussi *et al.*, "Carboxyethynyl Anchoring Ligands: A Means to Improving the Efficiency of Phthalocyanine-Sensitized Solar Cells," *Angew. Chemie*, vol. 124, no. 18, pp. 4451–4454, Apr. 2012, doi: 10.1002/ANGE.201108963.

[87] M. Kimura *et al.*, "Molecular Design Rule of Phthalocyanine Dyes for Highly Efficient Near-IR Performance in Dye-Sensitized Solar Cells," *Chem. – A Eur. J.*, vol. 19, no. 23, pp. 7496–7502, Jun. 2013, doi: 10.1002/CHEM.201300716.

[88] M. Ince *et al.*, "Peripherally and axially carboxylic acid substituted subphthalocyanines for dye-sensitized solar cells," *Chem. - A Eur. J.*, vol. 20, no. 7, pp. 2016–2021, Feb. 2014, doi: 10.1002/CHEM.201303639.

[89] B. Verreet *et al.*, "A 4% Efficient Organic Solar Cell Using a Fluorinated Fused Subphthalocyanine Dimer as an Electron Acceptor," *Adv. Energy Mater.*, vol. 1, no. 4, pp. 565–568, Jul. 2011, doi: 10.1002/AENM.201100137.

[90] H. Gotfredsen *et al.*, “Donor−Acceptor-Functionalized Subphthalocyanines for Dye-Sensitized Solar Cells,” *ChemPhotoChem*, vol. 2, no. 11, pp. 976–985, Nov. 2018, doi: 10.1002/CPTC.201800135.

[91] W. NAIM, “A novel approach of selective near-IR dye-sensitized solar cells as colorless and transparent photovoltaics : aesthetic evaluation and performance optimization,” Université de Picardie Jules Verne, 2022.

Chapter 2: Python-based software for the spectral modelling of femtosecond transient absorption data: a transition from the photosensitizers photochemistry to the solar cells.

This second chapter is to be read as an interface between the fundamental photodynamic investigations we lead on an organic photosensitizer D205 and the dye-sensitized-solar-cells last chapter in which photovoltaic characteristics are linked to photophysical behavior of real working solar cells. Advances in laser and computational technology have enabled precise recording and analysis of molecular dynamics in ultrafast spectroscopy, particularly within femtosecond transient absorption studies. Here, we introduce a Python-based software toolbox specifically designed for analyzing time-dependent data from ultrafast pump-probe experiments. This toolbox features a graphical interface that supports the application of various reaction models and the generation of coupled differential equations, facilitating global analysis of complex data. By employing advanced group velocity dispersion (GVD) correction and incorporating both Gaussian and exponential functions convoluted with Gaussian profiles, the software provides robust modelling capabilities. Additionally, it includes functionalities to manage Raman spectra, solvent dispersion effects, and interaction with transient phases, addressing challenges unique to ultrafast spectroscopy. Using D205 dye in multiple solvents as a case study, we demonstrate the toolbox's ability to accurately capture solvent-dependent photophysics, providing insights essential for optimizing dye-sensitized solar cell performance. Furthermore, the application of the software to perovskite-based solar cells is presented, showcasing its versatility in handling different systems and enabling the analysis of complex dynamics in photovoltaic devices. In summary, this work highlights a comprehensive tool for modelling and interpreting ultrafast spectroscopic data, enhancing our understanding of transient molecular processes and enabling deeper exploration of photophysical behaviors critical to applied photochemistry and renewable energy research.

1. Introduction

Dye-Sensitized Solar Cells (DSSCs) demonstrate considerable potential for commercial application among diverse renewable energy sources [50]–[54]. They belong to an innovative category of photovoltaic cell designed to effectively capture solar energy under diverse lighting situations, both indoors and outdoors. An optimization of DSSC efficiency is a key issue to deal with before proceeding to up-scale production. An understanding of the dye's photophysics and its solvation before and after the excitation is crucial to advancing the design of these DSSC components [12], [40], [55].

To delve into these interactions, an ultrafast technique is crucial. Femtosecond Transient Absorption Spectroscopy (Femto TAS) is a research area that provides essential information about the mechanical and kinetic details of chemical events that occur on a fast timescale. TAS setup presents a pump-probe ultrafast technique used to measure the absorption energies of the photo-generated excited states and photoproducts, as well as the associated lifetimes of the molecules. It allows for the analysis of biomolecular dynamics through detailed modelling of populations interacting with multiple well-characterized pulses [56]. This method allows the distinction between species that decay directly to the ground state and those forming an intermediate state before reaching the ground state [18], [57]. Time-resolved TAS sheds light on the dynamics of nanoclusters, where the dominant relaxation mechanism is a non-radiative core-to-ligand energy transfer occurring on a timescale of a few picoseconds [58]. The pump-prob technique is a powerful tool for investigating the electron transfer dynamics of the organic sensitizer [47], [59].

Despite its efficiency, the analysis of transient absorption data presents many challenges. The resulting datasets tend to be high-dimensional, including both temporal and spectral data, requiring sophisticated approaches for precise interpretation. Although current software solutions like Glotaran [60], Origin (OriginLab, Northhampton, MA, USA), Bio-Kine32 (Bio-Logic, Claix, France), and Surface Xplorer (Ultra-fast Systems LLC) are extensively utilized for TA data analysis, they often suffer from restricted flexibility, user accessibility issues, or an absence of specialized functionality for specific experimental configurations [61], [62]. Considering these limitations, the development of a customized software toolbox became important to address research requirements and optimize the analytical procedure.

Python, more than most other languages, provides ready-made capabilities for current trendy technologies such as data science, machine learning, and artificial intelligence. By installing Python, it comes with the core Python language. But to avoid the need to remake the code, users can import different modules that are already prewritten specialized code collections. Those modules are called Python libraries and have a very easy way of utilizing them by simply using the import command and following the command with the name of the module needed and that's what makes Python a modular language.

The Python-based software toolbox introduced in this study aims to optimize the program code using object-oriented programming (OOP), which enhances readability, improves efficiency, and includes a code segment for recognizing input file formats. This toolbox differs from existing packages by incorporating advanced global analysis of time-resolved spectroscopic data and the ability to perform group velocity dispersion (GVD) correction. Additionally, it features a connectivity scheme that can be graphically designed, and a user-friendly graphical interface that simplifies the learning curve for global fitting.

Featuring a user-friendly graphical interface, the toolbox streamlines the application of various reaction models to the data, enabling the generation of coupled differential equations. It allows the analysis of any time-dependent dataset to extract time-independent correlations of observables using GVD-modified Gaussian and exponential functions. Additionally, the toolbox boasts specific functionalities, such as removing the pump-probe signal without harming the sample signal, removing bad single spectra, considering Raman signals, and tailored for analyzing ultrafast pump-probe spectroscopic data. In essence, the described toolbox makes it possible to globally fit all data, or a noise-reduced subset of it.

2. Mathematical models

The FemtoFit program incorporated various mathematical models, which, based on the physical nature of the signal, were classified into distinct categories: solvent Raman processes (involving vibrational level transitions) and electronic level transitions. Furthermore, the incorporation of the in-cell group velocity dispersion (GVD) effect led to two different function types. These include models that either considered or ignored the GVD effect, resulting in the distinction between Gaussian and exponential functions convoluted with a Gaussian, and GVD-modified Gaussian and exponential functions convoluted with a modified Gaussian [61]. The latter is detailed in the Annex.

2.1. Gaussian and exponential functions are convoluted with a Gaussian

To process Raman signal data, the Gaussian function described in Equation (11) is proposed:

$$S(t) = y_0 + A_R \cdot \frac{1}{\sigma\sqrt{2\pi}} exp\left(-\frac{(t-t_0)^2}{2\sigma^2}\right) \tag{11}$$

The value of σ is defined by Equation (12):

$$\sigma = \frac{\tau_{FWHM}}{2\sqrt{2\ln(2)}} \tag{12}$$

To describe the electronic level transition signals, the exponential functions were convoluted with the Gaussian as shown in Equation (13):

$$S(t) = y_0 + \frac{A_1}{2} exp\left(-\frac{1}{\tau_1}\left(t - t_0 - \frac{\sigma^2}{2\tau_1}\right)\right) \cdot \left(1 + erf\left(\frac{t-t_0-\frac{\sigma^2}{\tau_1}}{\sqrt{2}\sigma}\right)\right) \tag{13}$$

For more complex systems, Equation (14) shows the available multiexponential function, with n ranging from 1 to 5:

$$S(t) = y_0 + \sum_{n=1}^{n} \frac{A_n}{2} exp\left(-\frac{1}{\tau_n}\left(t - t_0 - \frac{\sigma^2}{2\tau_n}\right)\right) \cdot \left(1 + erf\left(\frac{t-t_0-\frac{\sigma^2}{\tau_n}}{\sqrt{2}\sigma}\right)\right) \tag{14}$$

The exponential functions include a term to mimic the lifetime of a triplet state (or another very long-lived state) y_{inf}:

$$\frac{y_{inf}}{2} exp\left(-\frac{1}{10^6}\left(t - t_0 - \frac{\sigma^2}{2\tau_n}\right)\right) \cdot \left(1 + erf\left(t - t_0 - \frac{\sigma^2}{10^6}\right)\right) \tag{15}$$

If Raman signals are present in the measurement, the Raman checkbox must be selected, adding the term from Equation (11). This results in the Equation (16):

$$S(t) = y_0 + \sum_{n=1}^{n} \frac{A_n}{2}\, exp\left(-\frac{1}{\tau_n}\left(t - t_0 - \frac{\sigma^2}{2\tau_n}\right)\right) \cdot \left(1 + erf\left(\frac{t - t_0 - \frac{\sigma^2}{\tau_n}}{\sqrt{2}\sigma}\right)\right) + A_R \cdot \frac{1}{\sigma\sqrt{2\pi}} exp\left(-\frac{(t-t_0)^2}{2\sigma^2}\right) \quad (16)$$

In some cases, the Gaussian shape is absent, and in such instances, numerical convolution can be used. However, this approach comes with drawbacks, such as the need for more computationally expensive programs and longer processing times. The impulse response function (IRF) in femtosecond transient absorption originates from the laser pulse, which has a Gaussian profile, resulting in a Gaussian IRF. This leads to semi-analytical expressions for the output signal. In contrast, instruments like TCSPC, the IRF originates from the detector. This scenario is considered simpler, as no group velocity dispersion (GVD) is present. However, there are cases where GVD is present within the cell, adding more complexity to the analysis.

2.2. GVD correction

The early times are strongly affected by group velocity dispersion (GVD), so it is essential to apply at least a minimal correction to proceed with the data treatment. GVD arises from the difference in the group velocity of light with varying energy (wavelength) in condensed matter, causing red wavelengths (lower energy) to propagate faster than blue wavelengths (higher energy). In transient absorption, spectra are taken at different delay times, and the velocity effect results in the blue wavelengths appearing first in the spectrum, while red wavelengths appear later. To correct for GVD, an approximate adjustment can be made by shifting the zero time for each wavelength. This correction can be applied by entering the thickness of the condensed matter in millimeters, and the correction will be calculated using dispersion curves available in the literature.

The following equations 17, 18 and 19 are used to calculate the dispersion curves for specific materials: BK7, SiO_2, and CaF_2. These materials, each with their unique optical properties, exhibit different GVD behaviors, which are described by the respective equations. In these equations, wavelength (λ) is given in micrometers, and l represents the thickness of the condensed phase.

For BK7, a type of optical glass commonly used in lenses and prisms:

$$\Delta t, \mathrm{ps} = l \cdot \frac{\sqrt{\frac{1.03961212\cdot\lambda^2}{\lambda^2-0.00600069867}+\frac{0.231792344\cdot\lambda^2}{\lambda^2-0.0200179144}+\frac{1.01046945\cdot\lambda^2}{\lambda^2-103.560653}+1}}{0.299792458} \quad (17)$$

For SiO_2, often used in cuvettes and optical fibers:

$$\Delta t, \mathrm{ps} = l \cdot \frac{\sqrt{\frac{0.6961663 \cdot \lambda^2}{\lambda^2 - 0.0046791482} + \frac{0.4079426 \cdot \lambda^2}{\lambda^2 - 0.0135120631} + \frac{0.8974794 \cdot \lambda^2}{\lambda^2 - 97.9340025} + 1}}{0.299792458} \tag{18}$$

For CaF_2, used in applications requiring transparency in the ultraviolet to infrared range:

$$\Delta t, \mathrm{ps} = l \cdot \frac{\sqrt{\frac{0.5675888 \cdot \lambda^2}{\lambda^2 - 0.050263605^2} + \frac{0.4710914 \cdot \lambda^2}{\lambda^2 - 0.1003909^2} + \frac{3.8484723 \cdot \lambda^2}{\lambda^2 - 34.649040^2} + 1}}{0.299792458} \tag{19}$$

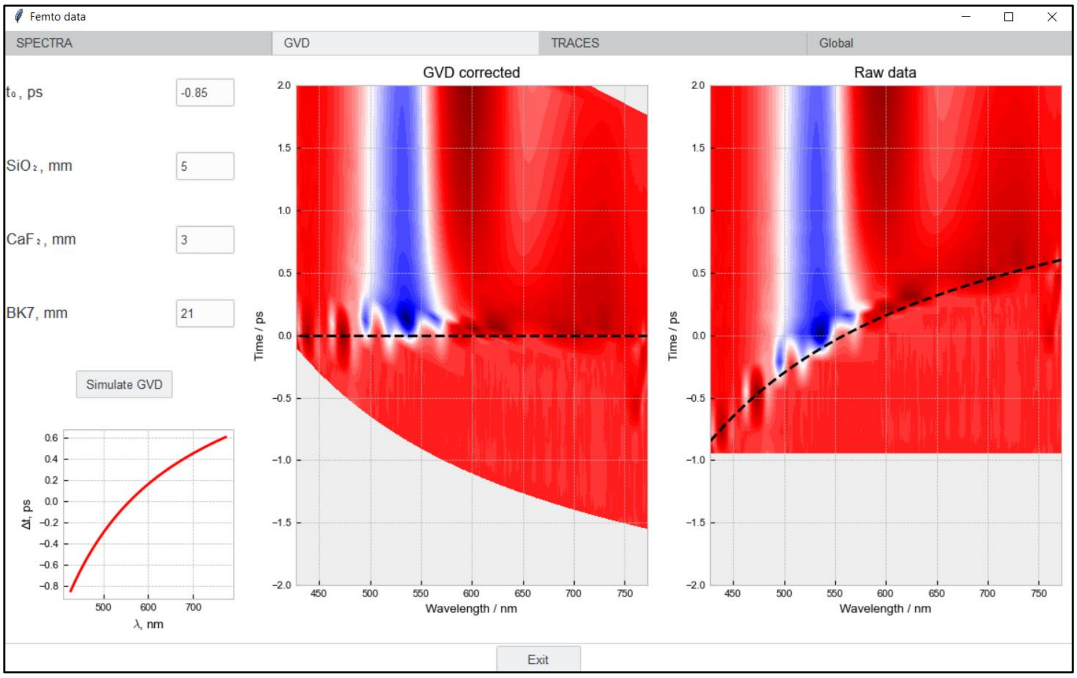

t_0, ps: -0.85

SiO_2, mm: 5

CaF_2, mm: 3

BK7, mm: 21

Figure 18. GVD correction applied to transient absorption data.

Figure 18 shows a comparison between raw data and GVD-corrected data for a transient absorption measurement. On the left, the "GVD corrected" panel shows the data after applying the correction, with the time delays for each wavelength adjusted. On the right, the "Raw data" panel displays the original, uncorrected data. The graph at the bottom left shows the simulated dispersion curve, representing the relationship between wavelength and time shift due to GVD. The different values for the thickness of SiO_2, CaF_2, and BK7 are indicated in the input fields. The dotted line in both plots represents the baseline for time comparison.

The goal of this work is to develop the program and test it with challenging data, considering all the complex stages of data processing, including primary processing, GVD correction, model selection, and optimization of model parameters. This ensures the creation of a program capable of handling data efficiently and correctly. The accuracy of the program is guaranteed by the models used to interpret experimental data and by thoroughly testing each functionality at every stage of processing. If errors are detected in the program's operation, corrective measures are suggested.

3. Global Fit and analysis of model data

3.1. Python-based spectral modelling software

To optimize the program's code and increase its speed, efficiency and flexibility in reading raw data, the object-oriented programming (OOP) designing language concept was used. The program's interface is structured into four distinct sections, each corresponding to a specific stage in the data processing process. These sections, or modules, are implemented as organized classes. The four tabs that correspond to these phases are SPECTRA, GVD, TRACES and Global, as illustrated in Table 5 and Figure 19.

Table 5. Overview of the program structure and implementation.

Program concept	Stages	Tabs	Modules
Data treatment stages needed	Primary Processing	***Spectra***	Spectra.py
	Group Velocity Dispersion (GVD) Correction	***GVD***	GVD.py
	Model Selection	***Traces***	Traces.py
	Optimization of Model Parameters	***Global***	Global.py

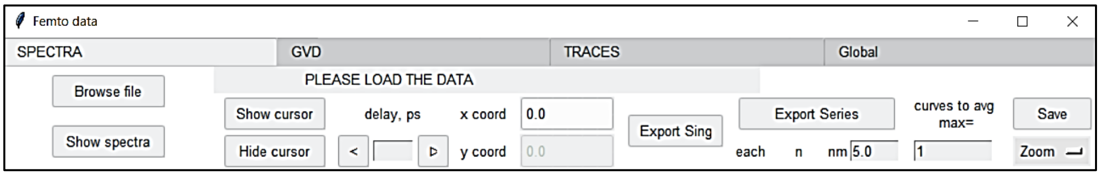

x coord 0.0

y coord 0.0

nm 5.0

curves to avg max= 1

Figure 19. Main window interface of the program: layout of the program's main window, highlighting its four tabs - SPECTRA, GVD, TRACES, and Global - each corresponding to a specific stage of data processing.

3.2. Data Treatment

An example dataset is analyzed to demonstrate the capabilities of the toolbox. The discrete steps required for a minimal analysis to elucidate the essential kinetics are detailed in the supplementary information. The initial step involves correcting the TA spectra by removing the pump signal from the graph, as illustrated in Figure 20. The spectral measurements show the absorption as a function of wavelength, covering a range of up to 800 nm.

As a next step in data treatment, the two possibilities are to export the kinetic traces. The choice depends on the complexity of the kinetic model. In cases involving simple kinetics, a direct analysis may be enough. However, for more complex photochemical processes, such as the one presented here, a combination of full femtosecond transient absorption measurements, additional spectroscopic experiments, and advanced global analysis is required - capabilities that this program provides.

In this case, an export series will be needed for detailed data analysis. To facilitate this process, a preprocessing step involves exporting individual traces to estimate lifetimes as a preliminary step before applying the export series, which utilizes the estimated lifetimes. Another essential preprocessing step is the group velocity dispersion (GVD) correction, as described earlier using the GVD Tab.

Once an approximate GVD correction is applied, the next stage of data treatment can proceed. In the TRACES section, meaningful initial guess parameters for the subsequent global fit can be generated using the right-side toolbar (Figure 21). The TRACES Tab also includes a utility for selecting fitting functions. As explained in the mathematical model’s section, Gaussian and exponential functions are available for modeling the experimental data. Raman fits can use only Gaussian functions, while several exponentials can be applied using the n-exp Gauss option in the function menu.

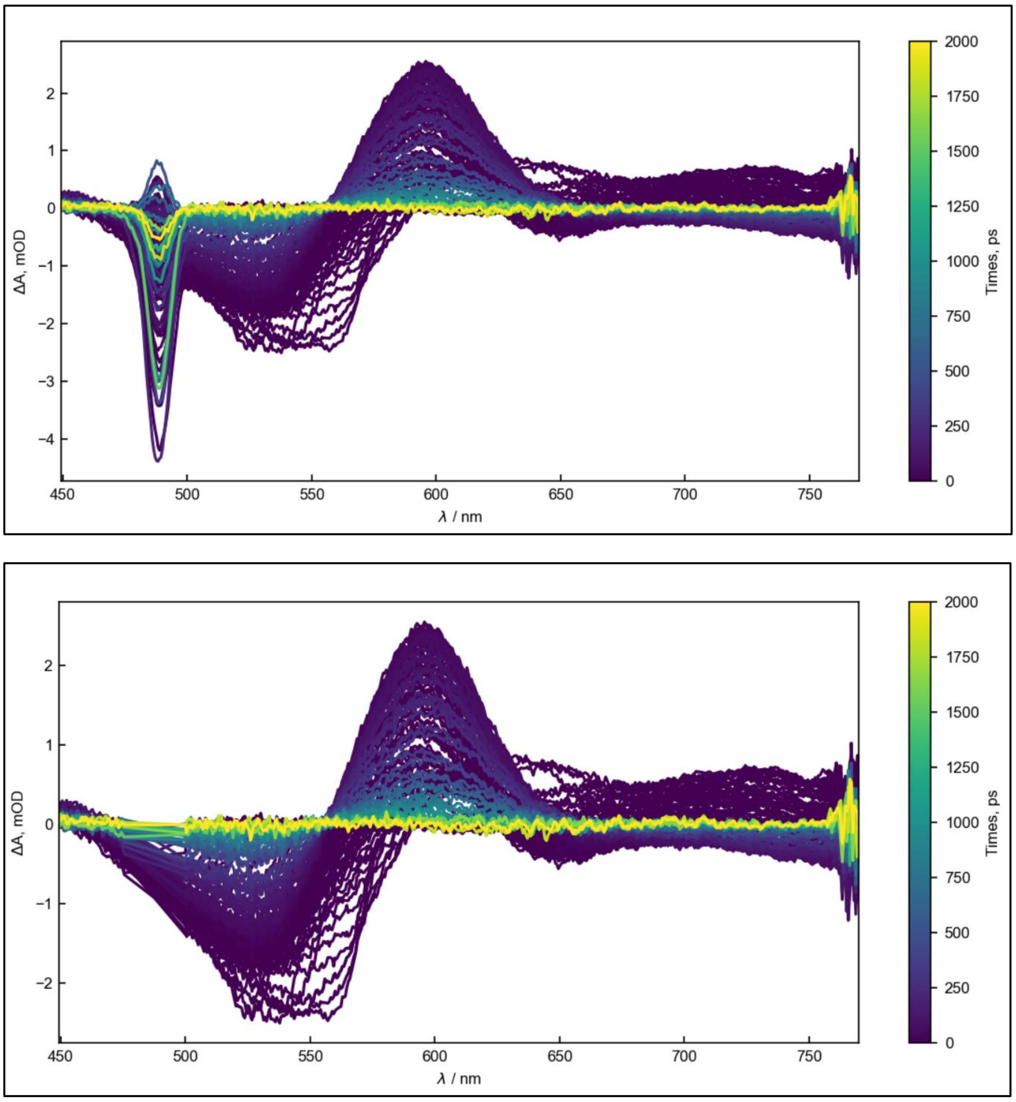

Figure 20. Correction of TA spectra by removing the pump component using FemtoFit

FemtoFit provides tools for excluding specific wavelength and time values directly on the SPECTRA and TRACES tabs (accessible via the top toolbar, highlighted with a blue rectangle in Figure 21). It is mandatory to specify the excitation wavelength in the λ_{exc} entry and enter the width of the BK7 glass in millimeters in the BK7 (mm) entry. The default optical path length is 1 mm. Additionally, the sample's absorbance at the excitation wavelength must be entered in the OD entry. The program also allows accounting for solvent effects using equations provided for treating solvent dispersion curves. Equation (20) describes the solvent dispersion correction [18]:

$$\tau_{GVD} = l \cdot \frac{(n_{probe} - n_{pump})}{0.2998} \tag{20}$$

where l is the thickness of the condensed phase, and n_{probe} and n_{pump} are the refractive indices of the probe and pump wavelengths in the solvent medium, respectively. Equations for handling multiple solvents and parameter values are provided in annex. In Figure 21, experimental data points are displayed as points, while the results of the initial guess parameters are represented by solid lines in the corresponding colors.

When the initial guess parameters are generated, a global fit can be performed. On the left side of Figure 22, a scrollable bar displays the best-fit parameters for each wavelength. For clarity, global parameters such as FWHM, time constants, and OD are only listed in the parameter set for the first wavelength. The parameters are displayed in editable entries, allowing the user to modify them as needed.

In the center of the "Global" tab, three graphs are presented: kinetic traces, where points represent experimental data and lines represent the fit; residuals as a function of time; and decay-associated spectra (DAS). The FemtoFit program dynamically updates these graphs after each "fit" or "refresh" action. The changes in residual values after parameter refinements indicate the quality of the fitting results, with the best fit minimizing residuals.

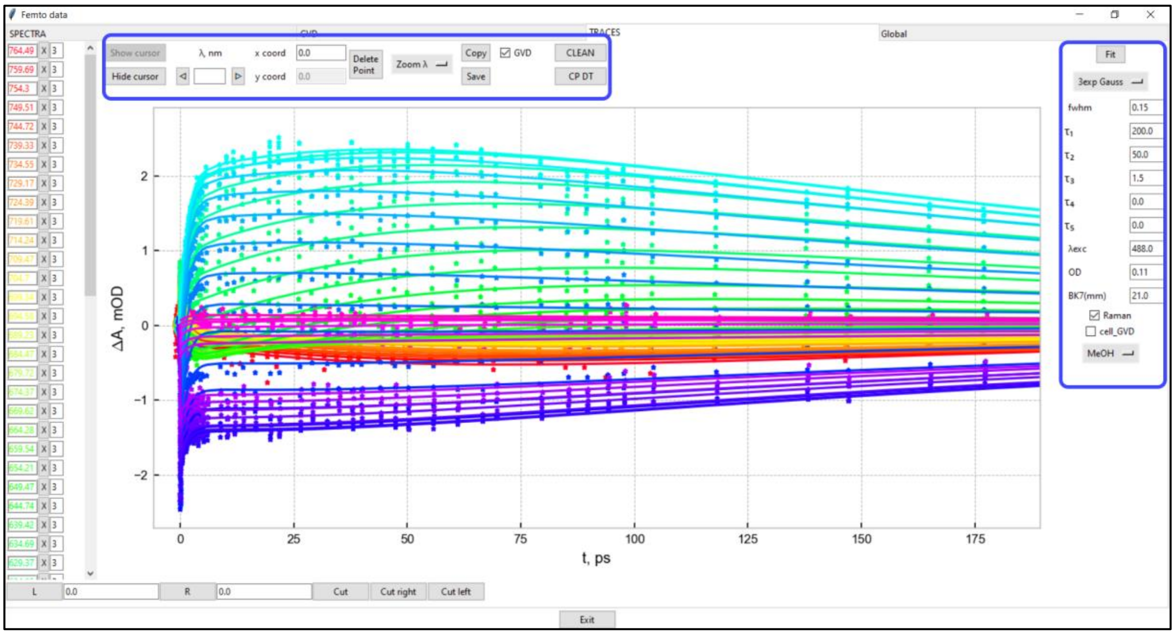

x coord 0.0
y coord 0.0
☑ GVD
3exp Gauss
fwhm 0.15
τ_1 200.0
τ_2 50.0
τ_3 1.5
τ_4 0.0
τ_5 0.0
λexc 488.0
OD 0.11
BK7(mm) 21.0
☑ Raman
☐ cell_GVD
MeOH
L 0.0
R 0.0

Figure 21. TRACES tab: initial guess parameters generated - functionality of the TRACES tab in the FemtoFit interface, where the first set of initial guess parameters is generated for global fitting. Experimental data points are shown as points, while the solid lines of corresponding colors represent the generated initial guess parameters.

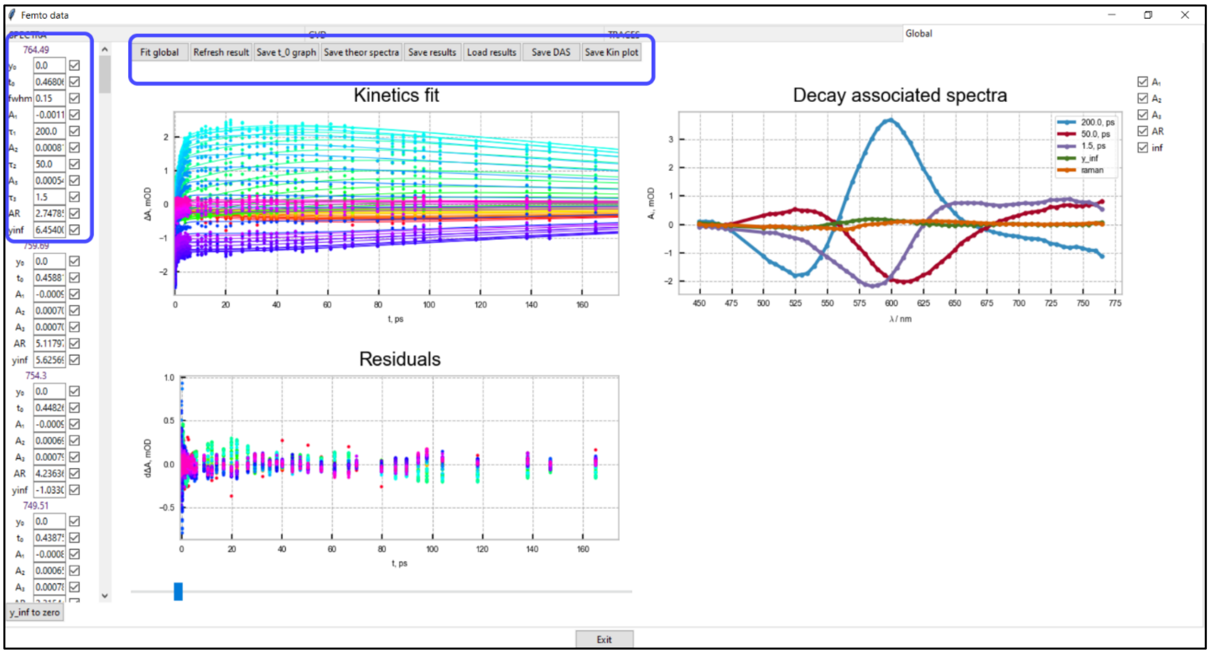

Figure 22. Global fit tab with highlighted fitting parameters and toolbar - the scrollable bar on the left side presents fitting parameters for each wavelength and the toolbar at the top provides saving functionalities. The central section features three graphs: kinetic traces (experimental data as points and fit as lines), residuals as a function of time, and decay-associated spectra (DAS).

The Levenberg-Marquardt algorithm is used for fitting. As a result, the parameter optimization outputs include χ^2 and χ^2_{red} statistics:

$$\chi^2 = \sum_i^N \left[y_{exp,i} - y_{theor,i}\right]^2 \tag{21}$$

$$\chi^2_{red} = \sum_i^N \frac{\left[y_{exp,i} - y_{theor,i}\right]^2}{N - N_{var}} \tag{22}$$

where N is the number of the experimental points, $y_{exp,i}$ is the experimental value, $y_{theor,i}$ is the theoretical model value, and N_{var} is the number of the optimized parameters. A good fit is indicated by lines closely following the experimental data and residuals showing no structure, remaining within the range of ±1 mOD.

The top panel includes several buttons for saving results. Users can save specific outputs, such as the wavelength dependence of τ_0 ("Save t_0 graph"), TA spectra calculated from the fit ("Save theor spectra"), decay-associated spectra as displayed ("Save DAS"), and experimental and theoretical kinetic traces ("Save Kin plot"). Upon saving, three output files are generated: result.json, a Python database format containing the raw results; result_pretty.txt, a user-friendly text file summarizing the fit results in an easily readable format; and result_wl.txt, a file storing the wavelength values for the traces. These files allow for further analysis and plotting in external visualization programs.

4. Test of the software on the photosensitizer D205

The well-known organic photosensitizer D205 was tested in three selected solvents: acetonitrile (ACN), methanol (MeOH), dimethyl sulfoxide (DMSO), and BmimBF4. The photophysical properties, such as the position and shape of absorption and emission spectra, excited state lifetimes, and other dynamic characteristics, are strongly influenced by the dye's environment. Therefore, it is essential to understand the solvent effects on the photophysical properties of organic photosensitizers, as these will affect the spectroscopic and photodynamic properties of DSSC photosensitizers and their efficiency. Consequently, the excited state lifetime of the dye varies depending on the processes it undergoes. To process the TA data in the presence of MeOH, AN, DMSO, and BmimBF4, the FemtoFit data analysis program was used. The method described earlier was applied to ensure the data was processed correctly.

Transient absorption spectroscopy of model dyes excited at 486 nm and 460 nm (for BmimBF4) was performed using the setup at the LASIRE laboratory, with a femtosecond Ti:sapphire laser system as the light source.

4.1. Signal Assignments

The TAS of D205 in DMSO shows the variation in absorbance, or $\Delta A(\lambda,t)$, as a function of probe wavelength. The $\Delta A(\lambda,t)$ measurement is the sum of three signal contributions from different physical phenomena. The transient absorption spectra of D205 in DMSO, ACN, MeOH, AN, and $BmimBF_4$ are shown in Figure 23 with the panels arranged from the fastest to the slowest decay.

Different signal assignments can be made from the initial spectra, allowing for the identification of lifetime components obtained after fitting. The band between λ=500-550 nm is attributed to the ground-state bleaching (GSB) or depopulation signal. The position of GSB was identified based on the steady-state absorption spectrum and is slightly blue-shifted for all solvents.

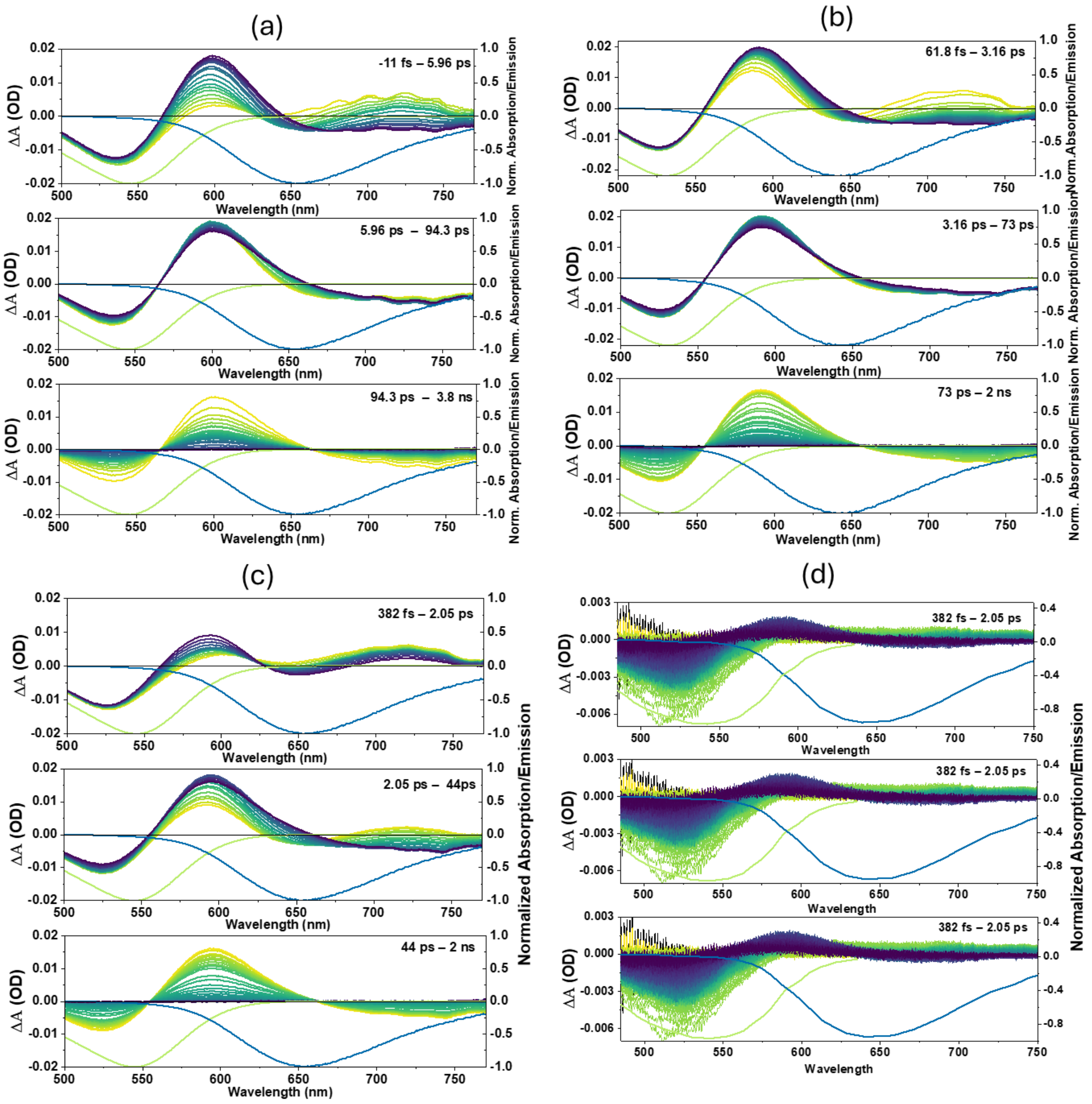

Figure 23. D205 transient absorption spectra in (a) DMSO, (b) ACN, (c) MeOH and (d) BmimBF4. The green and blue lines represent the scaled and intensity-inverted steady-state absorption and emission spectra of the solution, respectively.

The band centered at approximately λ=700-750 nm is assigned to the stimulated emission (SE) band, where molecules relax from the excited state to the ground state with light emission, if the probe beam possesses the specific energy, resulting in a negative band, as observed here. The SE band can also be identified using the steady-state fluorescence spectrum. Near λ=600 nm, the band indicates the excited-state absorption (EAS) band, which appears as a positive band.

At the initial short time intervals, we can observe spectra corresponding to solvation dynamics: absence of ground-state bleaching, blue-shifted stimulated emission, and positive amplitudes toward the red. Solvation dynamics, molecular geometry relaxation, and other processes may cause the shift in stimulated emission and other bands in the TA spectra. To attribute these possibilities, a multi-exponential global analysis can be performed to compare the decay-associated spectra with the steady-state spectra of the dye forms.

4.2. Global analysis

The best fit for most of the samples was achieved using both a three- and four-exponential model, with $\tau1$ consistently associated with excited state relaxation. The time constants are attributed to the following processes: Raman scattering (the fastest component below the time resolution), solvation dynamics, and the S_1 to S_0 transition.

One of the fast components, with values around 1.5 ps, is characteristic of solvation dynamics: absence of ground-state bleach, blue-shifted stimulated emission, and positive amplitudes toward the red. The fastest component (less than 1 ps, shown in green) exhibits Raman features with a broad Stokes contribution and positive amplitudes in the range of 650 nm to 730 nm. This suggests that this time component represents not only coherent artifacts but also part of the solvation dynamics within the time resolution of the setup.

The longest component, τ_1, corresponds to the relaxation of the excited state to the ground state. For methanol, the τ_1 value of 124.4 ps is shorter than that of D205 in DMSO ($\tau_1 = 419.2$ ps) and ACN ($\tau_1 = 340.5$ ps). This result is consistent with values reported in the literature, as well as for the nearly identical dye D149 [12], [18], [33], [37], [45], [63], [64].

The decay-associated spectra of D205 in BmimBF$_4$ are shown in Figure 24. The spectrum of the longest component ($\tau_1 = 988.9$ ps) closely resembles the steady-state absorption and emission spectra, corresponding to the relaxation of the excited state to the ground state. The three other components—$\tau_2 = 80.7$ ps, $\tau_3 = 5.0$ ps, and $\tau_4 = 0.08$ ps—display features characteristic of solvation dynamics. The component with $\tau_4 = 0.08$ ps also contains coherent artifacts due to BmimBF$_4$. Therefore, the photophysics of D205 in ionic liquid are very similar to its photophysics in organic solvents.

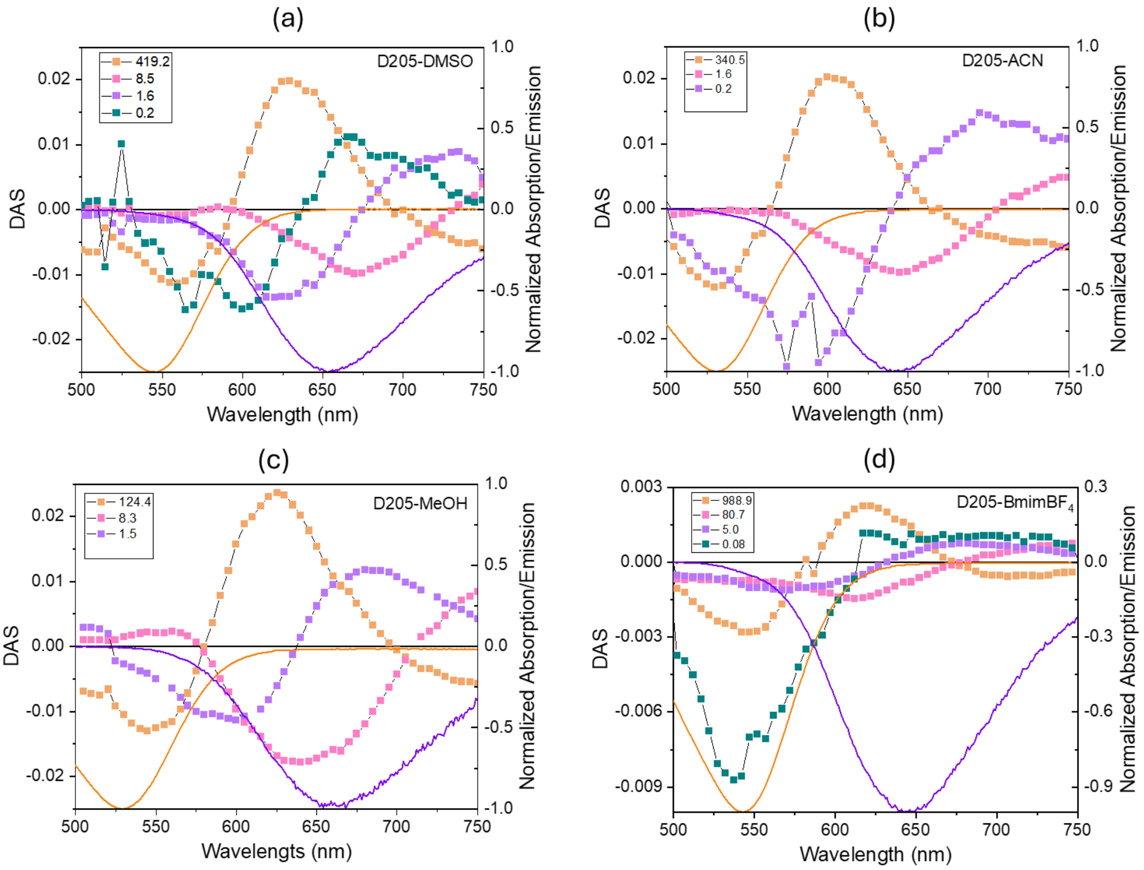

Figure 24. Decay-associated spectra of D205 in (a) DMSO, with time components of τ_1 = 419.2 ps, τ_2 = 8.5 ps, τ_3 = 1.6 ps and τ_4 = 0.2 ps; (b) ACN, with τ_1 = 340.5 ps, τ_2 = 1.6 ps, τ_3 = 0.2 ps; (c) in MeOH, with τ_1 = 124.4 ps, τ_2 = 8.3 ps, τ_3 = 1.5 ps; and (d) BmimBF$_4$, with τ_1 = 988.9 ps, τ_2 = 80.7 ps, τ_3 = 5.0 ps, and τ_4 = 0.08 ps.

5. Test of FemtoFit on Perovskite-based Solar Cells

This section presents an analysis of femtosecond transient absorption spectroscopy (TAS) performed on perovskite-based photovoltaic cells. Perovskite solar cells (PSCs) are promising technology for photovoltaic applications due to their high efficiency and low-cost fabrication methods. The ability to understand the photophysical processes occurring in these cells is crucial for improving their performance. TAS is particularly useful for investigating the dynamics of excited states in these materials, providing insights into charge generation, transport, and recombination mechanisms.

In this study, 720 nm and 450 nm wavelength were used to excite the samples, with probes in the visible and infrared regions, respectively. The use of different wavelengths allows for probing specific electronic transitions, and by analyzing the spectral evolution over time, we gain detailed information about the dynamics of various excited states and their relaxation processes. Optical density filters were used to regulate the energy reaching the samples, optimizing the spectra visualization. The samples were moved during measurements to ensure excitation of multiple regions, improving the representativeness of the analysis.

The transient absorption spectra were analyzed using the FemtoFit software, which is capable of fitting the data with exponential decay models, providing information about the time constants associated with different processes, such as solvation dynamics and the S_1 to S_0 transition.

A key aspect of this analysis is the exploration of FemtoFit's ability to analyze selected wavelengths either separately or together. By isolating specific wavelengths, we can focus on individual features of the transient absorption spectra, providing a more detailed and localized understanding of the dynamics at those wavelengths. Alternatively, when multiple wavelengths are analyzed simultaneously, the overall analysis becomes more efficient, allowing for a broader overview of the excited state processes across the entire spectrum.

This flexibility enables faster data processing and more precise analysis of the dynamics, particularly when dealing with complex spectra. The ability to perform both localized and global analyses is a powerful tool for investigating the temporal evolution of excited states in perovskite solar cells, providing insight into charge generation, transport, and recombination mechanisms.

5.1. Analysis with FemtoFit Software

In general, the spectra acquired through a 720 nm pump with probe in the visible range for different samples exhibit a similar configuration. A negative band appears around 470 nm, suggesting an association with the Ground State Bleach. Within the spectral range of 550 nm to 675 nm, two or three distinct positive bands can be observed, indicating potential connections with the excited state absorption. This particular observation highlights the need for a careful examination of previous research to identify the individual mechanisms associated with each of these positive discrete bands.

The FemtoFit software was used to fit the data by selecting specific wavelengths from the spectra that corresponded to the observed bands. To an excessive amount of data in this study, the results of only one analyzed sample, PK1_PMMA, will be presented. Figure 25 and Figure 26 show the spectra obtained from the TAS analysis, along with the kinetic curves derived from FemtoFit, and the time components associated with each curve. The reason for selecting wavelengths is to reduce the time required for analysis and, in some cases, to make the analysis feasible. Given that the sample may exhibit many complex dynamics, it is not always possible to analyze everything simultaneously, as the software struggles with too many components and overlapping processes.

The spectra obtained in the infrared region using a 450 nm pump presented a considerable challenge due to their low resolution, which made the analysis process difficult. Despite these limitations, a broad negative band covering approximately 1000 nm to 1300 nm was identified, with peaks concentrated between 1100 nm and 1200 nm. Achieving a satisfactory balance in pump energy using filters was particularly challenging for these tests, requiring a delicate balance to achieve high enough optical density without compromising the integrity of the sample.

Even with these technical challenges, FemtoFit software succeeded on making the adjustments. In this case, another approach for using the software is demonstrated, where specific wavelengths are selected, and all chosen wavelengths are considered together to perform a fitting, resulting in a single outcome. A distinct trend emerged in the results, indicating that the τ_1 time component generally showed higher values in these infrared analyses compared to the values derived from analyzing the dynamics occurring in the visible region.

Table 6. Kinetic fitting results for the perovskite-based solar cell sample PK1_PMMA using a 720 nm pump and visible range probe, as well as a 450 nm pump with infrared probe.

Pk1_PMMA								
Pump	**Probe**	**Fit at**	**A1**	**τ_1 (ps)**	**A2**	**τ_2 (ps)**	**A3**	**τ_3 (ps)**
720 nm	**Visible range**	473 nm	-3.31E-04	1225.9	-2.34E-04	69.1	-1.92E-04	3.2
		617 nm	5.07E-04	1344	5.81E-04	143.3	1.65E-04	3.7
		755 nm	-3.00E-03	1837	-2.31E-03	171.3	-2.29E-04	7.7
		770 nm	-1.99E-03	1006.8	-9.06E-04	58.2	3.13E-03	0.31
450 nm	**Infrared**	605 nm, 575 nm, 535 nm	3.59E-03	69.019	2.07E-03	2.702	-	-

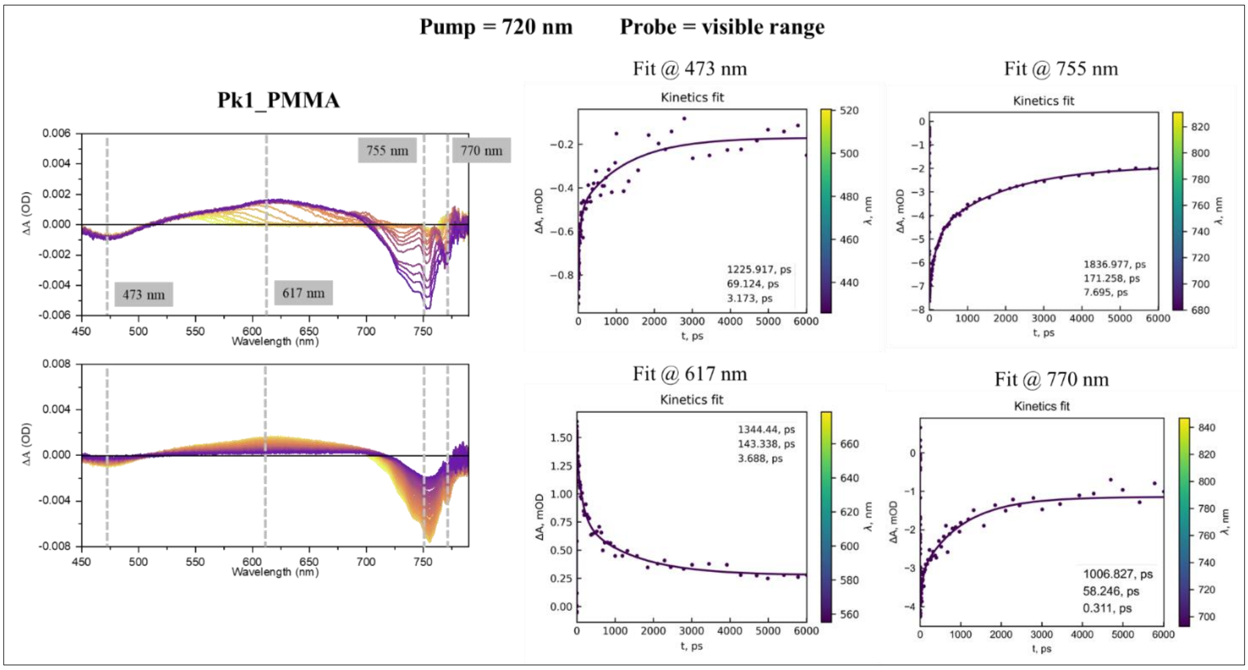

Figure 25. Spectra obtained with a 720 nm pump in the visible range for a perovskite-based solar cell device, along with the kinetic curves derived from FemtoFit software by fitting selected wavelengths of interest separately.

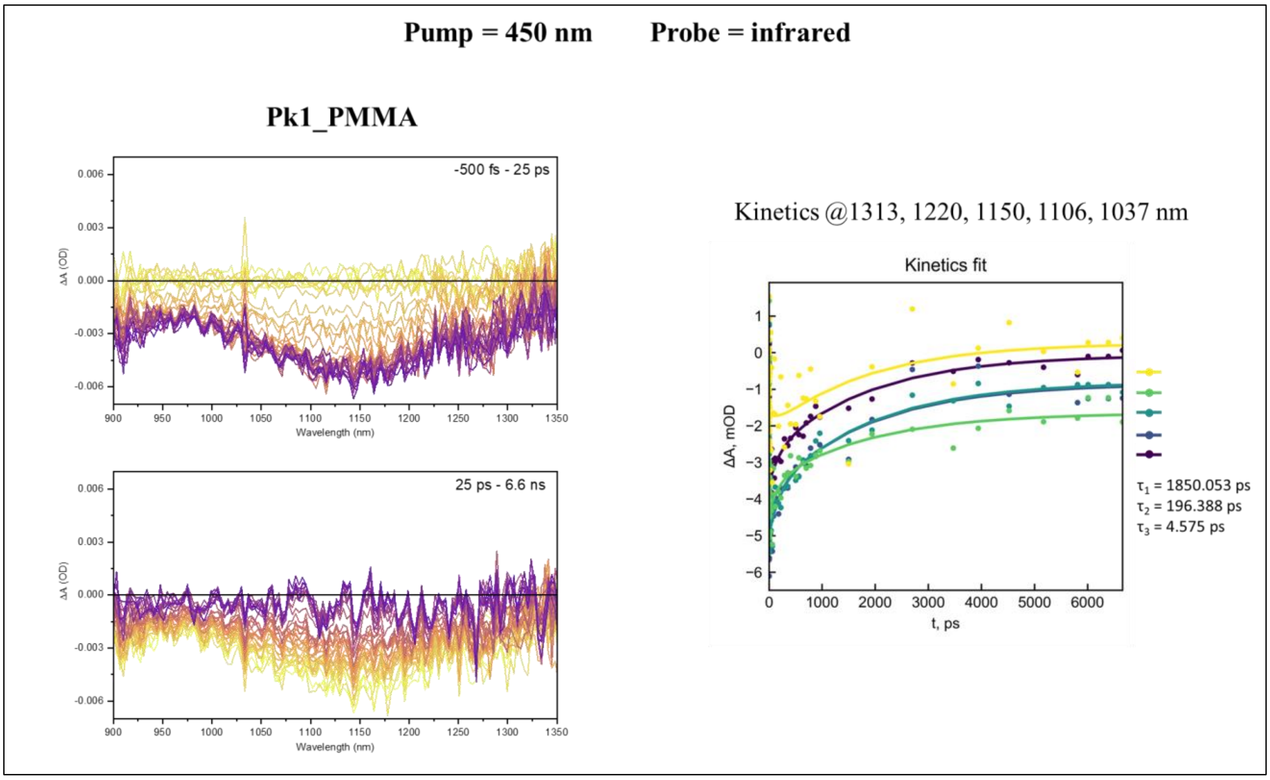

Figure 26. Spectra obtained with a 450 nm pump in the infrared range for a perovskite-based solar cell device, along with the kinetic curves derived from FemtoFit software by fitting selected wavelengths of interest together.

6. Conclusion

An optimized software toolbox was developed to treat femtosecond transient absorption data, specifically designed for fast photoinduced processes, such as those observed with indoline derivatives in DSSCs. The software addresses challenges related to group velocity dispersion (GVD) correction, incorporating mathematical models such as the Sellmeier and exponential equations. These models, along with an exponential function convoluted with a GVD-modified Gaussian, enable accurate data processing. The Python-based program is tailored to handle these complexities, ensuring precise analysis of transient absorption data.

To illustrate its application, D205 samples in various solvents were analyzed, demonstrating the molecular dynamics processing and the effectiveness of different preprocessing and global fitting steps. The results indicated that the photophysics of D205 in ionic liquids is similar to that observed in organic solvents.

As an example, perovskite-based photovoltaic cells were briefly analyzed under varying pump and probe conditions. The 720 nm pump with visible probe revealed spectral features that were analyzed using the fitting models. This example shows the versatility of the software in handling complex data, highlighting how the same approach can be applied across different systems.

In summary, the software provides a powerful and flexible tool for analyzing femtosecond transient absorption data across a wide range of systems, from simple dye solutions to more complex solar cell devices. Its ability to address challenges such as GVD correction and handle complex dynamic processes makes it invaluable for studying a variety of photophysical phenomena. By offering precise and adaptable fitting capabilities, it enables a thorough investigation of molecular dynamics and excited state behaviors, ultimately contributing to a deeper understanding of both fundamental processes and practical applications in areas such as solar energy research.

7. Chapter 2 References

[1] B. O'Regan and M. Grätzel, "A low-cost, high-efficiency solar cell based on dye-sensitized colloidal TiO2 films," *Nature*, vol. 353, no. 6346, pp. 737–740, Oct. 1991, doi: 10.1038/353737a0.

[2] E. Biyik *et al.*, "A key review of building integrated photovoltaic (BIPV) systems," *Engineering Science and Technology, an International Journal*, vol. 20, no. 3. Elsevier, pp. 833–858, Jun. 01, 2017, doi: 10.1016/j.jestch.2017.01.009.

[3] E. Franklin, V. Everett, A. Blakers, and K. Weber, "Sliver solar cells: High-efficiency, low-cost PV technology," *Adv. Optoelectron.*, vol. 2007, no. 1, p. 035383, Jan. 2007, doi: 10.1155/2007/35383.

[4] M. Biancardo *et al.*, "Characterization of microspherical semi-transparent solar cells and modules," *Sol. Energy*, vol. 81, no. 6, pp. 711–716, Jun. 2007, doi: 10.1016/j.solener.2006.10.009.

[5] K. Lee *et al.*, "Neutral-Colored Transparent Crystalline Silicon Photovoltaics," *Joule*, vol. 4, no. 1, pp. 235–246, Jan. 2020, doi: 10.1016/j.joule.2019.11.008.

[6] P. D. Sekaran and R. Marimuthu, "An Extensive Analysis of Dye-Sensitized Solar Cell (DSSC)," *Brazilian J. Phys.*, vol. 54, no. 1, pp. 1–10, Feb. 2024, doi: 10.1007/s13538-023-01375-w.

[7] S. Garcia Mayo, "Dye-Sensitized Solar Cells: the future of consumer electronics?," 2021, Accessed: Nov. 28, 2024. [Online]. Available: https://urn.kb.se/resolve?urn=urn:nbn:se:hig:diva-36993.

[8] Z. Yin *et al.*, "Graphene-Based materials for solar cell applications," *Advanced Energy Materials*, vol. 4, no. 1. John Wiley & Sons, Ltd, p. 1300574, Jan. 01, 2014, doi: 10.1002/aenm.201300574.

[9] Q. Huaulmé *et al.*, "Photochromic dye-sensitized solar cells with light-driven adjustable optical transmission and power conversion efficiency," *Nat. Energy*, vol. 5, no. 6, pp. 468–477, Jun. 2020, doi: 10.1038/s41560-020-0624-7.

[10] D. Joly *et al.*, "Metal-free organic sensitizers with narrow absorption in the visible for solar cells exceeding 10% efficiency," *Energy Environ. Sci.*, vol. 8, no. 7, pp. 2010–2018, Jul. 2015, doi: 10.1039/c5ee00444f.

[11] F. Grifoni *et al.*, “Toward Sustainable, Colorless, and Transparent Photovoltaics: State of the Art and Perspectives for the Development of Selective Near-Infrared Dye-Sensitized Solar Cells,” *Advanced Energy Materials*, vol. 11, no. 43. John Wiley & Sons, Ltd, p. 2101598, Nov. 01, 2021, doi: 10.1002/aenm.202101598.

[12] Y. Smortsova *et al.*, “Solvatochromic effects on a class of indoline derivatives organic photosensitizers: About the influence of hydrogen-bond acceptor and donor abilities parameters,” *J. Mol. Liq.*, vol. 245, pp. 76–84, Nov. 2017, doi: 10.1016/j.molliq.2017.06.052.

[13] N. Maity, P. Piatkowski, K. Polok, F. A. Miannay, and A. Idrissi, “Effect of the Mixture Composition of BmimBF4-Acetonitrile on the Excited-State Relaxation Dynamics of a Solar-Cell Dye D149: An Ultrafast Transient Absorption Study,” *J. Phys. Chem. C*, vol. 125, no. 32, pp. 17841–17852, Aug. 2021, doi: 10.1021/acs.jpcc.1c05008.

[14] D. Kuang, S. Uchida, R. Humphry-Baker, S. M. Zakeeruddin, and M. Grätzel, “Organic dye-sensitized ionic liquid based solar cells: Remarkable enhancement in performance through molecular design of indoline sensitizers,” *Angew. Chemie - Int. Ed.*, vol. 47, no. 10, pp. 1923–1927, Feb. 2008, doi: 10.1002/anie.200705225.

[15] Y. Smortsova, “Dye sensitized solar cells effciency improvement: optimization of the electrolyte using ionic liquids/molecular solvents mixture and study of the photodynamic properties of organic indolinic derivative dyes,” Universit_e de Lille, 2018.

[16] N. Maity, “Characterization of the polarity, reorientation dynamics and photophysics of indoline based solar cell dyes in ionic liquid-molecular solvent mixtures: steadystate UV-visible, EPR, time resolved fluorescence, femtosecond transient absorption and optical K,” Université de Lille, 2022.

[17] J. B. Prieto, F. L. Arbeloa, V. M. Martínez, T. A. López, and I. L. Arbeloa, “Photophysical properties of the pyrromethene 597 dye: Solvent effect,” *J. Phys. Chem. A*, vol. 108, no. 26, pp. 5503–5508, Jul. 2004, doi: 10.1021/JP0373898/ASSET/IMAGES/LARGE/JP0373898F00007.JPEG.

[18] P. W. Lohse *et al.*, “Ultrafast photoinduced relaxation dynamics of the indoline dye D149 in organic solvents,” *Phys. Chem. Chem. Phys.*, vol. 13, no. 43, pp.

19632–19640, Oct. 2011, doi: 10.1039/C1CP22429H.

[19] I. Benesperi, H. Michaels, and M. Freitag, "The researcher's guide to solid-state dye-sensitized solar cells," *Journal of Materials Chemistry C*, vol. 6, no. 44. Royal Society of Chemistry, pp. 11903–11942, Nov. 15, 2018, doi: 10.1039/c8tc03542c.

[20] S. V. Raksha, V. I. Kondrashin, E. A. Pecherskaya, and K. O. Nikolaev, "Functional Materials for Dye-sensitized Solar Cells," vol. 7, no. 4, p. 4062, 2015, Accessed: Jan. 31, 2023. [Online]. Available: https://essuir.sumdu.edu.ua/handle/123456789/44480.

[21] H. Iftikhar, G. G. Sonai, S. G. Hashmi, A. F. Nogueira, and P. D. Lund, "Progress on electrolytes development in dye-sensitized solar cells," *Materials*, vol. 12, no. 12. Multidisciplinary Digital Publishing Institute, p. 1998, Jun. 21, 2019, doi: 10.3390/ma12121998.

[22] M. K. Nazeeruddin *et al.*, "Combined experimental and DFT-TDDFT computational study of photoelectrochemical cell ruthenium sensitizers," in *Renewable Energy: Four Volume Set*, vol. 2–4, no. 48, American Chemical Society, 2018, pp. 227–251.

[23] P. Wang *et al.*, "Stable new sensitizer with improved light harvesting for nanocrystalline dye-sensitized solar cells," *Adv. Mater.*, vol. 16, no. 20, pp. 1806–1811, Oct. 2004, doi: 10.1002/adma.200400039.

[24] A. Yella *et al.*, "Porphyrin-sensitized solar cells with cobalt (II/III)-based redox electrolyte exceed 12 percent efficiency," *Science (80-.).*, vol. 334, no. 6056, pp. 629–634, Nov. 2011, doi: 10.1126/science.1209688.

[25] M. K. Nazeeruddin *et al.*, "Conversion of Light to Electricity by zyx cis-XzBis(zyxwv 2,2'-bipyridyl-4,4'-dicarboxylate)ruthenium(11) Charge-Transfer Sensitizers (X zyxw = C1-, Br-, I-, CN-, and SCN-) on Nanocrystalline Ti02 Electrodes," *J. Am. Chem. SOC. zyxw*, vol. 115, no. Ii, pp. 6382–6390, 1993.

[26] N. Papageorgiou *et al.*, "The Performance and Stability of Ambient Temperature Molten Salts for Solar Cell Applications," *J. Electrochem. Soc.*, vol. 143, no. 10, pp. 3099–3108, Oct. 1996, doi: 10.1149/1.1837171.

[27] L. A. Santa-Cruz *et al.*, "Effect of heterocyclic nitrogen ionic liquid additives on

the rate of backreaction in DSSCS: An electrochemical characterization," *J. Sci. Adv. Mater. Devices*, vol. 6, no. 3, pp. 483–487, Sep. 2021, doi: 10.1016/J.JSAMD.2021.05.007.

[28] D. Kuang, S. Uchida, R. Humphry-Baker, S. M. Zakeeruddin, and M. Grätzel, "Organic Dye-Sensitized Ionic Liquid Based Solar Cells: Remarkable Enhancement in Performance through Molecular Design of Indoline Sensitizers," *Angew. Chemie*, vol. 120, no. 10, pp. 1949–1953, 2008, doi: 10.1002/ange.200705225.

[29] J. R. Reimers and L. E. Hall, "The solvation of acetonitrile," *J. Am. Chem. Soc.*, vol. 121, no. 15, pp. 3730–3744, 1999, doi: 10.1021/ja983878n.

[30] O. Quinet, B. Champagne, and V. Rodriguez, "Experimental and theoretical investigation of the Raman and hyper-Raman spectra of acetonitrile and its derivatives," *J. Chem. Phys.*, vol. 124, no. 24, p. 244312, 2006, doi: 10.1063/1.2208350.

[31] K. L. Rowlen1 and J. M. Harris, "Raman Spectroscopic Study of Solvation Structure in Acetonitrile/Water Mixtures," *Anal. Chem.*, vol. 63, no. 10, pp. 964–969, 1991, doi: 10.1021/ac00010a006.

[32] A. M. Brouwer, "Standards for photoluminescence quantum yield measurements in solution (IUPAC technical report)," *Pure Appl. Chem.*, vol. 83, no. 12, pp. 2213–2228, Aug. 2011, doi: 10.1351/PAC-REP-10-09-31/MACHINEREADABLECITATION/RIS.

[33] M. Fakis, P. Hrobárik, E. Stathatos, V. Giannetas, and P. Persephonis, "A time resolved fluorescence and quantum chemical study of the solar cell sensitizer D149," *Dye. Pigment.*, vol. 96, no. 1, pp. 304–312, Jan. 2013, doi: 10.1016/J.DYEPIG.2012.07.025.

[34] J. C. Del Valle and J. Catalán, "Kasha's rule: A reappraisal," *Phys. Chem. Chem. Phys.*, vol. 21, no. 19, pp. 10061–10069, 2019, doi: 10.1039/c9cp00739c.

[35] Y. Zhang, Y. Duan, and T. Wang, "Excited-state hydrogen-bonding dynamics of camphorsulfonic acid doped polyaniline: A theoretical study," *Phys. Chem. Chem. Phys.*, vol. 16, no. 47, pp. 26261–26265, Nov. 2014, doi: 10.1039/c4cp04267k.

[36] N. Sharma, S. K. Jain, and R. C. Rastogi, “Excited-state dipole moments of indoles using solvatochromic shift methods: An experimental and theoretical study,” *Bull. Chem. Soc. Jpn.*, vol. 76, no. 9, pp. 1741–1746, 2003, doi: 10.1246/bcsj.76.1741.

[37] T. Le Bahers, T. Pauporté, G. Scalmani, C. Adamo, and I. Ciofini, “A TD-DFT investigation of ground and excited state properties in indoline dyes used for dye-sensitized solar cells,” *Phys. Chem. Chem. Phys.*, vol. 11, no. 47, pp. 11276–11284, 2009, doi: 10.1039/b914626a.

[38] C. Wohlfahrt, “Static Dielectric Constants of Pure Liquids and Binary Mixtures,” in *Landolt-Börnstein – Group IV Physical Chemistry*, O. Madelung, Ed. 2002.

[39] C. Albrecht, “Joseph R. Lakowicz: Principles of fluorescence spectroscopy, 3rd Edition,” *Anal. Bioanal. Chem. 2007 3905*, vol. 390, no. 5, pp. 1223–1224, Jan. 2008, doi: 10.1007/S00216-007-1822-X.

[40] A. M. El-Zohry and B. Zietz, “Concentration and solvent effects on the excited state dynamics of the solar cell dye D149: The special role of protons,” *J. Phys. Chem. C*, vol. 117, no. 13, pp. 6544–6553, Apr. 2013, doi: 10.1021/jp400782g.

[41] A. M. El-Zohry and B. Zietz, “Electron Dynamics in Dye-Sensitized Solar Cells Influenced by Dye-Electrolyte Complexation,” *J. Phys. Chem. C*, vol. 124, no. 30, pp. 16300–16307, Jul. 2020, doi: 10.1021/acs.jpcc.0c03436.

[42] N. Boens *et al.*, “Fluorescence lifetime standards for time and frequency domain fluorescence spectroscopy,” *Anal. Chem.*, vol. 79, no. 5, pp. 2137–2149, Mar. 2007, doi: 10.1021/ac062160k.

[43] PicoQuant, *FluoFit: User’s Manual and Technical Data*, Version 4. .

[44] A. M. El-Zohry, D. Roca-Sanjuán, and B. Zietz, “Ultrafast twisting of the indoline donor unit utilized in solar cell dyes: Experimental and theoretical studies,” *J. Phys. Chem. C*, vol. 119, no. 5, pp. 2249–2259, Feb. 2015, doi: 10.1021/JP505649S/SUPPL_FILE/JP505649S_SI_001.PDF.

[45] A. El-Zohry, A. Orthaber, and B. Zietz, “Isomerization and aggregation of the solar cell dye D149,” *J. Phys. Chem. C*, vol. 116, no. 50, pp. 26144–26153, Dec. 2012, doi: 10.1021/jp306636w.

[46] A. M. El-Zohry, S. Agrawal, F. De Angelis, M. Pastore, and B. Zietz, “Critical

Role of Protons for Emission Quenching of Indoline Dyes in Solution and on Semiconductor Surfaces," *J. Phys. Chem. C*, vol. 124, no. 39, pp. 21346–21356, Oct. 2020, doi: 10.1021/acs.jpcc.0c07099.

[47] J. Sobuš, J. Karolczak, D. Komar, J. A. Anta, and M. Ziółek, "Transient states and the role of excited state self-quenching of indoline dyes in complete dye-sensitized solar cells," *Dye. Pigment.*, vol. 113, pp. 692–701, Feb. 2015, doi: 10.1016/j.dyepig.2014.10.008.

[48] R. Berera, R. van Grondelle, and J. T. M. Kennis, "Ultrafast transient absorption spectroscopy: Principles and application to photosynthetic systems," *Photosynthesis Research*, vol. 101, no. 2–3. Springer, pp. 105–118, Sep. 04, 2009, doi: 10.1007/s11120-009-9454-y.

[49] A. Maciejewski *et al.*, "Transient absorption experimental set-up with femtosecond time resolution. Femto- and picosecond study of DCM molecule in cyclohexane and methanol solution," in *Journal of Molecular Structure*, Nov. 2000, vol. 555, no. 1–3, pp. 1–13, doi: 10.1016/S0022-2860(00)00582-2.

[50] J. E. Ikpesu, S. E. Iyuke, M. Daramola, and A. O. Okewale, "Synthesis of improved dye-sensitized solar cell for renewable energy power generation," *Solar Energy*, vol. 206. Pergamon, pp. 918–934, Aug. 01, 2020, doi: 10.1016/j.solener.2020.05.002.

[51] N. I. A. Shukor *et al.*, "A Green Approach to Natural Dyes in Dye-Sensitized Solar Cells," *Sensors (Basel).*, vol. 23, no. 20, p. 8412, Oct. 2023, doi: 10.3390/s23208412.

[52] D. Javiya *et al.*, "Studies and comparison of natural dye-sensitized solar cells and thin-film solar cells," in *Materials Today: Proceedings*, Jan. 2023, vol. 73, pp. 545–549, doi: 10.1016/j.matpr.2022.10.222.

[53] C. L. Lee, W. H. Lee, and C. H. Yang, "High efficiency of dye-sensitized solar cells based on ruthenium and metal-free dyes," *Int. J. Photoenergy*, vol. 2013, no. 1, p. 250397, Jan. 2013, doi: 10.1155/2013/250397.

[54] S. Rahman *et al.*, "Research on dye sensitized solar cells: recent advancement toward the various constituents of dye sensitized solar cells for efficiency enhancement and future prospects," *RSC Advances*, vol. 13, no. 28. Royal Society

of Chemistry, pp. 19508–19529, Jun. 28, 2023, doi: 10.1039/d3ra00903c.

[55] B. S. Arslan *et al.*, “Optimization of fabrication parameters for efficient dye-sensitized solar cells based on dyes containing benzothiadiazole, indoline, and their co-sensitization,” *Electrochim. Acta*, vol. 458, p. 142523, Aug. 2023, doi: 10.1016/j.electacta.2023.142523.

[56] L. J. G. W. van Wilderen, C. N. Lincoln, and J. J. van Thor, “Modelling Multi-Pulse Population Dynamics from Ultrafast Spectroscopy,” *PLoS One*, vol. 6, no. 3, p. e17373, 2011, doi: 10.1371/JOURNAL.PONE.0017373.

[57] G. Nass Kovacs *et al.*, “Three-dimensional view of ultrafast dynamics in photoexcited bacteriorhodopsin,” *Nat. Commun. 2019 101*, vol. 10, no. 1, pp. 1–17, Jul. 2019, doi: 10.1038/s41467-019-10758-0.

[58] T. D. Green and K. L. Knappenberger, “Relaxation dynamics of Au25L18 nanoclusters studied by femtosecond time-resolved near infrared transient absorption spectroscopy,” *Nanoscale*, vol. 4, no. 14, pp. 4111–4118, Jun. 2012, doi: 10.1039/c2nr31080e.

[59] M. Fakis, E. Stathatos, G. Tsigaridas, V. Giannetas, and P. Persephonis, “Femtosecond decay and electron transfer dynamics of the organic sensitizer d149 and photovoltaic performance in quasi-solid-state dye-sensitized solar cells,” *J. Phys. Chem. C*, vol. 115, no. 27, pp. 13429–13437, Jul. 2011, doi: 10.1021/jp201143n.

[60] I. H. M. Van Stokkum, D. S. Larsen, and R. Van Grondelle, “Global and target analysis of time-resolved spectra,” *Biochimica et Biophysica Acta - Bioenergetics*, vol. 1657, no. 2–3. Elsevier, pp. 82–104, Jul. 09, 2004, doi: 10.1016/j.bbabio.2004.04.011.

[61] M. Ziólek, M. Lorenc, and R. Naskrecki, “Determination of the temporal response function in femtosecond pump-probe systems,” *Appl. Phys. B Lasers Opt.*, vol. 72, no. 7, pp. 843–847, 2001, doi: 10.1007/S003400100587/METRICS.

[62] J. S. Beckwith, C. A. Rumble, and E. Vauthey, “Data analysis in transient electronic spectroscopy–an experimentalist’s view,” *International Reviews in Physical Chemistry*, vol. 39, no. 2. Taylor & Francis, pp. 135–216, Apr. 02, 2020, doi: 10.1080/0144235X.2020.1757942.

[63] S. Ito *et al.*, “High-conversion-efficiency organic dye-sensitized solar cells with a novel indoline dye,” *Chem. Commun.*, no. 41, pp. 5194–5196, 2008, doi: 10.1039/b809093a.

[64] E. Rohwer *et al.*, “Ultrafast Photodynamics of the Indoline Dye D149 Adsorbed to Porous ZnO in Dye-Sensitized Solar Cells,” *ChemPhysChem*, vol. 14, no. 1, pp. 132–139, Jan. 2013, doi: 10.1002/CPHC.201200715.

[65] V. Novelli, N. Barbero, C. Barolo, G. Viscardi, M. Sliwa, and F. Sauvage, “Electrolyte containing lithium cation in squaraine-sensitized solar cells: Interactions and consequences for performance and charge transfer dynamics,” *Phys. Chem. Chem. Phys.*, vol. 19, no. 40, pp. 27670–27681, Oct. 2017, doi: 10.1039/c7cp04340f.

[66] S. Singh, Z. H. Khan, M. B. Khan, P. Kumar, and P. Kumar, “Quantum dots-sensitized solar cells: a review on strategic developments,” *Bulletin of Materials Science*, vol. 45, no. 2. Springer, pp. 1–13, Jun. 01, 2022, doi: 10.1007/s12034-022-02662-z.

[67] F. Matteocci *et al.*, “Wide bandgap halide perovskite absorbers for semi-transparent photovoltaics: From theoretical design to modules,” *Nano Energy*, vol. 101, p. 107560, Oct. 2022, doi: 10.1016/j.nanoen.2022.107560.

[68] W. Naim *et al.*, “Transparent and Colorless Dye-Sensitized Solar Cells Exceeding 75% Average Visible Transmittance,” vol. 15, p. 59, 2023, doi: 10.1021/jacsau.1c00045.

[69] A. Ebenezer Anitha and M. Dotter, “A Review on Liquid Electrolyte Stability Issues for Commercialization of Dye-Sensitized Solar Cells (DSSC),” *Energies*, vol. 16, no. 13. Multidisciplinary Digital Publishing Institute, p. 5129, Jul. 03, 2023, doi: 10.3390/en16135129.

[70] A. Agrawal, S. A. Siddiqui, A. Soni, and G. D. Sharma, “Advancements, frontiers and analysis of metal oxide semiconductor, dye, electrolyte and counter electrode of dye sensitized solar cell,” *Solar Energy*, vol. 233. Pergamon, pp. 378–407, Feb. 01, 2022, doi: 10.1016/j.solener.2022.01.027.

[71] B. K. Korir, J. K. Kibet, and S. M. Ngari, “A review on the current status of dye-sensitized solar cells: Toward sustainable energy,” *Energy Science and*

Engineering, vol. 12, no. 8. John Wiley & Sons, Ltd, pp. 3188–3226, Aug. 01, 2024, doi: 10.1002/ese3.1815.

[72] M. Grätzel, “Dye-sensitized solar cells,” *J. Photochem. Photobiol. C Photochem. Rev.*, vol. 4, no. 2, pp. 145–153, Oct. 2003, doi: 10.1016/S1389-5567(03)00026-1.

[73] J. Wu *et al.*, “Counter electrodes in dye-sensitized solar cells,” *Chemical Society Reviews*, vol. 46, no. 19. Royal Society of Chemistry, pp. 5975–6023, Oct. 02, 2017, doi: 10.1039/c6cs00752j.

[74] G. Richhariya, A. Kumar, A. K. Shukla, K. N. Shukla, and B. C. Meikap, “Effect of Different Counter Electrodes on Power Conversion Efficiency of DSSCs,” *Journal of Electronic Materials*, vol. 52, no. 1. Springer, pp. 60–71, Jan. 01, 2023, doi: 10.1007/s11664-022-09973-1.

[75] N. A. Karim, U. Mehmood, H. F. Zahid, and T. Asif, “Nanostructured photoanode and counter electrode materials for efficient Dye-Sensitized Solar Cells (DSSCs),” *Solar Energy*, vol. 185. Pergamon, pp. 165–188, Jun. 01, 2019, doi: 10.1016/j.solener.2019.04.057.

[76] C. I. Oprea *et al.*, “Role of energy level alignment in solar cells sensitized with a metal-free organic dye: A combined experimental and theoretical approach,” *Phys. Status Solidi Appl. Mater. Sci.*, vol. 208, no. 10, pp. 2467–2477, 2011, doi: 10.1002/pssa.201127083.

[77] J. Lungu *et al.*, “Heterocyclic azodyes as pigments for dye sensitized solar cells - A combined experimental and theoretical study,” *J. Optoelectron. Adv. Mater.*, vol. 12, no. 9, pp. 1969–1975, 2010.

[78] L. Zhang and J. M. Cole, “Dye aggregation in dye-sensitized solar cells,” *J. Mater. Chem. A*, vol. 5, no. 37, pp. 19541–19559, Sep. 2017, doi: 10.1039/C7TA05632J.

[79] F. Xu, T. T. Testoff, L. Wang, and X. Zhou, “Cause, Regulation and Utilization of Dye Aggregation in Dye-Sensitized Solar Cells,” *Mol. 2020, Vol. 25, Page 4478*, vol. 25, no. 19, p. 4478, Sep. 2020, doi: 10.3390/MOLECULES25194478.

[80] A. F. Buene, D. M. Almenningen, A. Hagfeldt, O. R. Gautun, and B. H. Hoff, “First Report of Chenodeoxycholic Acid–Substituted Dyes Improving the Dye Monolayer Quality in Dye-Sensitized Solar Cells,” *Sol. RRL*, vol. 4, no. 4, p.

1900569, Apr. 2020, doi: 10.1002/solr.201900569.

[81] X. Jiang, T. Marinado, E. Gabrielsson, D. P. Hagberg, L. Sun, and A. Hagfeldt, "Structural Modification of organic dyes for efficient coadsorbent-free dye-sensitized solar cells," *J. Phys. Chem. C*, vol. 114, no. 6, pp. 2799–2805, Feb. 2010, doi: 10.1021/JP908552T/SUPPL_FILE/JP908552T_SI_005.TIF.

[82] P. Boyce, N. Eklund, S. Mangum, C. Saalfield, and L. Tang, "Minimum acceptable transmittance of glazing," *http://dx.doi.org/10.1177/14771535950270030201*, vol. 27, no. 3, pp. 145–152, Sep. 1995, doi: 10.1177/14771535950270030201.

[83] N. Kutlu, "Investigation of electrical values of low-efficiency dye-sensitized solar cells (DSSCs)," *Energy*, vol. 199, p. 117222, May 2020, doi: 10.1016/j.energy.2020.117222.

[84] S. Sarker, H. W. Seo, and D. M. Kim, "Calculating current density-voltage curves of dye-sensitized solar cells: A straight-forward approach," *J. Power Sources*, vol. 248, pp. 739–744, Feb. 2014, doi: 10.1016/j.jpowsour.2013.09.101.

[85] M. E. Ragoussi, M. Ince, and T. Torres, "Recent Advances in Phthalocyanine-Based Sensitizers for Dye-Sensitized Solar Cells," *European J. Org. Chem.*, vol. 2013, no. 29, pp. 6475–6489, Oct. 2013, doi: 10.1002/EJOC.201301009.

[86] M.-E. Ragoussi *et al.*, "Carboxyethynyl Anchoring Ligands: A Means to Improving the Efficiency of Phthalocyanine-Sensitized Solar Cells," *Angew. Chemie*, vol. 124, no. 18, pp. 4451–4454, Apr. 2012, doi: 10.1002/ANGE.201108963.

[87] M. Kimura *et al.*, "Molecular Design Rule of Phthalocyanine Dyes for Highly Efficient Near-IR Performance in Dye-Sensitized Solar Cells," *Chem. – A Eur. J.*, vol. 19, no. 23, pp. 7496–7502, Jun. 2013, doi: 10.1002/CHEM.201300716.

[88] M. Ince *et al.*, "Peripherally and axially carboxylic acid substituted subphthalocyanines for dye-sensitized solar cells," *Chem. - A Eur. J.*, vol. 20, no. 7, pp. 2016–2021, Feb. 2014, doi: 10.1002/CHEM.201303639.

[89] B. Verreet *et al.*, "A 4% Efficient Organic Solar Cell Using a Fluorinated Fused Subphthalocyanine Dimer as an Electron Acceptor," *Adv. Energy Mater.*, vol. 1, no. 4, pp. 565–568, Jul. 2011, doi: 10.1002/AENM.201100137.

[90] H. Gotfredsen *et al.*, “Donor−Acceptor-Functionalized Subphthalocyanines for Dye-Sensitized Solar Cells,” *ChemPhotoChem*, vol. 2, no. 11, pp. 976–985, Nov. 2018, doi: 10.1002/CPTC.201800135.

[91] W. NAIM, “A novel approach of selective near-IR dye-sensitized solar cells as colorless and transparent photovoltaics : aesthetic evaluation and performance optimization,” Université de Picardie Jules Verne, 2022.

Chapter 3: Fabrication and analysis of Dye-Sensitized Solar Cells (DSSC): SubPc and VG20-TBPF dyes

This chapter reports on the study of DSSCs using SubPc and VG20-TBPF dyes. The investigation focused on the fabrication of the cells, including the preparation of dye solutions, immersion of the photoanodes, and performance testing. The performance of the DSSCs was characterized using steady-state UV-visible absorption, emission spectroscopy, transient absorption spectroscopy (TAS), as well as impedance spectroscopy (IMVS/IMPS) to evaluate charge transport and recombination dynamics. For the VG20-TBPF cells, CDCA was added to the dye solution in varying concentrations to reduce dye aggregation. The best performance was observed for a 1:300 ratio of VG20-TBPF to CDCA, achieving a power conversion efficiency of 2.18%. The addition of CDCA enhanced the uniformity of the dye distribution on the TiO_2 *surface, improving electron injection and reducing recombination. Additionally, a new method of fabricating the photoanodes was explored, focusing on reducing the thickness of the semiconductor layer. For the SubPc dyes, the S32 dye dissolved in THF showed the best performance, with a PCE of 1.69%. This efficiency was achieved despite the challenges posed by the different solvent environments. The study demonstrated that the SubPc dyes exhibited unique behaviors related to their solubility and molecular structure, with the S32 dye showing promising potential for DSSC applications.*

1. Introduction

A dye-sensitized solar cell (DSSC) is a molecular device that works through electrochemical processes and consists of two main electrodes - the photo-anode and the counter electrode - and the electrolyte containing a redox mediator. At the heart of this device, there is the dye attached to TiO_2 anatase nanocrystals. The dye's performance as a sensitizer is influenced by its light-harvesting ability, aesthetic properties due to its absorbance profile, and the alignment between LUMO and HOMO energy levels concerning TiO_2 and redox couple conduction bands. Depending on the structure of the dye and the potential for molecular tuning, DSSCs can achieve different levels of transparency and color, which makes them an attractive technology for efficient energy conversion with visual customization due to their wavelength selectivity.

A schematic of a DSSC is shown in Figure 27. The photoanode acts as a base for anchoring the dye and transporting electrons. It consists of a glass slide with transparent conducting oxide (TCO) film, usually fluorine-doped tin oxide (FTO), covered by titanium dioxide (TiO_2). The anatase phase of TiO_2 is used due to its good electronic properties and band gap (~3.2 eV) favorable for electron injection, as well as its convenient high electronic mobility. The TiO_2 particles form a mesoporous structure with a high surface area available for dye adsorption, which is essential for efficient light absorption. In addition, this nanostructure allows for rapid electron transport through itself, reducing recombination rates and increasing the electron injection efficiency.

The dye molecule in DSSCs is critical for light absorption, which boosts the overall photoelectric conversion process. When absorbing photons, the dye's electrons are excited from HOMO to LUMO. Ideally, the dye's LUMO level should be at least 0.2 eV higher in energy than the conduction band of TiO_2, allowing for effective electron injection. On the other hand, the HOMO level must align well with the redox potential of the electrolyte for efficient regeneration of the dye. Different dyes are designed to optimize these energy alignments, usually adapted for broad-spectrum absorption, which increases the light-gathering capacity. Consequently, both the kinetics of electron injection and dye regeneration will be affected, which represents a challenge in optimizing the dyes and their interaction with the system. Metal-based dyes, such as ruthenium (Ru)-based compounds, have historically been the most widely used due to their high stability and efficiency. These dyes are effective at absorbing light and transferring electrons, characteristics that made them popular in earlier studies [65]. However, due to its rarity, the high cost of ruthenium and environmental concerns regarding its toxicity have motivated the search for alternatives. As a result, options such as metal-free organic dyes, sensitizers based on quantum dots (QDs) [66], and perovskites [67] have been explored [6]. In addition to offering greater sustainability, organic dyes allow for molecular customization, with adjustments to their absorption properties and affinity with the semiconductor [11], [68]. Despite this, they still face challenges in terms of stability and efficiency when playing the role of sensitizer, which makes research into new organic dyes essential to achieve a better balance between cost, efficiency, and sustainability in DSSCs.

In DSSCs, the electrolyte is a core component. Usually, it contains the couple I^-/I^{3-} as the redox mediator, which acts as transporting changes between the photoanode and the counter electrode. The redox couple is responsible for regenerating the oxidized dye, setting up an electrochemical cycle within the cell. The electrolyte's properties, such as ionic conductivity, viscosity, and stability, are optimized to minimize diffusion limitations and avoid recombination processes, which can harm efficiency [69], [70]. The low viscosity of traditional liquid electrolytes, typically based on organic solvents like acetonitrile, enables fast ion diffusion and high energy conversion efficiencies. However, these electrolytes have stability issues such as high volatility and leaking which can corrode other components of the cell [65], [71]. Aiming to handle this stability question, investigations using ionic liquids and solid and quasi-solid-state electrolytes have been done. Ionic liquids, such as imidazolium and guanidinium salts, present lower volatility and higher thermal stability than traditional organic solvents, enduring high temperatures without evaporating. However, they still present challenges in terms of cost, which may limit their viability for large-scale use [21], [69], [72].

The counter electrode, usually made up of FTO glass coated with a thin layer of platinum, acts as a catalyst for the reduction of the couple I^-/I^{3-}. Platinum is commonly used due to its great catalytic properties, stability and ability to facilitate rapid electron transfer [73]. However, in order to reduce costs and improve sustainability, alternative materials are being investigated, such as carbon-based catalysts, conductive polymers and other metallic compounds [74]. The efficiency of the counter electrode has an impact on the cell's internal resistance and overall charge collection, and is carefully designed to balance electronic conductivity with catalytic activity in order to improve the device's performance [75].

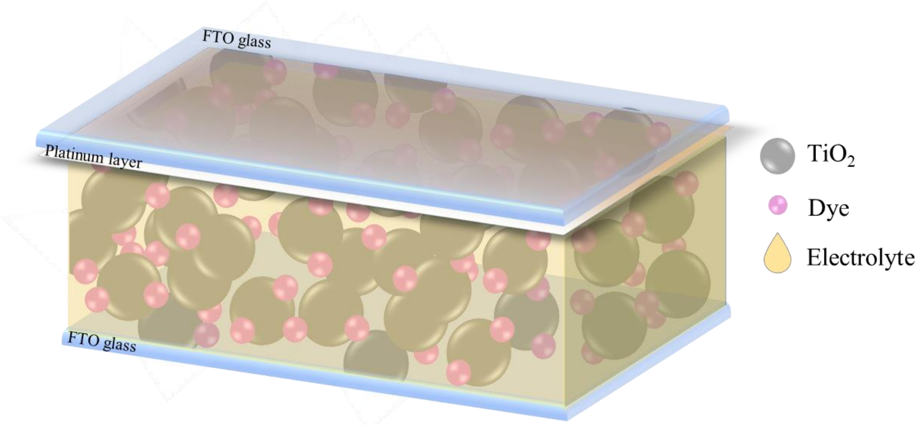

Figure 27. Schematic representation of a dye-sensitized solar cell (DSSC), illustrating the primary components: the FTO (fluorine-doped tin oxide) glasses, the platinum layer, the mesoporous semiconductor layer (TiO_2), the dye-sensitizer, and the electrolyte.

1.1. DSSCs Working Principle

The operating process of DSSCs, which convert light into electricity through photochemical and electrochemical reactions, is associated with the ability of the sensitizing dye molecules to capture light, inject electrons into the semiconductor, and regenerate efficiently through interactions with the electrolyte. The cell's efficiency depends on each stage of this process, starting with the sunlight excitation of the sensitizing dye adsorbed on the semiconductor layer. A schematic illustrating the processes taking place inside the cell is shown in Figure 28. Energy photons hν are absorbed by the molecules, leading to electronic transitions from the ground state (D) to the excited state (D*), as described by reaction R1. Once the dye reaches its excited state, an electron is transferred to the conduction band of the semiconductor, usually TiO_2, starting the electron flow inside the cell. Thus, the dye molecule is oxidized (D^+). This stage of the process is represented in reaction R2 and takes place rapidly, on the picosecond scale. The excited electron then flows through the interconnected layer of TiO_2 and then reaches the transparent substrate of the photoanode, where it will enter the external circuit until it reaches the counter electrode.

The dye molecule, now oxidized, undergoes a regeneration process to return to its ground state of energy and continue absorbing light, giving rise to the entire electronic circuit again. The redox mediator in the electrolyte is responsible for reducing the dye molecule, restoring it to its original D state and forming I_3^- ions. This process is represented by reaction R3 and its time scale is generally between milliseconds and microseconds.

The photoexcited electrons that have been injected into the conduction band of TiO_2, after traveling through the external circuit, reach the counter electrode. The I_3^- ions present in the electrolyte are then reduced. In this way, the electrolyte returns to its stationary state. The counter electrode coated with a catalytic material, such as platinum, facilitates this reduction process, represented in reaction R4. This reaction takes place on a time scale of microseconds [71], [75].

(R1) Photoexcitation of the electron in the dye

$$D/TiO_2 + hv \rightarrow D^*/TiO_2$$

(R2) Electron injection ($k \approx 10^{-12}$ s)

$$D^*/TiO_2 \rightarrow D^+/TiO_2 + e^-/TiO_2$$

(R3) Dye regeneration ($k \approx 10^{-4}$ s)

$$2D^+/TiO_2 + (RE)3I^- \rightarrow 2D/TiO_2 + I_3^-(OX)$$

(R4) Electrolyte regeneration ($k \approx 10^{-6}$ s)

$$(OX)I_3^- + (CE)2e^- \rightarrow (RE)3I^-$$

Some recombination reactions can interfere with the overall efficiency of the device. One of these is regeneration in the oxidized dye D^+ through recombination with electrons present in the conduction band of TiO_2, represented in reaction R5. This process is called twinned recombination since the electron recombines with the same molecular species from which it was initially excited and injected (i.e. the dye molecule). This normally takes place at short distances, at the dye-TiO_2 interface, and just after the electron injection, before the electron reaches the external circuit. This reaction decreases the number of electrons contributing to power generation, wasting the energy of the absorbed photon.

Moreover, the electrons injected into the semiconductor layer can also take part in an oxidation process of the redox mediator present in the electrolyte (reaction R6). This reaction is called non-geminate recombination, since the electron recombines with a species other than the one in which it was initially excited. Such recombination takes place over longer time scales compared to geminate recombination.

(R5) Geminate Recombination (k ≈ 10^{-4} s)

$$e^{-}/TiO_2 + D^{+}/TiO_2 \rightarrow D/TiO_2$$

(R6) Non-geminate recombination (k ≈ 10^{-2} s)

$$e^{-}/TiO_2 + \ (OX)I_3^{-} \rightarrow (RE)3I^{-}$$

Both geminate and non-geminate recombination reactions are undesirable because they reduce the efficiency of the devices, causing energy losses. To optimize the performance of DSSCs, it is necessary to carefully choose the optoelectronic materials so that they facilitate the rapid regeneration of the dye and the electrolyte, minimizing the chances of recombination reactions occurring. In particular, the electron injection and the dye regeneration by the redox pair must be faster than the dye decay and the undesired reaction between the electron injected and the oxidized dye. In addition, the injection of electrons from the excited dye into the conduction band of TiO_2 must occur quickly, typically in femtoseconds, which is significantly faster than the relaxation of the dye, which normally takes nanoseconds [71].

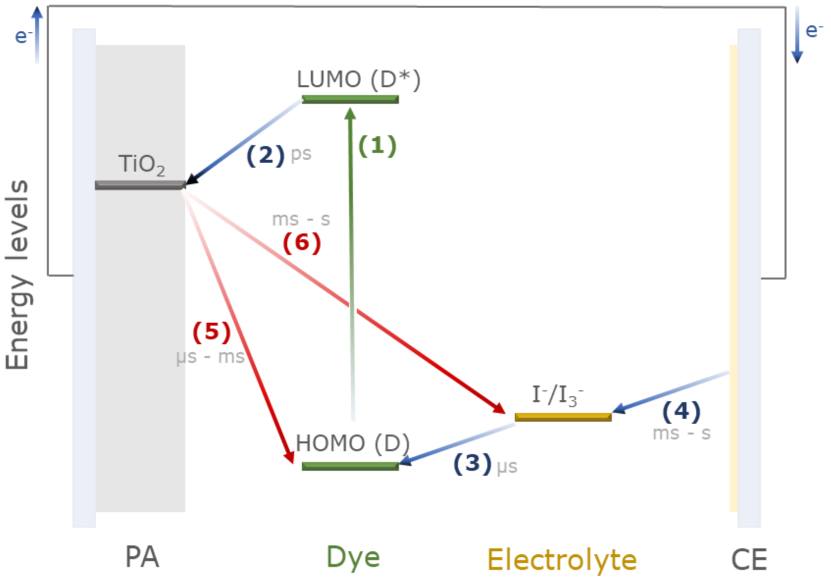

Figure 28. Schematic representation of the working principle of a dye-sensitized solar cell (DSSC), illustrating the main reactions involved in its operation: (1) light absorption by the dye, leading to the excitation of an electron from the HOMO to the LUMO; (2) injection of the excited electron into the conduction band of the semiconductor (TiO_2); (3) regeneration of the oxidized dye through electron donation from the redox electrolyte, which is subsequently reduced at the counter electrode (4); (5) geminate recombination of injected electrons with the oxidized dye; and (6) non-geminate recombination of injected electrons with the redox species in the electrolyte.

1.2. Critical Factors for Efficient DSSCs

1.2.1. Band alignment

One of the main criteria to be considered when choosing a dye to act as a sensitizer for DSSC is the alignment between the energy levels of the dye and the energy levels of the semiconductor and the redox pair present in the electrolyte. A good alignment allows the excited dye to efficiently inject electrons into the semiconductor's conduction band, as well as enabling the regeneration of this oxidized dye by the electrolyte. To ensure electron injection, the dye must have an excited LUMO (Lowest Unoccupied Molecular Orbital) energy level higher than the semiconductor's conduction band. Meanwhile, regeneration of the oxidized dye is only possible if it has a HOMO (Highest Occupied Molecular Orbital) below the redox potential of the electrolyte, allowing the electron to be transferred from the redox pair to the oxidized dye. Once electron injection into the semiconductor occurs, the dye becomes oxidized and therefore needs to be regenerated for the DSSC process cycle to continue. If the LUMO of the dye is not sufficiently above the conduction band of the semiconductor, electron injection becomes slow or completely impeded, leading to lower photocurrent generation. Similarly, a HOMO positioned too close to or higher than the redox potential of the electrolyte blocks the regeneration of the dye, resulting in an accumulation of oxidized dye molecules that cannot restart the process [76].

Although it is essential that the LUMO of the dye is above the conduction band of the semiconductor and that its HOMO is below the redox potential of the electrolyte, excessive misalignment in either direction can negatively affect the performance of DSSCs. When the LUMO is significantly larger than the semiconductor's conduction band, electron injection, although thermodynamically favorable, can suffer kinetic inefficiencies due to reduced electronic coupling between the dye and the semiconductor. In addition, the large energy gap can lead to energy dissipation in the form of heat, reducing the device's overall efficiency. Similarly, a HOMO far below the redox potential of the electrolyte can slow down regeneration kinetics and lead to recombination losses, as the oxidized dye molecules persist for longer periods [77].

When band alignment is not optimized within a reasonable range, energy generation and process restart are directly impacted. Therefore, good alignment between the DSSC components is essential to avoid energy losses and maximize energy conversion efficiency.

1.2.2. Dye Aggregation

Aggregation of dye molecules is another factor that can negatively affect the efficiency of DSSCs. Even at reasonable concentrations, dye molecules can self-associate, forming molecular aggregates. These aggregates disrupt the uniform absorption of light, harm the electron injection and reduce the overall performance of the device. Aggregation affects the efficiency of DSSCs in different ways, depending on the type of aggregate formed, which is usually classified as H-aggregates or J-aggregates. Each type has different optical properties that impact the device's performance.

H-aggregates are formed when the dye molecules align side by side, causing a hypsochromic shift (blue shift) in the absorption band. This shift reduces the range of wavelengths in which the dye can effectively absorb sunlight and can lead to a mismatch between the dye's absorption spectrum and the solar spectrum. As a result, the dye captures less sunlight, resulting in energy losses and reduced electron injection into the semiconductor. In addition, the H-aggregation broadens the absorption band in the visible range, which can cause a coloration on the surface. This coloration is particularly undesirable for applications that require transparency, such as building-integrated photovoltaics (BIPV) or transparent solar cells for windows, where it is essential to keep a neutral appearance. H-aggregation therefore has a negative impact on both the efficiency and aesthetic of DSSCs.

J-aggregates are formed through a head-to-tail alignment of the dye molecules and lead to a bathochromic shift (red shift) in the absorption band. This shift broadens the absorption spectrum in the red region and can also introduce additional absorption peaks in this range. Although this red shift may initially seem beneficial, it can disturb the correspondence between the dye's absorption spectrum and the solar spectrum. This misalignment impairs the charge separation process, reducing the efficiency of electron injection, as happens in the presence of H-aggregates. By affecting the transfer of excited state electrons from the dye to the semiconductor, J-aggregates cause a decrease in photocurrent generation and overall energy conversion efficiency.

Both H and J aggregates negatively interfere with the ideal photoelectronic properties of the sensitizing dye, altering the absorption spectrum and, consequently, the electron injection dynamics. To mitigate these effects, careful molecular engineering and the use of additives to prevent aggregation are required, thus optimizing the efficiency and appearance of DSSCs [68], [78], [79].

To avoid the harmful effects of aggregation, disaggregating agents such as chenodeoxycholic acid (CDCA) are usually added to the dye solutions. CDCA works by spacing the dye molecules more uniformly on the surface of the semiconductor, preventing these molecules from forming aggregates, which helps to keep uniform adsorption on the surface of the semiconductor and optimal light absorption of the dye, promoting the aesthetic transparency of the device. In addition to CDCA, strategies such as co-sensitization and the incorporation of bulky side groups or long chains into the dye molecules can also reduce aggregation tendencies. However, balancing the concentration of CDCA is crucial, since excessive amounts can decrease the dye load in the semiconductor, reducing the cell's light absorption capacity and, consequently, its energy conversion efficiency [80], [81].

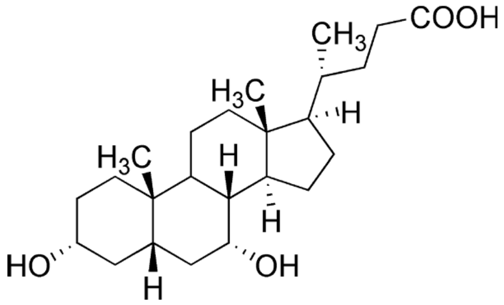

Figure 29: Molecular structure of chenodeoxycholic acid (CDCA) [81]

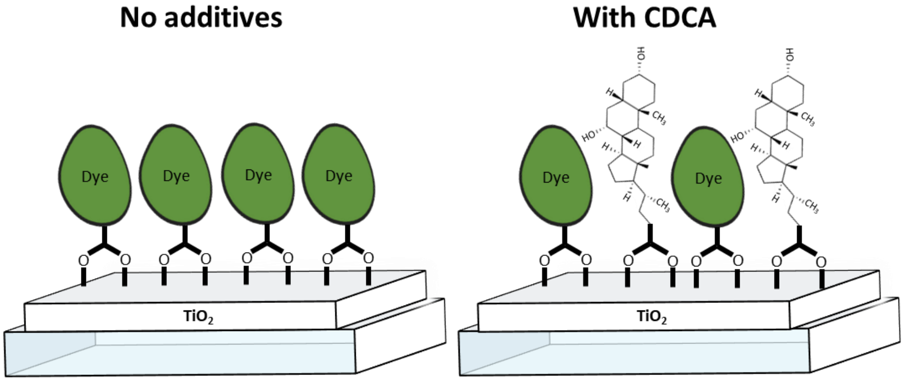

Figure 30. Schematic representation of dye molecule distribution on TiO_2 surfaces: (left) without CDCA and (right) with CDCA, demonstrating molecular spacing.

2. Methodology

The DSSC manufacturing method used was developed at the *Laboratoire de Réactivité et Chimie des Solides* (LRCS) and is detailed in the appendix. In summary, the production process begins with the preparation of the photoanode, the main step being the printing of TiO_2 onto the previously prepared FTO TEC 11 glass substrate. After the heat treatment process, the photoanode is immersed in the dye solutions for 24 hours so that the dye adsorbs onto the semiconductor layer. The counter electrodes have an FTO TEC 7 glass substrate and receive a layer of platinum. After this process, the cell is assembled, where the photoanode and counter electrode are joined by Surlyn bonding. The electrolyte is applied inside the cell through a hole previously drilled in the counter electrode. After being sealed, the cell receives a black metal mask with an opening only in the area of interest (approximately 0.160 cm^2), where all the cell's components are present. Wires are also attached to the devices to enable them to be connected to the solar simulator's external circuitry.

The cell is then ready to have its performance evaluated. In some cases, the efficiency of the cells is measured before and after a period of irradiation that can last from 15 minutes to an hour. This step is carried out in order to observe the photochemical stability of the dyes and the other components of the cell, as well as the possible effects of photoactivation, since in some cases the performance of a DSSC can improve after a brief initial exposure to light, as there is a reorganization or optimization of the interface between the dye, semiconductor and electrolyte. All the DSSCs produced in this study had their performance assessed by the solar simulator and Intensity Modulated Photovoltage/Photocurrent Spectroscopy (IMVS/IMPS) experiments, procedures detailed in the appendix.

To investigate the kinetics of the regeneration and recombination processes present, suitable samples were produced for picosecond transient absorption spectroscopy tests. These samples produced for TAS must be more transparent. To achieve this, no TiO_2 scattering layer is applied as is done in the cells used for electrical characterization. In addition, the counter electrode receives a thinner layer of platinum. The electrolyte remains the same, as it does not absorb in the region of the spectrum to be used in the tests. The details of this technique are described in the appendix.

Also, the transparency of DSSC containing VG20-TBPF dyes was evaluated using transmission tests carried out on devices specially produced for this evaluation and using a standardized metric. In general, AVT (average visible transmittance) is used as a reliable measure to assess the optical transparency of glass, allowing for comparing different products within a consistent metric. Consequently, AVT has been adopted in the photovoltaic industry as an aesthetic parameter [82]. It is defined as the weighted integration of the transmission spectrum of a photovoltaic module, considering the human eye's photopic response and the solar photon flux. Equation 23 presents the AVT calculation, where λ is the wavelength, T (λ) is the transmission of the tested device, V (λ) is the photopic response, and S (λ) is the solar photon flux (AM 1.5G).

$$AVT = \frac{\int T(\lambda)\, V(\lambda)\, S(\lambda)\, d\lambda}{\int V(\lambda)\, S(\lambda)\, d\lambda} \tag{23}$$

2.1. Key Electrical Parameters

The efficiency of DSSCs can be measured by basic electrical parameters obtained from the current-voltage density curve, the J-V curve. The short-circuit current density (J_{sc}), the open-circuit voltage (V_{oc}), the fill factor (FF) and the power conversion efficiency (PCE or η) are the parameters that offer insights into cell performance. Therefore, understanding the intrinsic physical meanings of these parameters and how they interact with each other is essential for evaluating and optimizing DSSCs for more efficient energy conversion. The details presented in this section are derived from the comprehensive studies by Kutlu, N. (2020) [83] and Sarker, S. et al. (2014) [84].

2.1.1. Short-circuit current density (J_{SC})

The sort-circuit current density represents the maximum current potential that the cell can generate. This parameter is measured in the short-circuit condition, i.e. when the resistance of the external circuit is zero, leading to a zero potential difference. In this condition, all the electrons generated flow freely through the external circuit and there is no voltage in the device. The value of J_{sc} is given as the amount of current per unit of area and is directly linked to the efficiency of the cell in converting sunlight into electric current. Using a dye that has a broad absorption spectrum, ideally extending into the infrared region, as well as reducing electron recombination losses, can maximize J_{sc}.

2.1.2. Open-Circuit Voltage (V_{OC})

Open-circuit voltage represents the maximum voltage that the solar cell can produce in the absence of a current flowing (J = 0). This condition occurs when there is no connection between the photoanode and the cathode and, therefore, the cell has an “open” circuit. During the measurement of this value, the DSSC is exposed to a sunlight simulator which leads to charge separation. After the injection of electrons into the semiconductor, a potential difference is created in the cell. As the terminals are connected to a circuit with extremely high resistance, current is not established and the maximum value of V is measured. A high V_{oc} value can be achieved by reducing the recombination rates between the electrons injected into the semiconductor and the oxidized redox pair in the electrolyte.

2.1.3. Fill Factor (FF)

The fill factor is a parameter that reflects the quality of the cell, defined by the equation 24.

$$FF = \frac{P_{max}}{J_{sc} \times V_{oc}} \tag{24}$$

The maximum power obtained (P_{max}) in a DSSC represents the operating point where the device delivers the highest power value, the product of the maximum current and voltage values outside of extreme short-circuit or open-circuit conditions. The product of $J_{sc} \times V_{oc}$ is a theoretical maximum power value, i.e. it is a parameter that helps define the potential performance of the cell, but which cannot be achieved in practice. A quality cell with P_{max} values close to the theoretical power limit leads to an FF close to 1, which translates into a J-V curve shaped like a square. FF values considered satisfactory are above 0.6, which indicates low series resistance and high resistance values for unwanted alternative paths, leading to low useful current losses.

2.1.4. Current Density-Voltage (J-V) Characterization

The main method for evaluating the efficiency of a cell is current density-voltage characterization. In this technique, the DSSC is illuminated with simulated sunlight, using a solar simulator that mimics the solar spectrum at AM 1.5G irradiation. This is a standard condition that simulates typical sunlight at mid-latitudes and provides irradiance of 100mW/cm^2, allowing consistent comparisons between different devices. Upon irradiation, the cell is subjected to a range of applied voltages, and the resulting current densities are measured. This technique makes it possible to extract the critical parameters J_{sc}, V_{oc}, and FF, from which the power conversion efficiency (PCE) is calculated. The J-V curve is constructed after normalizing the current density values by the cell's active area. This characterization is fundamental for evaluating the photovoltaic behavior of the device.

The J-V curve is typically divided into three regions:

1. **Short-Circuit Region (V ≈ 0)**: In this condition, J_{sc} reaches its maximum value, since all the charge generated is captured by the electrodes and flows through the external circuit without meeting resistance. This region of the graph reflects the efficiency of the light capture and charge separation processes. A low J_{sc} value may indicate that the dye has low light absorption, that electron injection is inefficient, and/or that the electrons injected into the semiconductor are recombining before reaching the external circuit.
2. **Open-Circuit Region (J ≈ 0)**: in the case of an open circuit, the resistance in the external circuit has its maximum possible value, minimizing or avoiding the current flow. Therefore, the photogenerated charges remain inside the cell and V_{oc}, which represents the difference between the energy levels of the semiconductor and the electrolyte, has a maximum value. This parameter is strongly influenced by the kinetic rates of recombination of the electrons injected with the redox mediator.
3. **Maximum Power Point (MPP)**: in the region between the short circuit and the open circuit is the point where the product of current and voltage is maximum, called MPP. At this point, the current and voltage have the highest possible values under operating conditions and therefore represent the maximum power achievable by a DSSC under illumination. The FF is calculated from the current and voltage values at the MPP.

2.1.5. Interpretation of the J-V Curve and Performance Metrics

From the values of V_{oc}, J_{sc}, and FF, the power conversion efficiency (η) can be calculated using equation 25, where P_{in} represents the incident power density, usually set at the standard value of 100mW/cm2. Efficient light absorption, electron injection, and dye regeneration processes result in a satisfactory J_{sc} value. Similarly, low recombination rates lead to a high $V_{oc,}$ and low internal resistance rates combined with good charge transport lead to an FF closer to 1.

$$PCE = \frac{V_{oc} \times J_{sc} \times FF}{P_{in}} \tag{25}$$

In practice, the values obtained are the result of a combination of processes. However, by analyzing the shape of the J-V curve, it is possible to suggest hypotheses about the internal operation of the cell. For example, a low V_{oc} reflects a low potential difference within the cell and could therefore suggest significant recombination rates at the semiconductor/electrolyte interface. Furthermore, this low potential difference may be the result of inefficient electron injection caused by poor alignment between the dye's excited state and the semiconductor's conduction band. A low J_{sc} value represents a low charge density in the internal circuit, which could be the result of a thin or irregular layer of adsorbed dye, poor light absorption, inefficient electron injection, or slow electron transport within the semiconductor. Finally, a low FF indicates the presence of a high series resistance and/or a low shunt resistance (current losses that occur due to the presence of unwanted alternative paths within the cell). These anomalies can be caused by the low conductivity of the electrode, the presence of short circuits, or the poor quality of the photoanode.

From the analysis obtained by J-V characterization, it is possible to identify critical points in the performance of DSSCs. This makes it clearer where to focus efforts to optimize the efficiency of these devices. This optimization could include, for example, the development of new cell designs and manufacturing methods, the use of innovative materials, the adoption of new dyes with a broader light absorption spectrum, and the application of different electrolyte compositions.

3. SubPc Dyes

Phthalocyanines (Pcs) dyes, synthetic analogs of porphyrin, have attracted significant scientific interest due to their strong absorption in the visible range. Pcs are well-known for their stability and improved light-harvesting properties in the far red- and near-IR spectral regions, making them widely used as sensitizers. However, the efficiency of Pc-based DSSCs is generally lower than that of porphyrin-based cells. Despite this, structural modifications to Pc molecules have successfully increased the performance of Pc-based solar cells, reaching efficiencies of up to 5.9% [85]. Recent research has boosted interest in these compounds, especially as advances in molecular dynamics have highlighted the structural and chemical flexibility of Pcs, allowing for customized photophysical characteristics [86]–[88].

The structural versatility of Pcs allows one or more isoindol units to be replaced by other hetero- or carbocycles. This flexibility has been used to create new Pc derivatives with customized absorption properties to better align with the solar emission spectrum on Earth. For example, removing an isoindol unit from the Pc nucleus results in SubPc analogs. Unlike the planar configuration of Pcs, SubPcs have a cone-like geometry that inherently reduces aggregation, a common issue that reduces the efficiency when in dye-sensitized solar cells (DSSCs). One of the main photophysical benefits of SubPcs is their strong absorption of light in the visible range (500-700 nm), which makes them efficient materials for harvesting light. For example, Verreet *et al.* [89] reported organic photovoltaic cells with a power conversion efficiency of 4% using a fluorinated fused subphthalocyanine dimer as a deep red absorption acceptor. SubPcs have thus emerged as promising active layer components in photovoltaic devices, especially due to the high open-circuit voltage (V_{oc}) values they allow.

SubPc dyes also stand out for their high thermal and photochemical stability, which favors the high durability of DSSCs. Moreover, they produce devices with high V_{oc} values due to the positioning of their energy levels which allows the excited electron to have a high probability of migrating from the LUMO to the conduction band of TiO_2, which favors charge separation, while the energy difference between the HOMO of the dye and the redox level of the electrolyte is high enough to prevent the electron from returning to the dye quickly. This supports a satisfactory V_{oc} [88].

Given that the DSSC samples studied here were produced in the laboratory, the dye to be used must suit the conditions of manual assembly. The choice of dye is very important and factors such as familiarity with the procedure should be considered. As these were the first DSSC samples to be produced in this study, SubPc was chosen because of the resistance to high temperatures and short-term stability of the resulting devices. During the assembly process, for a researcher in the process of learning, some fabrication steps may take longer to complete. Some of them require raising the temperature of the photoanode, for example, which can cause sensitive dyes, such as NIR, to burn out. SubPc dyes, on the other hand, show satisfactory resistance to the production process, even when carried out more slowly, in addition to the advantages mentioned above. As a consequence, this class of dyes proved to be ideal for application in the first devices produced.

3.1. Comparing four SubPc Dyes

Despite its potential, there are few reports on the use of SubPcs in DSSC. The first example of DSSCs based on SubPcs was reported by Mine I. *et al.* [88] using several axially and peripherally carboxylic acid-substituted SubPcs as photosensitizers. In this paper the compounds bearing an axial carboxylic moiety saw lower efficiencies than the substituted in peripheral positions, being the maximum efficiency 1.32%. The study also reported some SubPc derivatives with peripheral COOH anchoring groups to optimize the performance of the cells. However, these structural modifications failed to improve power conversion efficiency, probably because of the inadequate driving force for the electron injection of the dye into the CB of TiO_2 because of the low LUMO energy levels of the employed dyes. Later on, Gotfredsen *et al.* [90] reported a series of donor acceptor-functionalized SubPc derivatives as sensitizers in liquid- and solid-state DSSCs. In the first case, a power conversion efficiency of 0.46% was obtained with unsymmetric SubPc. The low conversion efficiency was explained via the dye desorption caused by liquid electrolytes which resulted in a low photocurrent density and overall conversion efficiency. When the same dye was used in solid-state DSSCs using a solid electrolyte, the current density increased 4 times, and the overall conversion efficiency reached 1.54%. This moderate conversion efficiency was attributed to low dye loading.

To explore this further, four SubPc (Figure 31) dyes with varying structural modifications were synthesized and analyzed for their impact on photovoltaic performance. This study was conducted in collaboration with Dr. Mine Ince from the Department of Organic Chemistry at the *Universidad Autónoma de Madrid*, where the dyes were synthesized. The production and characterization of the cells were carried out at the LRCS in Amiens, France. Each dye was designed to mitigate dye aggregation, optimize light absorption, and facilitate electron injections by incorporating diverse substituents. The choice of dye plays a crucial role in DSSCs, as an effective dye should cover the visible to near-infrared (NIR) spectrum and exhibit optimal band alignment with the TiO_2 conduction band.

As shown in Figure 31, all SubPc derivatives have bulky donor peripheral groups to reduce potential dye aggregation on TiO_2 surface. 4-ethynyl benzoic acid was used as an anchoring moiety, and 4-tertbutyl phenoxy substituents were introduced in axial position to increase the solubility and the chemical stability. For SubPcs 3 and 4, bulky thiophenol units were introduced at the peripheral positions of the macrocycles to increase their light-harvesting ability and electron-donating character of the SubPc.

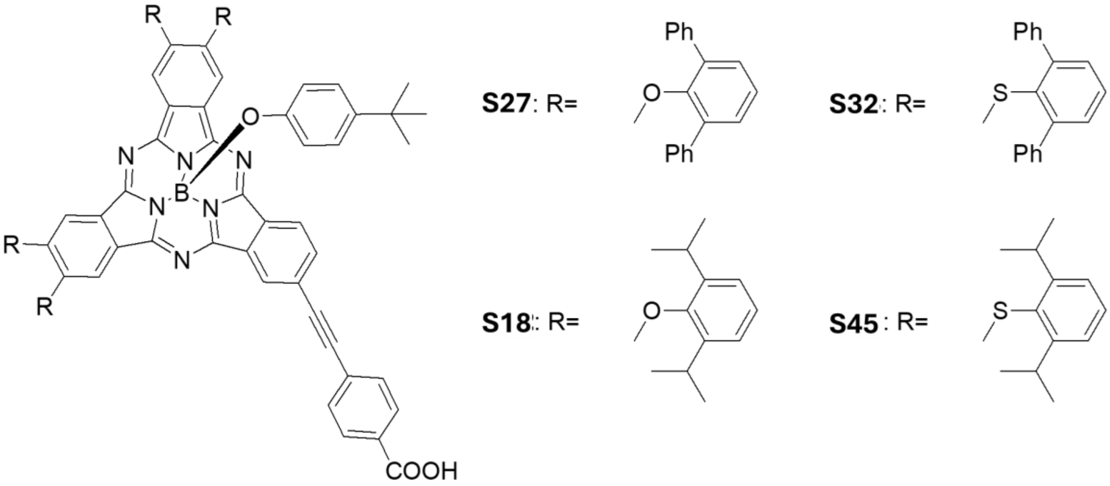

Figure 31. Molecular structures of the SubPc sensitizers S18, S27, S32, and S45, highlighting their distinct functional groups. S18 features an ether group, S27 includes an ether and phenyl groups, S32 contains a thioether and phenyl groups, and S45 incorporates a thioether group.

3.2. Manufacturing

The manufacturing process of DSSCs using SubPc dyes involves preparing the dye solutions in solvents such as ethanol (EtOH) and tetrahydrofuran (THF) without disaggregating agents added. The choice of solvent plays a significant role in dye adsorption on the TiO_2 surface and affects overall cell performance, with solvatochromic effects further influencing the dye's absorption and emission spectra based on solvent polarity, thereby impacting light absorption efficiency and charge transfer within the cell. Steady-state UV-Vis absorption and Fluorescence spectroscopy tests were carried out on these solutions. These solutions were also used to produce the DSSC devices.

DSSCs were assembled following the method described in the Methodology section and detailed in the appendix. The employed electrolyte is composed of 0.5 M of

LiI and 50 mM of I_2 in an acetonitrile solution. The devices' performances were evaluated under standard conditions, also described in the Methodology section, by measuring the open-circuit voltage (V_{oc}), short-circuit current density (J_{sc}), fill factor (FF), and overall efficiency (η).

3.3. Results and Discussion

3.3.1. Steady-state spectroscopy

The optical properties of SubPc dyes are essential for understanding their effectiveness as sensitizers in dye-sensitized solar cells (DSSCs). Subphthalocyanine (SubPc) compounds exhibit structures of strong absorption in the visible region due to their unique π-conjugated. The absorption spectra of SubPc dye solutions in THF are shown in Figure 32, revealing maximum absorption peaks (λ^{abs}_{max}) at different wavelengths. The S32 dye shows the most red-shifted absorption compared to the others, while S18 is shifted more toward the blue region. S27 and S45 fall in between. Figure 33 shows the emission spectra of the dyes studied, which have varied peaks as in the absorption spectrum. The λ^{emi}_{max} follow the same order as λ^{abs}_{max}. Table 7 summarizes the values found from the characterization via steady-state spectroscopy.

Table 7: Photophysical characteristics of the studied SubPc dyes: maximum absorption wavelength (λ^{abs}_{max}), maximum emission wavelength (λ^{emi}_{max}), Stokes shift ($\Delta\nu_{stokes}$), and quantum yield (Φ).

SubPc dye	λ^{abs}_{max} (nm)	λ^{emi}_{max} (nm)	$\Delta\nu_{stokes}$ (cm^{-1})	Φ
S18	580	587	205.60	0.18
S27	588	594	171.79	0.07
S32	602	612	271.43	0.51
S45	596	606	276.87	0.15

Dyes with electron-donating groups, such as thioether substituents in S32 and S45, exhibit a bathochromic shift (red-shift) in their absorption and emission maxima, resulting in absorption at longer wavelengths. The bathochromic shift is typical when electron-donating groups are introduced into molecules, as these groups increase the electronic density in the conjugated system, making it more capable of absorbing light at longer wavelengths [30]. This shift enhances the dyes' ability to harvest light efficiently, absorbing a broader range of visible light, which is crucial for maximizing DSSC performance.

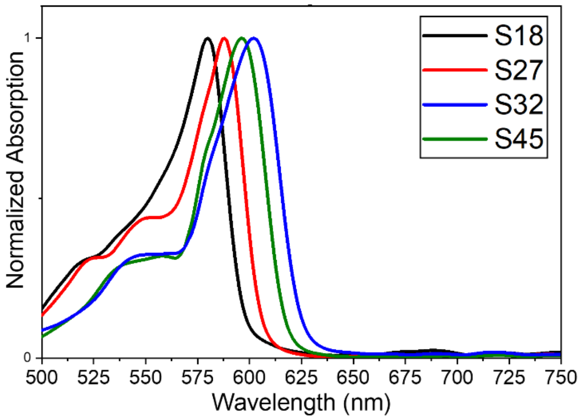

Figure 32. Absorption Spectra of SubPcs S18, S27, S32 and S45 in THF.

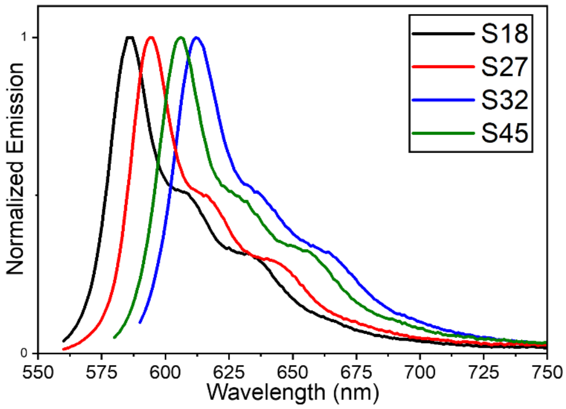

Figure 33: Emission Spectra of SubPcs S18, S27, S32 and S45 in THF.

3.3.2. *Photovoltaic Performance Analysis*

In the DSSC fabrication process, the photoanode is dipped into the dye solution to allow the dye molecules to adsorb onto the semiconductor layer. In the present study, dye solutions with a concentration of 0.1 mM in THF and ethanol were used in an attempt to observe the impact of the solvent in the dye solution for immersing the photoanode on the performance of the final DSSC. In addition to solvatochromic effects, these solvents can affect the dye adsorption on the semiconductor layer, influencing the number of molecules and the uniformity of the dye coverage on the photoanode. A uniform adsorption is important to ensure that an appropriate amount of dye is available for light collection. Furthermore, the evaporation rate of the solvent can have an impact on the adsorption conditions. Solvents that evaporate slowly generally allow for more controlled adsorption and can lead to more uniform dye layers. [31].

The fabricated devices underwent electrical characterization in an Oriel Solar Simulator, where the main electrical parameters were obtained and are shown in Tables 8 and 9. When using THF-based photoanode dipping solutions (Table 8), the device sensitized with S32 stands out for its high J_{SC} value, while also presenting satisfactory V_{OC} and FF. This combination results in the highest efficiency among the samples

(1.69%). On the other hand, when ethanol is used as a solvent (Table 9), the device sensitized with S18 exhibits higher V_{OC}, J_{SC}, and FF values, achieving a better performance with an efficiency of 1.32%.

When comparing the performance of the fabricated devices, it can be observed that DSSCs sensitized with S18 or S27 achieve higher efficiencies when the dyes are dissolved in ethanol solutions. In contrast, devices sensitized with S32 or S45 perform better when THF is used as the solvent. This behavior may be related to the solubility characteristics of the dyes in each solvent. Structurally, S18 and S27 share the presence of an ether functional group, which is replaced by a thioether group in S32 and S45, potentially influencing their solubility and interaction with the semiconductor.

The JV curves of the devices are shown in Figures 34 and 35. Analyzing the curves, it is evident that most of them have a nearly square shape, reflecting FF values that can be considered satisfactory (between 57% and 67%). This suggests the absence of significant issues such as excessive resistances or defects at the material interfaces. It also indicates that the manufacturing process was carried out successfully and efficiently. The V_{OC} values obtained (between 0.31 V and 0.44 V) are relatively low for DSSCs. This directly impacts the cells' efficiency and may indicate significant recombination rates between the electrons injected into the semiconductor and the electrolyte. It also suggests that the dyes used were not fully optimized to enhance charge separation. The better-performing samples showed J_{SC} values closer to the expected range (7.69 mA/cm² for S32 in THF and 5.18 mA/cm² for S18 in EtOH), although still low for DSSCs. This likely reflects limited light absorption by the dyes and inefficient electron injection.

Table 8: Photovoltaic performance parameters open-circuit voltage (V_{OC}), short-circuit current density (J_{SC}), fill factor (FF), and efficiency (η) of SubPc dyes in THF-based photoanode dipping solutions.

Solvent: THF				
SubPc Dye	V_{OC} (V)	J_{SC} (mA/cm^2)	FF (%)	η (%)
S18	0.33	3.58	60	0.72
S27	0.31	3.85	63	0.77
S32	0.38	7.69	58	1.69
S45	0.38	3.51	67	0.89

Table 9: Photovoltaic performance parameters open-circuit voltage (V_{OC}), short-circuit current density (J_{SC}), fill factor (FF), and efficiency (η) of SubPc dyes in EtOH-based photoanode dipping solutions.

Solvent: EtOH				
SubPc Dye	V_{OC} (V)	J_{SC} (mA/cm^2)	FF (%)	η (%)
S18	0.44	5.18	57	1.32
S27	0.41	4.06	65	1.11
S32	0.4	4.96	61	1.23
S45	0.39	3.06	65	0.79

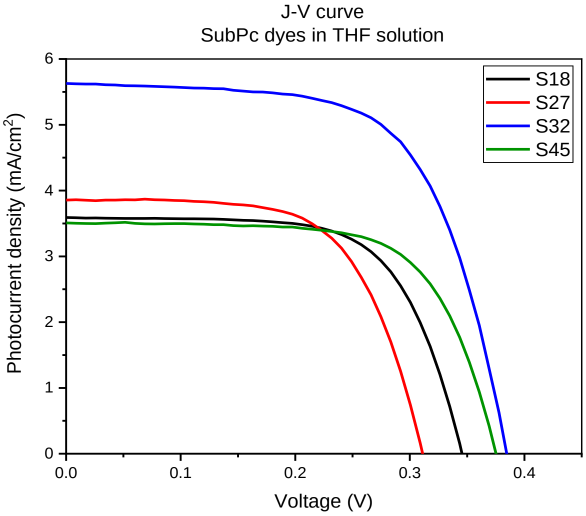

Figure 34. Evolution of JV curves of DSSCs fabricated using SubPc dyes as sensitizers in THF-based photoanode dipping solutions.

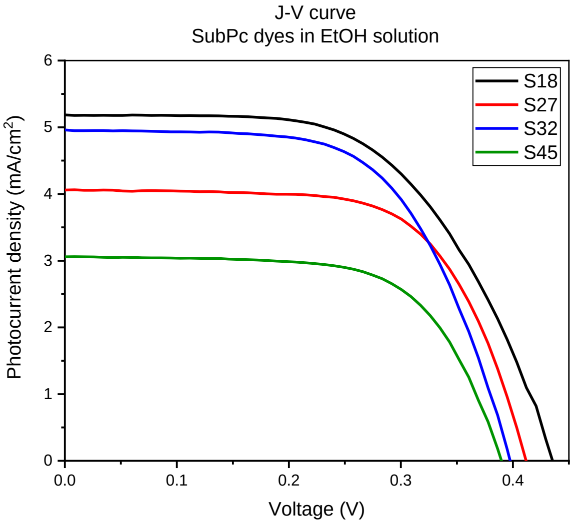

Figure 35. Evolution of JV curves of DSSCs fabricated using SubPc dyes as sensitizers in ethanol-based photoanode dipping solutions.

The best efficiency result was found for the device produced with S32 in THF (1.69%). This dye differs from the others in terms of structure, due to the presence of a thioether group and phenyl groups. As a result, it has more red-shifted absorption and emission spectra compared to the other dyes. This might be crucial for its better performance, since the sunlight spectrum has a significant intensity in this wavelength range, allowing the dye to absorb more light and, consequently, generate a greater number of electrons. In addition, S32 has the highest quantum yield value and is therefore more likely to generate excited states that can effectively transfer electrons to the semiconductor, resulting in better electron injection and minimizing losses due to nonradioactive decay processes. Finally, S32 has the second highest Stokes Shift value, which can also contribute to improved performance by reducing reabsorption losses within the system [32].

In general, the devices produced using S32 and S27 as sensitizers have good J_{SC} values in both ethanol and THF. Both dyes have phenyl group substituents in their structure that present extended π-conjugated systems, which facilitate the electron flow and broaden the light absorption spectrum [33]. These properties are crucial for achieving greater photoelectric conversion. Further investigation into the causes of the lower than expected J_{SC} and V_{OC} values and, consequently, relatively low efficiency values, IMVS/IMPS and Nano TAS tests were carried out. A bottleneck in the operating process of these cells needs to be found to create a more detailed hypothesis about the reasons behind the relatively low values found.

3.3.3. Intensity Modulated Photovoltage/Photocurrent Spectroscopy (IMVS/IMPS)

IMVS and IMPS are powerful techniques used to analyze electron recombination and transport dynamics within DSSCs, providing insights into the factors that govern their efficiency. IMVS measures the electron lifetime, which is associated with the recombination rate of electrons, while IMPS measures electron transport time, giving insight into the speed of electron movement within the device.

IMVS tests can be used to compare the samples in terms of their average electron lifetime in the semiconductor, i.e. the average time that the injected electron remains in the semiconductor before recombining with the oxidized dye (geminate recombination) or with the electrolyte's redox pair (non-geminate recombination), indicating the stability of the electron in the semiconductor [34]. Figure 36 (a) shows the data obtained from the IMVS tests carried out on the samples produced using the SubPc dyes in THF solution. The device produced with the S32 dye has the longest electron lifetime for the same voltage value. Following this, the devices with S45 and S27, with similar curve slopes. The sample corresponding to S18 comes last with a different curve slope. The lines fitted to the data for the different dyes in the IMVS graph have similar positions in the IMPS graph. However, IMPS measures the time taken for the injected electron to move through the semiconductor to the external circuit. The adjusted line showing the highest transport time values corresponds to the device produced using the S32 dye.

Figure 36 also displays the corresponding IMVS and IMPS graphs of the DSSCs produced using ethanol in the dipping solution. The graphs point out that the fitted lines behave similarly and that in both cases the device produced with S18 stands out from the others with longer transport time and longer electron lifetime values.

In addition to analyzing the graphs, the electron lifetimes and transport times for devices operating under the best conditions can be numerically compared using Equation 26. To perform this calculation, the highest modulus frequency value is considered, which corresponds to the highest voltage or current value recorded in the analysis. This frequency (f_{peak}) is directly related to the time components of the process, being the electron lifetime (τ_e) or the transport time (τ_t) through the semiconductor [35].

$$\tau_e \; or \; \tau_t = \frac{1}{2\pi f_{peak}} \tag{26}$$

The collected data also enables the calculation of the charge collection efficiency (η_{cc}), which measures the efficiency by which the electrons injected into the semiconductor are collected at the anode before recombining with the oxidized dye or the redox pair in the electrolyte. In other words, ηcc represents the portion of charges generated by the light that can be used to generate current in the external circuit [35]. Table 10 gives the estimated values for electron lifetime (τ_e), electron transport time (τ_t) and charge collection efficiency (η_{cc}).

In the experiments using THF as the solvent of dipping solution, the IMVS/IMPS analyses showed that S32-based DSSC had the longest electron lifetime. However, this same sample also had the longest electron transport time.

Table 10. Electron lifetime (τ_e), transport time (τ_t), and charge collection efficiency (η_{cc}) for SubPc sensitizers in THF and ethanol (EtOH).

SubPcs dyes in THF				SubPcs dyes in EtOH			
Dye	τ_e (ms)	τ_t (ms)	η_{cc}	Dye	τ_e (ms)	τ_t (ms)	η_{cc}
S18	39.98	2.52	0.94	S18	100.42	39.98	0.72
S27	20.04	4	0.83	S27	31.76	20.04	0.61
S32	50.33	10.04	0.83	S32	39.98	31.76	0.56
S45	31.76	2.52	0.93	S45	31.76	6.34	0.83

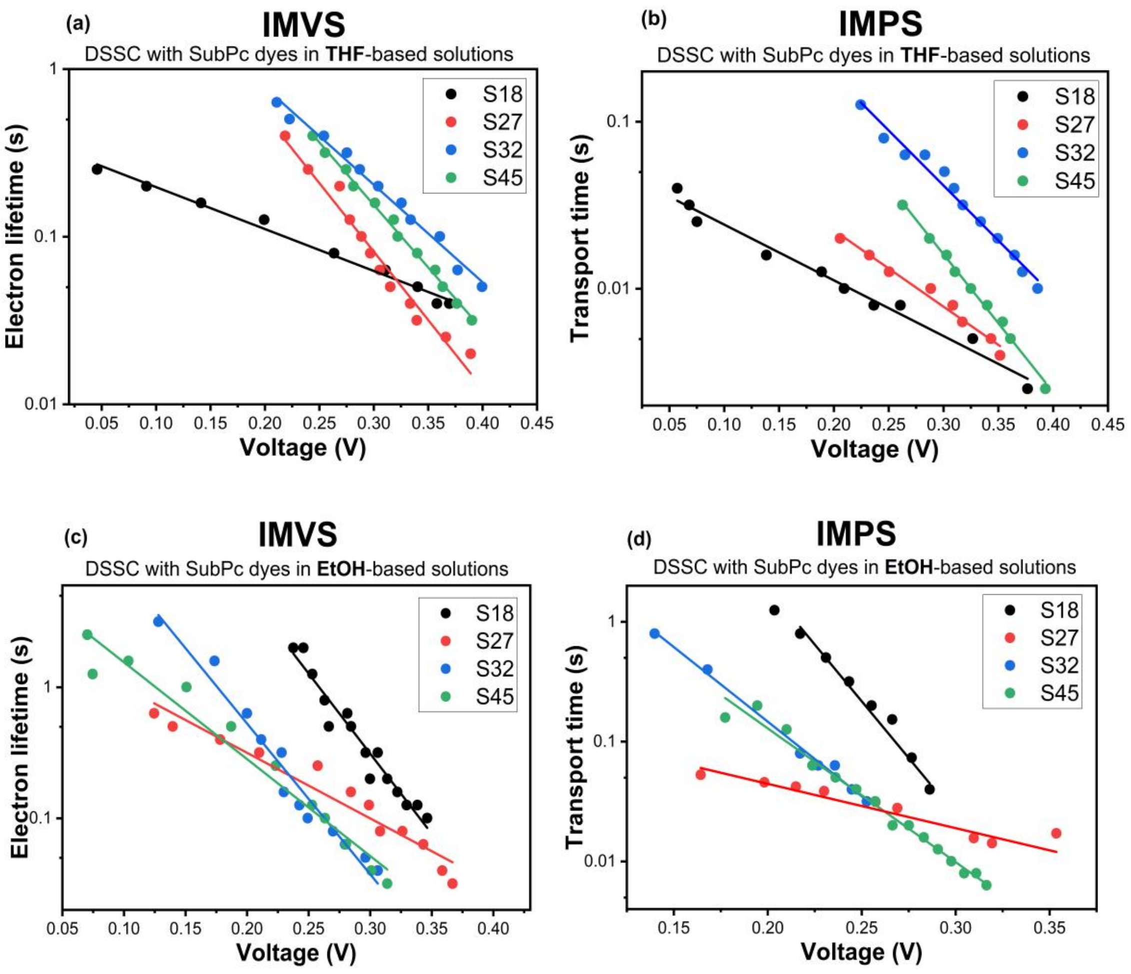

Figure 36. Evolution of the electron lifetime by IMVS (a, c) and the transport time by IMPS spectroscopy (b, d) for SubPc sensitizers in different solvents: (a, b) THF and (c, d) ethanol.

That means while the electron remains stable in the semiconductor for longer in S32-based sample compared to the others, the electron transport in its semiconductor layer is slower. These conditions lead this device to have a lower η_{cc} value than, for example, the S18-based device which, despite having a lower τ_e, has a low τ_t. Comparing the samples produced using EtOH as the solvent of dipping solution, it can be seen that the S18-based one achieved higher τ_e and τ_t values, a similar behavior presented by the sample based on S32 in THF, discussed earlier. In both THF and EtOH, we can see that the samples with the highest efficiency in generating energy (S32 and S18, respectively) also had the highest τ_e values, indicating that the lifetime of the electron in the semiconductor is possibly the factor that has the greatest direct impact on efficiency in this study.

3.3.4. Picosecond Transient Absorption Spectroscopy (Nano TAS)

For a more detailed analysis of the processes of geminate recombination and dye regeneration, the Picosecond Transient Absorption Spectroscopy (Pico TAS) technique was used. In this approach, two overlapping beams, called pump and probe, interact with the DSSC. The pump beam excites the sample at a specific wavelength, while the probe beam performs a scan to detect, at different wavelengths and time scales, the transient absorption phenomena associated with the photoinduced processes, allowing detailed analysis of these dynamic processes. More specific information on how this technique was performed can be found in the appendix. The following tests were carried out on the LRCS picosecond TAS setup with a pump at 600 nm.

As the sample based on S32 in THF showed the best efficiency results, this dye was chosen to be used in the preparation of the specific DSSC sample for the PicoTAS assay. The fitting of the experimental decay data was done using a Python code developed at LASIRe and made available as supplementary material. The code employs a model based on a quasi-analytical convolution with a Gaussian pulse, which allows the data to be adjusted considering the temporal shape of the excitation pulse (pump) and separating the instrumental effects from the transient phenomena of the process. The time component values involved in the recorded phenomena can be estimated through the fit.

Through TAS tests, it is possible to describe the processes of geminate recombination and dye regeneration, since both have time scales compatible with the technique. To investigate the dynamics of geminate recombination, a DSSC must be produced where the electrolyte has no redox pair, called NR (or non-redox couple), thus ensuring that all the injected electrons are recombined. The process of non-geminate recombination occurs on a time scale of milliseconds to seconds, while geminate recombination occurs on a time scale of nanoseconds to microseconds. The TAS in NR samples therefore provides the lifetime of the transient specimen involved in geminate recombination. Meanwhile, to investigate the dye regeneration process, a full-electrolyte (FE) sample is produced, where the redox pair is present in the electrolyte. The DSSC circuit is thus closed, allowing the dye to regenerate. Although geminate recombination can also be detected, in this case the phenomena can be identified and treated separately since each species (such as the oxidized dye, the excited dye or the recombination intermediate) has a specific spectral signature.

The transient absorption spectra obtained for samples S32 FE (with complete redox electrolyte) and S32 NR (without redox pair) provided information on the dynamics of dye regeneration and geminate recombination, which are fundamental to understanding the relatively low efficiency of the produced devices. For the S32 FE sample (Figure 37), a prominent band was found in the region around 650-710 nm, which can be attributed to the oxidized dye (S32+), formed after the electron injection into the semiconductor. This band was observed at all the time scales investigated. In the 50 ns test, the band grows fast, reaching maximum intensity at around 14 ns, followed by a decay that does not reach 0 intensity at the end of the interval. At longer times, such as the 2 μs test, the band exhibits similar behavior, growing up to around 0.4 μs before decaying, again maintaining a residual intensity at the end of the test. Finally, in the 5 μs test, this band grows more slowly, reaching a maximum at approximately 1 μs and gradually decreasing, without disappearing completely at the end of the interval.

For the S32 NR sample (Figure 38), a similar behavior was observed in the 650-700 nm band for the 2 μs test, growing until around 0.4 μs before starting to decay, with a residual intensity at the end. However, in the 50 μs test, an additional peak was detected at 810 nm, possibly associated with an intermediate state of recombination or an electronic transition of the dye, which disappears almost completely at the end of the interval. These spectra provide evidence of the competitive dynamics between geminate recombination and regeneration, which were analyzed quantitatively by fitting decay curves.

The values obtained by fitting the TAS data highlight characteristic times that explain the processes involved (Figure 39). For S32 FE, the regeneration time of the oxidized dye (τ_{reg}) was determined as 0.594 μs, through a triexponential fit, indicating that the redox pair in the electrolyte can regenerate the oxidized dye relatively quickly. In S32 NR, in the absence of regeneration by the redox pair, the average geminate recombination time (τ_{grec}) was set as 1.264 μs, from a biexponential fit, reflecting that the injected electrons have a significant probability of recombining with the oxidized dye in very short times.

The TAS results allow us to explain the main limitations of the device. For the S32 FE sample, the 650-700 nm band is dominated by the oxidized dye, and the incomplete decay of the band at all time scales investigated suggests that part of the oxidized dye is not regenerated before undergoing geminate recombination. Direct competition between regeneration and recombination is evident since the characteristic times τ_{reg} (0.594 μs) and τ_{grec} (1.264 μs) are in the same order of magnitude, which favors considerable losses of injected electrons. For S32 NR, the absence of the redox pair exposes the predominant role of geminate recombination, as highlighted by the short τ_{grec}.

By integrating these results with the IMVS and IMPS data and the maximum overall efficiency of the cell (1.69%), a more complete interpretation can be constructed. The electron transport time in the semiconductor (τ_t = 10.04 ms) indicates that charge transport is efficient, while the average electron lifetime (τ_e = 50.33 ms) suggests that the electrons have enough time to reach the electrode before recombining. However, the short geminate recombination time (τ_{grec} = 1.264 μs) observed in the TAS tests demonstrates that a large part of the injected electrons is lost before they even begin to transport through the semiconductor. This behavior explains the cell's low J_{SC}, reducing its overall efficiency [36]. In addition, the closeness of the regeneration and geminate recombination times in S32 FE intensifies the competition between the processes, further compromising performance [37].

These results indicate that the limited efficiency of the solar cell sample based on the S32 dye is directly related to the imbalance between regeneration and geminate recombination. Although charge transport in the semiconductor is efficient, as evidenced by the times τ_t and τ_e, losses due to geminate recombination predominate. The short regeneration time τ_{reg} is promising but needs to be significantly faster than τ_{grec} to minimize losses. Evidence suggests that improvements in efficiency can be achieved by modifying the dye or electrolyte, optimizing the TiO_2/dye interface to reduce unwanted recombinations.

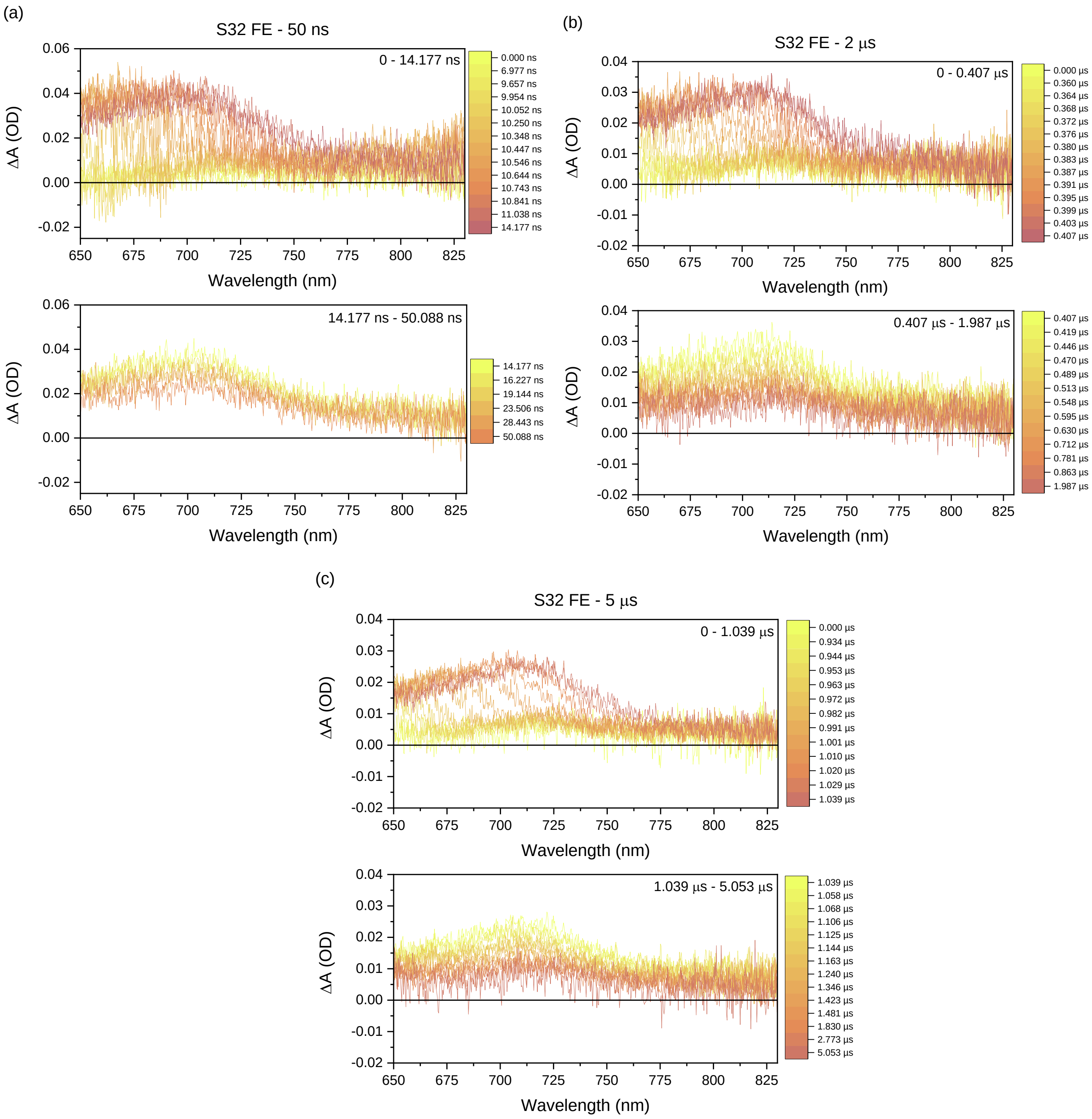

Figure 37. Transient absorption spectra of the DSSC full-electrolyte system based on the S32 dye measured at (a) 50 ns, (b) 2 μs, and (c) 5 μs in the near-infrared region (650–825 nm). For each timescale, the top panels show the initial evolution of the excited- state dynamics, while the bottom panels show the decay process and spectral shifts over time. The color gradient indicates the temporal progression of the transient absorption signal.

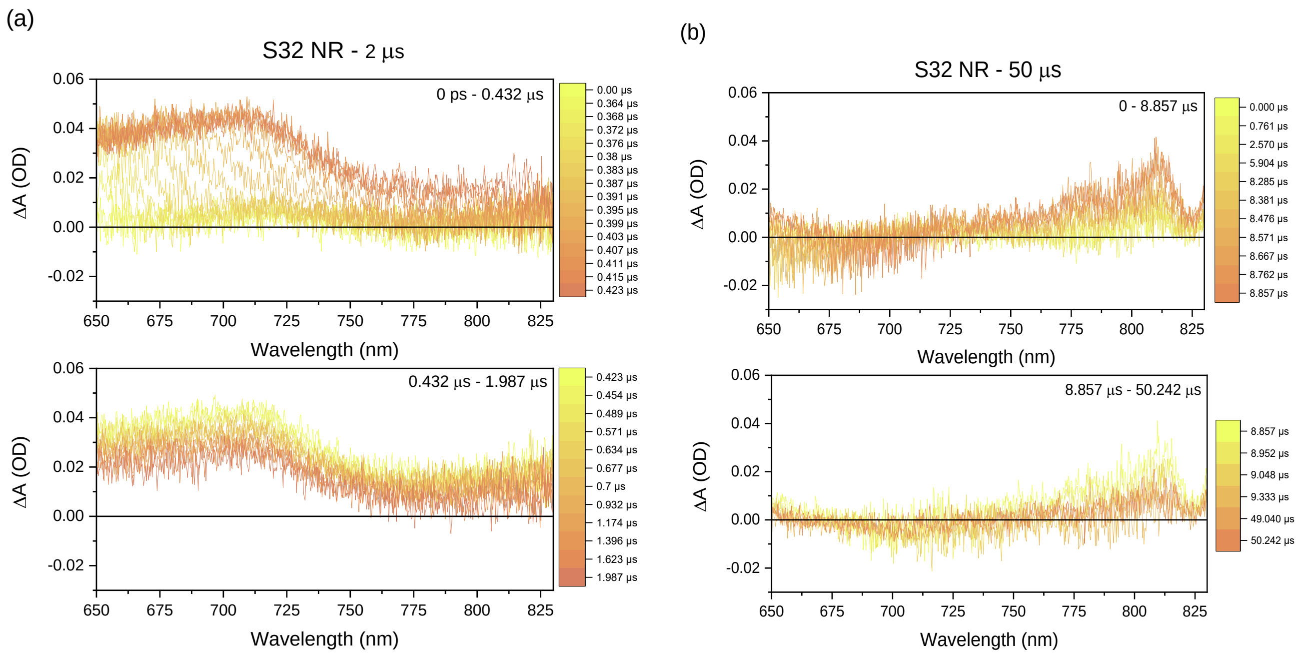

Figure 38. Transient absorption spectra of the DSSC non-redox couple system based on the S32 dye measured at (a) 2 µs, and (b) 50 µs in the near-infrared region (650–825 nm). For each timescale, the top panels show the initial evolution of the excited-state dynamics, while the bottom panels show the decay process and spectral shifts over time. The color gradient indicates the temporal progression of the transient absorption signal.

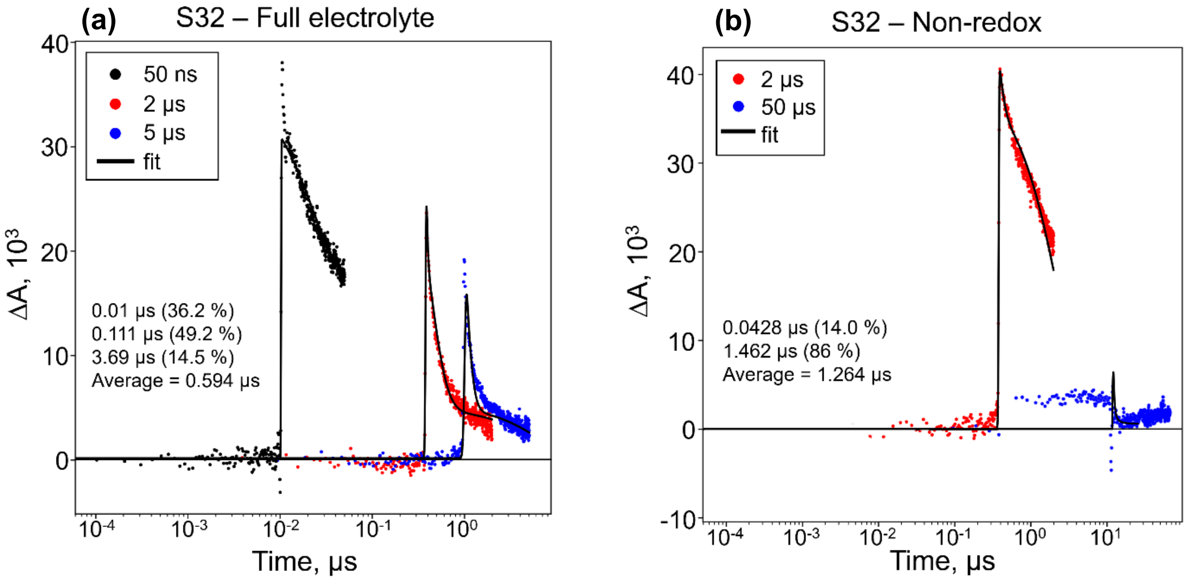

Figure 39. Kinetic decay analysis of the transient absorption signals for the S32 dye in (a) the full-electrolyte (FE) configuration and (b) the non-redox couple (NR) configuration. The measurements were conducted at different delay times: 50 ns (black), 2 µs (red), and 5 µs (blue). The solid black lines represent exponential fits to the data. The extracted lifetimes, the time components and their respective contributions are displayed in the plots.

3.4. Conclusions and Perspectives

This study explored the synthesis, characterization, and performance evaluation of DSSCs based on SubPcs dyes, using techniques such as TAS, IMVS/IMPS and steady-state spectroscopy. Key results from each technique provided critical information on the photophysical behavior and performance limitations of these devices, culminating in a comprehensive understanding of the underlying mechanisms.

From the steady-state spectroscopy, the SubPcs showed absorption and emission profiles strongly influenced by their structural modifications, with S32 showing the most red-shifted spectrum, evidencing its greater ability to capture light in the visible range. DSSC devices were satisfactorily constructed with the four dyes studied, using THF and ethanol as solvents for the sensitizer solutions. The satisfactory FF values, found at between 57% and 67%, reflect the absence of significant anomalies, such as inadequate resistances or defects in the interfaces, demonstrating that the fabrication of the cells was conducted efficiently. These properties, together with the higher quantum yield of S32, contributed to its better photovoltaic performance, reaching a maximum efficiency of 1.69% when dissolved using THF as the dipping solution solvent. However, the relatively low efficiencies of SubPc-based devices compared to other sensitizers reflect the need for further optimization of the molecular structures and energy alignment of these dyes.

IMVS/IMPS measurements revealed that the electron lifetime (τ_e = 50.33 ms) was significantly longer than the transport time (τ_t = 10.04 ms) for devices based on S32 in THF, indicating relatively stable electron populations in the semiconductor. However, the relatively high transport time contributed to a moderate charge collection efficiency (η_{cc} = 0.83), consistent with the observed photogenerated current densities. These results highlight the need to balance transport and recombination dynamics to improve overall performance.

TAS analysis provided crucial information on the competitive dynamics between regeneration and geminate recombination processes. For S32 FE, the regeneration time (τ_{reg} = 0.594 µs) was relatively short, indicating an efficient interaction between the dye and the electrolyte. However, the comparable geminate recombination time (τ_{grec} = 1.264 µs) revealed significant charge losses before complete regeneration, limiting the photogenerated current of the device. For S32 NR, TAS identified a transient intermediate at 810 nm, potentially indicating recombination pathways specific to redox-free systems.

Overall, this work achieved its objectives by synthesizing and characterizing SubPc-based DSSCs, identifying the best-performing dye, and analyzing their photophysical properties using advanced techniques such as TAS. Direct comparison with other studies is limited by the lack of works in the literature employing a similar approach, especially with a detailed analysis of dynamic behavior by TAS, which underscores the relevance of this study in establishing a starting point for understanding the performance and photophysical characteristics of SubPc-based devices. Future studies should focus on mitigating recombination pathways and improving interactions between dye and TiO_2, to maximize light absorption and charge separation, thus improving the performance of these promising sensitizers.

4. VG20-TBPF dye

VG20 class dyes are known as an attractive option for DSSCs. These dyes, derived from polymethine cyanines, have been designed to absorb light in the near-infrared (NIR) spectrum, allowing solar cells to operate with a high average visual transmittance (AVT), crucial for architectural and electronic applications. In contrast to conventional photovoltaic technologies like crystalline silicon cells, which are opaque and optimize absorption in the visible spectrum, VG20 dyes employ a selective method, absorbing light in regions invisible to the human eye, typically beyond 800 nm [11]. This approach is especially beneficial in contexts where aesthetics is essential, such as incorporation into building facades, solar windows, and transparent electronic gadgets, all while preserving competitive energy conversion efficiency. Research indicates that DSSCs utilizing VG20 can get an average visible transmittance (AVT) of up to 76% and a power conversion efficiency (PCE) of 3.1% [68], thereby establishing them as a viable technology in both technical and economic contexts for diverse applications.

The molecular structure of VG20 is crucial to its unique features (Figure 40). Dyes in this category contain a symmetrical polymeric structure, characterized by significant absorption in the near-infrared range and a high molar extinction coefficient. These attributes ensure that an extensive number of infrared photons is absorbed and transformed into electrical energy, while visible light is largely transmitted, enhancing the devices' transparency. Moreover, VG20 is designed to chemically bond to the surfaces of semiconductor oxides like TiO_2, which supports DSSCs. This chemical contact is crucial for electron injection, whereby excited electrons are transported to the semiconductor's conduction band, resulting in electric current generation. Nonetheless, despite its outstanding efficiency, VG20 faces inherent restrictions that impact its practical and commercial viability. The main issues include the formation of molecular aggregates on the TiO_2 surface, limited stability under adverse environmental conditions, and the occurrence of electron recombination processes, which decrease the overall efficiency of the device. These challenges are especially significant in outdoor applications, such as building facades, where devices survive long exposure to variations in temperature, humidity, and bright sunshine [20], [91].

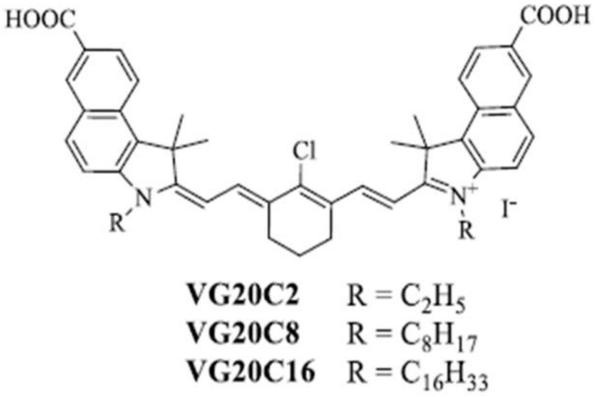

Figure 40. Molecular structures of the VG20 sensitizers (VG20C$_2$, VG20C$_8$, and VG20C$_{16}$) with varying alkyl chain lengths (R = C_2H_5, C_8H_{17}, and $C_{16}H_{33}$) [91].

Molecular aggregation is one of the main factors limiting the performance of VG20 in DSSCs. When dye molecules form aggregates on the TiO_2 surface, the efficiency of electron injection is reduced, as the interface between the dye and the semiconductor becomes less efficient. This is because the electronic properties of aggregated molecules differ significantly from isolated molecules, which affects charge transfer. In addition, the formation of aggregates can reduce the amount of light absorbed by the dye, negatively impacting energy conversion. Another significant problem is the chemical and thermal instability of VG20, which makes it susceptible to degradation under prolonged operating conditions. This degradation reduces not only the efficiency but also the useful life of the devices, compromising their viability for commercial and architectural applications that require durability and reliability.

To overcome these limitations, a variant of VG20 was developed, called VG20-TBPF (Figure 41), which introduces a functionalized counter-ion (tetrabromophenylfluorone, or TBPF) into its molecular structure. This modification was designed to directly address the main challenges associated with VG20, offering significant improvements in terms of performance and stability. The VG20-TBPF is based on the VG20-C_{16} structure, as it is already known that the presence of longer alkyl chains, such as the 16-carbon chain in VG20-C_{16}, helps to reduce molecular aggregation [68]. The TBPF counter-ion acts as a molecular spacer, reducing aggregation between the dye molecules and ensuring uniform coverage on the TiO_2 surface. This characteristic is essential for improving the interaction between the dye and the semiconductor, promoting more efficient charge transfer. In addition, the perfluorinated groups in TBPF give the dye greater thermal and chemical resistance, protecting it against degradation caused by prolonged exposure to light and heat. This improvement in stability is particularly relevant for outdoor applications, where devices need to operate reliably for years without significant loss of performance.

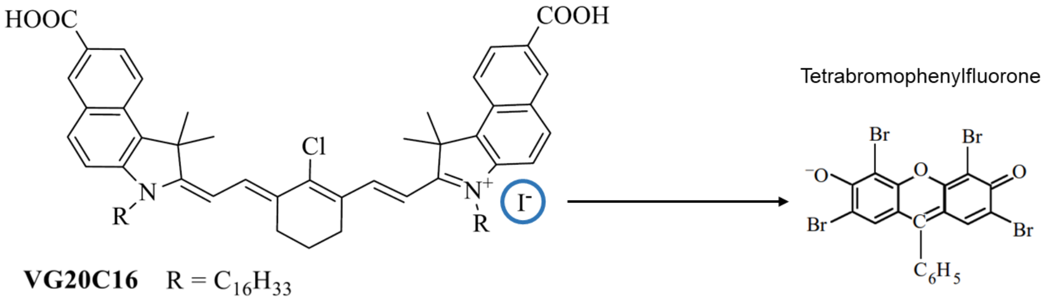

Figure 41. Chemical structures of VG20C_{16} (left) and the tetrabromophenylfluorone counter-ion (right). VG20 features a long alkyl chain ($R = C_{16}H_{33}$) and a chlorinated central core, with tetrabromophenylfluorone replacing iodide (I^-) as the counter-ion.

In addition to improving stability and reducing aggregation, VG20-TBPF has significant advantages in the energetic alignment of its HOMO (highest occupied molecular level) and LUMO (lowest unoccupied molecular level) levels with the redox potentials of the electrolyte used in the DSSCs. This adjusted alignment ensures efficient electron injection and dye regeneration operations, thus decreasing charge losses from recombination. This adjusted alignment promises efficient electron injection and dye regeneration operations, hence reducing charge losses from recombination. Despite the absence of practical research on VG20-TBPF, its molecular architecture indicates the possibility for enhanced energy conversion efficiency and superior performance relative to traditional VG20. These expectations are based on theoretical insights suggesting that the structural changes in VG20-TBPF could effectively handle significant issues faced by DSSCs. VG20-TBPF offers an innovative standard for the design of photovoltaic dyes by addressing issues such as molecular aggregation, chemical instability, and inefficiencies in charge transfer.

4.1. Manufacturing following the Standard Fabrication Method

This study aimed to investigate the performance of DSSCs using VG20-TBPF, comparing them with VG20-based devices. Initially, DSSCs were produced using the regular fabrication method, followed by trials using an alternative method that sought to reduce the thickness of the semiconductor layer. The influence of different concentrations of CDCA on the efficiency and transparency of the devices was evaluated.

For the regular method, the photoanodes were fabricated by printing the TIO_2 layer and dipping in the VG20-TBPF solution to promote its adsorption. The dye solution was prepared in a 0.1 mM solution in DMSO/EtOH (1:9 v/v), to which different concentrations of CDCA were added (0, 5, 10 and 30 mM). The electrolyte used contained 1 M DMII and 0.75 M LiI in thioethane/acetonitrile (115 µL/385 µL). Fabrication and testing followed the standard procedures described in the Appendix. After production, the devices were characterized to determine parameters such as efficiency, short-circuit current (J_{SC}), open-circuit voltage (V_{OC}), and average visible transmittance (AVT). It is expected that CDCA will act as a dispersing agent, reducing the molecular aggregation of the dye and thus promoting greater electron injection efficiency and a more uniform organization of the dye on the semiconductor surface. In addition, its influence on the transparency of the devices was evaluated based on AVT measurements.

An alternative method for fabricating the photoanodes was explored, using thinner semiconductor layers applied via *spin coating*. To do this, a solution containing TiO_2 paste (30 NR), and dry ethanol was prepared. At each stage, 60 μL of the solution was deposited on the glass and subjected to *spin coating* at a speed of approximately 1000 rpm for 15 seconds. After *spin coating*, the films were dried on a plate heated to 200 °C for 2 minutes. The process was repeated to form multiple layers, resulting in photoanodes with 1, 3, 6 and 9 layers. The photoanodes prepared using the alternative method were sensitized using two different procedures. In the first, the photoanodes were immersed during 24 hours in a solution of VG20-TBPF (0.3 mM in DMSO/EtOH with CDCA). In the second, sensitization was carried out using *spin coating* with the same solution. In this case, four layers of 60 μL each were applied successively, with rotation of 1000 rpm for 30 seconds for each layer, allowing drying between depositions. The devices manufactured by both methods were characterized consistently, evaluating parameters such as conversion efficiency (PCE), J_{SC}, V_{OC} and AVT. All the tests were carried out under the conditions previously described.

4.1.1. Optical and electrochemical properties of VG20-TBPF in solution

The VG20-TBPF dye in solution shows a clear absorption band in the NIR region, with a maximum at λ^{abs}_{max} = 834 nm, corresponding to the S_0-S_1 electronic transition (Figure 42a). A shoulder observed at 765 nm is mainly attributed to vibronic states in the molecule. However, this shoulder can also be influenced by the presence of H aggregates in the self-organized monolayers. This absorption characteristic positions the dye band outside the photopic response range of the human eye. The fluorescence of VG20-TBPF exhibits a sharp emission band at λ^{emi}_{max} = 847 nm, resulting in a Stokes shift of 183 cm^{-1}.

Cyanine dyes, including VG20-TBPF, tend to form molecular aggregates, which can affect their performance in DSSCs. To mitigate this problem, chenodeoxycholic acid (CDCA) was introduced into the dye solution in proportions of 1:30 and 1:50 of VG20-

TBPF:CDCA ratio. In addition, the dye solution was prepared at a low concentration (0.1 mM) to minimize aggregation. Increasing the concentration of CDCA in the VG20-TBPF solution did not significantly affect the amplitude of the vibronic shoulder or the width of the absorption band (Figure 42b). This observation suggests that the formation of H-type aggregates is unlikely in the DMSO/ethanol (1:9 v/v) solvent mixture under these experimental conditions.

The absorption and emission characteristics of VG20-TBPF proved remarkably similar to those previously reported for VG20-C16, which showed λ^{abs}_{max} = 834 nm for absorption and λ^{emi}_{max} = 850 nm for emission. These values, reported earlier [68], are in line with the results obtained in this study, reinforcing the similarity of the optical properties of the two dyes under similar experimental conditions. This consistency highlights the reliability of VG20-TBPF as an alternative to VG20-C_{16}, with the potential for similar applications in DSSCs and transparent photovoltaic technologies.

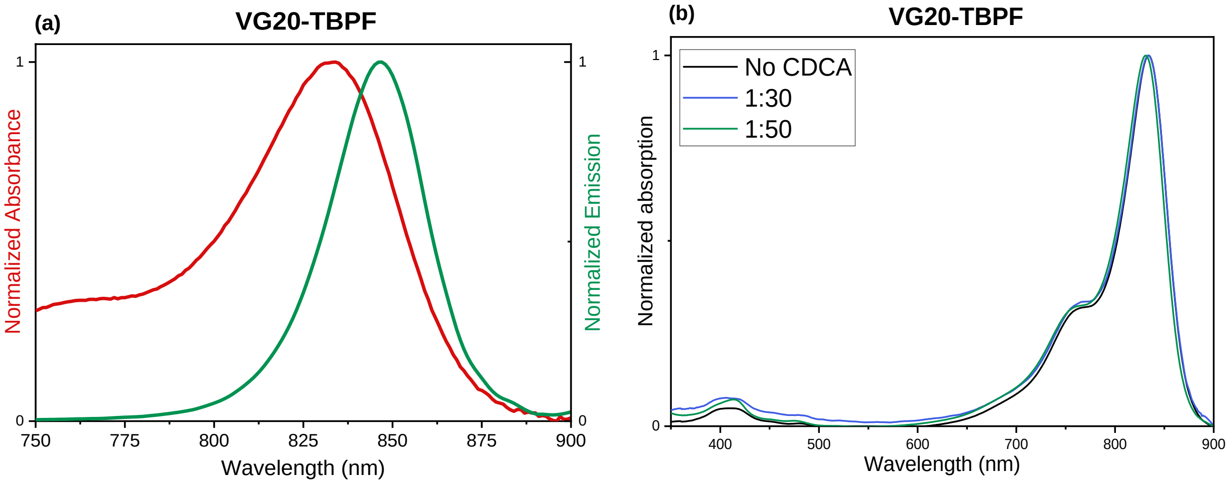

Figure 42. (a) Normalized absorbance and emission spectra of VG20-TBPF. The absorbance peak is centered at 834 nm, while the emission peak appears at 850 nm. (b) Normalized absorption spectra of VG20-TBPF with varying concentrations of CDCA (no CDCA, 1:30, and 1:50 ratios)

4.1.2. Photovoltaic performance of VG20-TBPF-based DSSCs

DSSCs were manufactured using the conventional method described in the methodology, using the specified electrolyte and VG20-TBPF solutions with different concentrations of CDCA. The results obtained are summarized in Table 11 and represented by the curves of photocurrent density as a function of voltage (J-V), shown in Figure 43. These data provide insights into the impact of CDCA on the performance of the devices and highlight how the modulation of this additive influences key parameters of the DSSCs.

Table 11 shows the photovoltaic parameters obtained for different proportions of CDCA. There is a significant increase in the V_{OC}, $J_{SC,}$ and efficiency (η) values as the concentration of CDCA increases. In the case without CDCA (1:0 ratio), the devices showed a V_{OC} of 0.22 V, J_{SC} of 3.03 mA/cm² and a total efficiency of only 0.37%. With the inclusion of CDCA in increasing concentration, the parameters improved progressively. For the highest ratio tested (1:300), the devices reached a V_{OC} of 0.35 V, J_{SC} of 10.17 mA/cm², and an efficiency of 2.18%, representing a significant increase in overall performance.

The J-V curves shown in Figure 43 corroborate the results in the table, demonstrating a clear improvement in the short-circuit current density (J_{SC}) as the concentration of CDCA increased. The curve corresponding to the 30 mM concentration (1:300 ratio) shows the highest current density, indicating that the higher proportion of CDCA promoted a more efficient device. This behavior is in line with the known role of CDCA, which acts as a molecular aggregation inhibitor. By reducing the formation of dye aggregates on the semiconductor surface, CDCA allows for a more uniform organization of the molecules, facilitating the injection of electrons into the TiO_2 conduction band and improving the dye regeneration process. Another important point to note is the behavior of the fill factor, which varied between 50% and 56% for all concentrations of CDCA. Despite its modest increase, this stability of the FF shows that resistive losses and the overall quality of the devices remained under control throughout the different tests. This suggests that the improvements observed in the devices can be attributed mainly to the greater injection efficiency and charge regeneration provided by CDCA, rather than changes in the charge of transport processes or internal resistive losses. The increase in V_{OC} also deserves attention, as it went from 0.22 V (for 1:0) to 0.35 V (for 1:300). By avoiding aggregates and improving the distribution of the dye molecules, CDCA enhances charge separation and increases the density of electrons available to generate current.

Finally, the overall efficiency of the devices increased noticeably with the higher concentration of CDCA. The value of 2.18% obtained in the 1:300 ratio is significantly higher than in the condition without CDCA, confirming the effectiveness of this additive in improving photovoltaic performance. Overall, the results presented show that the inclusion of CDCA in VG20-TBPF solutions not only optimizes key photovoltaic parameters such as J_{SC} and efficiency but also demonstrates efficient control over aggregate formation and FF stability. The combination of improvements observed in electrical parameters and molecular organization highlights the essential role of CDCA as an additive for DSSCs, validating its inclusion as an effective strategy for improving performance in dye-sensitized solar cell technologies.

Table 11. Photovoltaic performance parameters open-circuit voltage (V_{OC}), short-circuit current density (J_{SC}), fill factor (FF), and efficiency (η) of VG20-TBPF-based DSSC.

VG20-TBPF:CDCA	V_{OC} (V)	J_{SC} (mA/cm^2)	FF (%)	η (%)
01:00	0.22	3.03	52	0.37
01:50	0.23	4.22	54	0.54
1:100	0.27	5.63	50	0.81
1:300	0.35	10.17	56	2.18

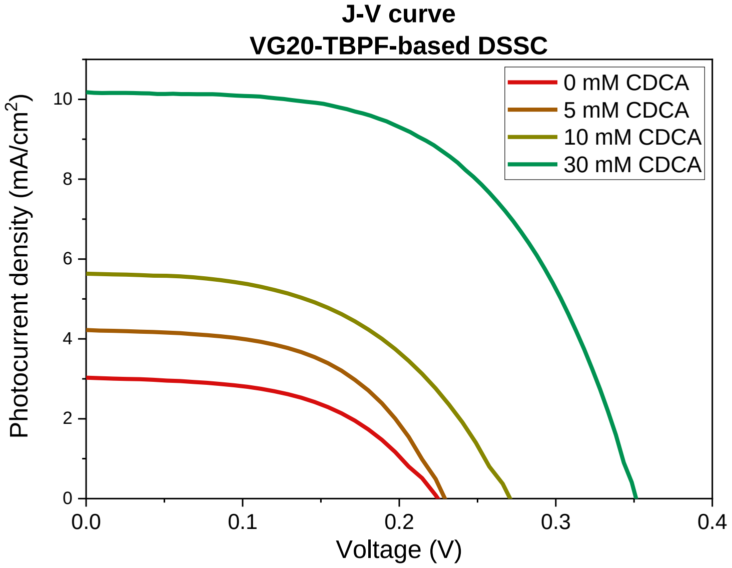

Figure 43. J-V curves of VG20-TBPF-based DSSCs with varying concentrations of CDCA (0 mM, 5 mM, 10 mM, and 30 mM). The data demonstrate the impact of CDCA concentration on the photovoltaic performance of the cells, including short-circuit current density (J_{SC}), open-circuit voltage (V_{OC}), and overall efficiency.

In terms of efficiency, VG20-TBPF showed a value of 2.18% for the 1:30 ratio, surpassing the 1.9% achieved by VG20 in the same ratio. This result highlights the potential of VG20-TBPF to deliver superior performance under optimized conditions. The introduction of TBPF as the counter-ion combined with the action of CDCA, may have contributed to a better distribution of the dye on the semiconductor surface, minimizing the formation of aggregates and improving electron injection efficiency.

4.1.3. IMVS/IMPS analysis

The results obtained are shown in Figure 44, corresponding to the IMPS and IMVS analyses, respectively. According to the curves, the sample with the highest proportion of CDCA (1:300) consistently showed the longest transport times and electron lifetimes for the same voltage value in both analyses. This suggests that the addition of CDCA probably reduces recombination processes in the semiconductor, especially at higher concentrations. Comparing the curves, the devices with the lowest proportion of CDCA (1:0 and 1:50) showed the shortest lifetimes and transport times, indicating a higher recombination rate and a possible lower efficiency in charge transport.

The fitted graphs indicate that the presence of CDCA, particularly in the 1:300 ratio, improves electron stability in the semiconductor and reduces recombination-related losses. This is in line with what is expected for CDCA, which acts as a molecular aggregation inhibitor, promoting more uniform coverage of the dye on the TiO_2 surface and optimizing the electron injection and transport process. However, when considering the estimated numerical data calculated by Equation 26 and presented in [39], it is important to adopt a conservative analysis. The lifetime (τ_e) and transport time (τ_t) values obtained between the samples are very close, which makes it difficult to infer significant differences based solely on these numerical estimative. For example, the τ_e values for the 1:50, 1:100, and 1:300 samples are almost identical (63 ms), with differences within the margin of error expected for the technique. Similarly, the τ_t values show limited variations, with the 1:300 sample showing a slight reduction to 15 ms, but no substantial deviations from the other samples. This closeness in the values reflects the estimated nature of the data and reinforces the importance of integrating all the results for a better interpretation.

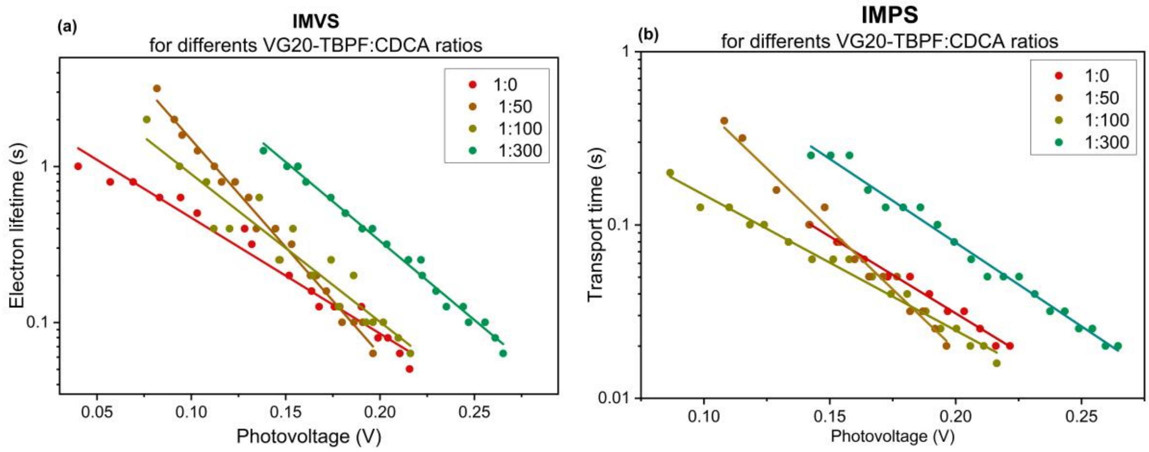

Figure 44. Electron lifetime (a) and transport time (b) as a function of photovoltage measured by IMVS/IMPS for VG20-TBPF-based DSSCs with different VG20-TBPF:CDCA ratios (1:0, 1:50, 1:100, and 1:300).

Despite these limitations, the results of the curves provide a more robust view of the trends observed. The slopes of the IMPS and IMVS curves highlight consistent behavior for samples with a higher concentration of CDCA, suggesting that these devices are less prone to recombination and have more efficient charge transport. The charge collection efficiency (η_{cc}), calculated based on lifetimes and transport times, follows this same trend, with slightly higher values for the 1:300 ratio. This reflects more effective charge collection before recombination processes occur.

Table 12. Electron lifetime (τe), transport time (τt), and charge collection efficiency (ηcc) for SubPc sensitizers in THF and ethanol (EtOH).

VG20-TBPF based DSSC			
VG20-TBPF:CDCA	τ_e (ms)	τ_t (ms)	ηcc
1:0	50.33	20.04	0.72
1:50	63.36	20.04	0.76
1:100	63.36	20.04	0.76
1:300	63.36	15.92	0.8

In summary, the results of the IMVS and IMPS analyses indicate that the presence of CDCA, particularly in the highest ratio tested, improves the transport dynamics and stability of electrons in the semiconductor. However, due to the proximity in the estimated values, it is prudent to consider that these differences are subtle and may be related to experimental variations or limitations inherent in measurement techniques. Thus, interpretation of the data should focus mainly on the general trends observed in the curves, which point to the positive role of CDCA in the performance of VG20-TBPF-based DSSCs.

4.1.4. Transmittance and AVT Analysis

The aggregation of dye molecules is a critical factor that can influence both the efficiency and aesthetics of DSSCs, especially in devices designed for transparent applications, such as solar cells integrated into windows or facades. To prevent the formation of aggregates, it is common to add disaggregating agents, such as chenodeoxycholic acid (CDCA), to dye solutions. CDCA acts by reducing the formation of H and J aggregates, promoting a more uniform distribution of the dye molecules on the surface of the semiconductor. However, while reducing aggregation, high concentrations of CDCA can also decrease the adsorbed dye load, reducing light absorption and affecting photovoltaic performance. This balance is especially important in solar cells intended for applications where transparency is essential. In this study, AVT values were measured on complete cells. This approach makes it possible to assess the final transparency of the device under conditions that are closer to the real thing. However, it is important to note that the cells used for these measurements were specifically designed to maximize transparency, using transparent electrodes and configurations optimized for aesthetics, and not to achieve the best photovoltaic efficiencies. This highlights the focus of the study on evaluating the potential of VG20-TBPF-based DSSCs for applications in transparent devices.

The AVT analysis shows a significant increase in transparency with increasing CDCA concentration. In the absence of CDCA (1:0 ratio), the AVT was around 33%, while at the highest concentration tested (1:300), the value increased to 57%. This reflects the expected role of CDCA as a disaggregating agent, promoting a reduction in the density of adsorbed dye and, consequently, in the coloration of the cell. The intermediate values for 1:50 and 1:100 (48% and 48%, respectively) confirm this trend towards greater transparency with increasing concentrations of CDCA.

Figure 45 shows the transmittance curve for the 1:300 sample, which obtained the highest AVT. The dotted line represents the average AVT value, while the continuous line shows the transmittance curve along the spectrum. The gray peak, representing the photopic response (indicating the average sensitivity of the human eye to visible light), makes it possible to correlate the transparency of the device with visual perception. The transmittance curve for 1:300 is well aligned with the photopic response, suggesting that this cell is highly promising for aesthetic applications, such as architectural integration.

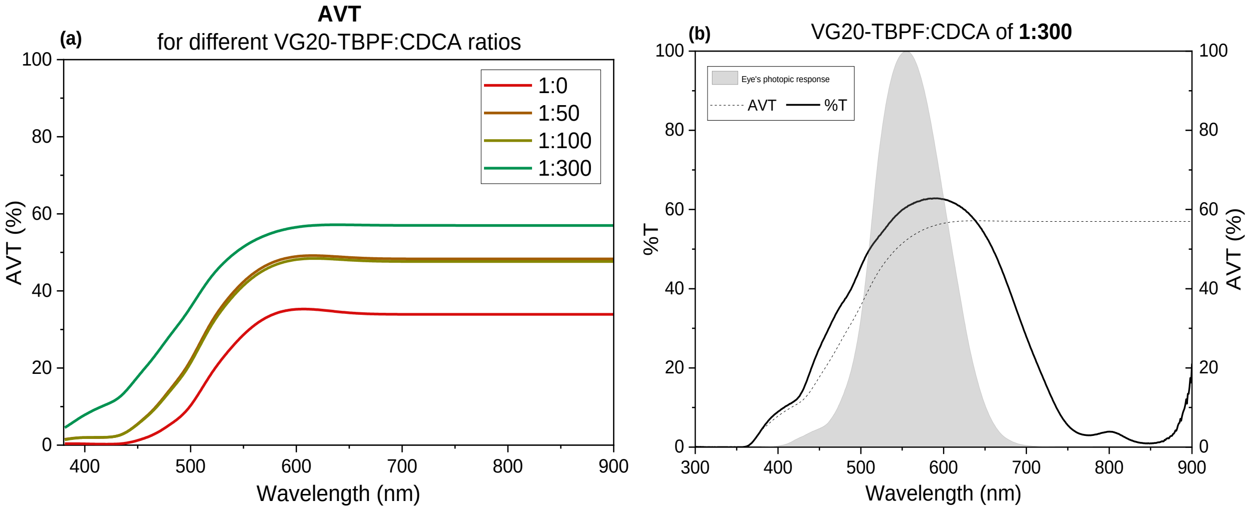

Figure 45. (a) Average Visible Transmittance (AVT) as a function of wavelength for VG20-TBPF-based DSSCs with different VG20-TBPF:CDCA ratios (1:0, 1:50, 1:100, and 1:300). (b) Overlaid AVT and transmittance for VG20-TBPF:CDCA at a 1:300 ratio together with eye's photopic response spectra.

Analysis of the results suggests that increasing the concentration of CDCA contributes to greater transparency, but it is important to note that this comes at the cost of lower dye loading in the semiconductor. Although the higher AVT in the 1:300 ratio is desirable for applications that demand high transparency, reducing the dye load can negatively impact the photovoltaic efficiency of these devices, as indicated by the lower density of adsorbed dye reported in the literature. This trade-off between transparency and efficiency should be considered when optimizing devices for different applications. In summary, the results highlight the essential role of CDCA in balancing the aggregate reduction and transparency of DSSCs. The 1:300 concentration proved particularly effective in maximizing AVT, making the device more suitable for applications that prioritize aesthetics and color neutrality. However, the devices still require adjustments to find a balance between transparency, efficiency and operational stability under real conditions.

4.2. *Developing a new manufacturing method for VG20-TBPF-based DSSC*

One of the main strategies for improving the performance of DSSCs is to optimize the thickness of the semiconductor layer, which plays a crucial role in electron transport dynamics and interaction with the dye. Thinner semiconductor layers can offer significant advantages for the electrochemical characteristics of solar cells. Firstly, reducing the thickness decreases the path that electrons need to take to reach the external circuit, thus reducing the resistive losses associated with charge transport. This can lead to an increase in charge collection efficiency and a reduction in recombination losses, since the electrons spend less time in the semiconductor. In addition, thinner layers can improve the transparency of the device, an especially important factor for applications in solar windows and building-integrated devices, where aesthetics is an essential requirement.

However, reducing the thickness also presents challenges. Thinner layers can decrease the amount of dye adsorbed on the semiconductor, reducing light absorption and, potentially, the current density generated. Therefore, optimizing the thickness of the semiconductor is a delicate balance between maintaining a layer thin enough to improve electron transport and thick enough to ensure good light absorption. This was the motivation for exploring a new manufacturing method that would make it possible to reduce the thickness of the semiconductor in a controlled manner, while maintaining the efficiency of the cell.

The new manufacturing method was based on the *spin coating* technique, which allows for the controlled and uniform deposition of thin layers of semiconductor. To do this, a solution containing TiO_2 paste (30 NR) and dry ethanol was prepared. The semiconductor was applied by depositing 60 μL of this solution onto the glass substrate, followed by a *spin coating* process at approximately 1000 rpm for 15 seconds. After each deposition, the film was dried on a plate heated to 200 °C for 2 minutes, ensuring adhesion and stability of the layer. This process was repeated to form films with different thicknesses, ranging from 1, 3, 6 and 9 layers, corresponding to estimated thicknesses of approximately 1 μm per layer. After forming the semiconductor layers, the photoanodes were sensitized using two different methods to apply the VG20-TBPF dye. In the first method, the photoanodes were immersed for 24 hours in a solution of VG20-TBPF (0.3 mM in DMSO/EtOH, 1:9) containing CDCA. This technique, called immersion deposition, is widely used and promotes uniform adsorption of the dye on the surface of the semiconductor. In the second method, the dye was applied via *spin coating*. To do this, four successive layers of 60 μL of the dye solution were deposited, using a speed of 1000 rpm for 30 seconds for each layer. Between each application, the layers were allowed to dry before the next deposition.

This new method was designed to evaluate the influence of reducing the thickness of the semiconductor layer and the method of applying the dye on the overall performance of the DSSCs. The *spin coating* technique was chosen due to its ability to produce homogeneous and well-controlled layers, allowing for a more accurate assessment of the relationship between thickness, electron transport and photovoltaic efficiency. The inclusion of an alternative sensitization method, such as *spin coating of* the dye, also aimed to explore its influence on dye adsorption and interaction with the semiconductor.

4.2.1. Photoanodes Transmittance analysis

One of the main challenges in developing DSSCs is to balance aesthetics and efficiency, especially for applications that require transparent devices such as solar windows or photovoltaic cells integrated into buildings. In the new manufacturing method explored, one of the objectives was to evaluate the transparency of the photoanodes after adding the VG20-TBPF dye, both by *dipping* and *spin coating*. This analysis makes it possible to verify that the semiconductor maintains good transparency after the different deposition processes, ensuring that the final device has the potential for aesthetic applications without compromising its functionality.

The maximum transmittance values (%T max) obtained are represented in the transmittance curves in Figure 46. In general, the results show that the photoanodes maintained relatively high transparency, indicating that the manufacturing method adopted promotes semiconductors and dye layers that allow light to pass through efficiently.

For the photoanodes produced by the *dipping* method, the maximum transmittance values increased with the number of layers, rising from 46% for 1 layer to 69% with 6 layers. This indicates that even with an increase in the amount of semiconductor deposited, the photoanodes remained highly transparent. This behavior can be attributed to the uniformity of the layers formed during the *dipping* process, which prevents excess dye and promotes homogeneous coverage. For the photoanodes manufactured using the *spin coating* method, the results show even greater transparency for 1 and 3 layers, with %T max values reaching 74%. However, for 6 layers, transparency decreased to 51%, suggesting that thicker layers applied by *spin coating* may interfere with the passage of light, possibly due to a higher density of semiconductor or a higher concentration of dye on the surface.

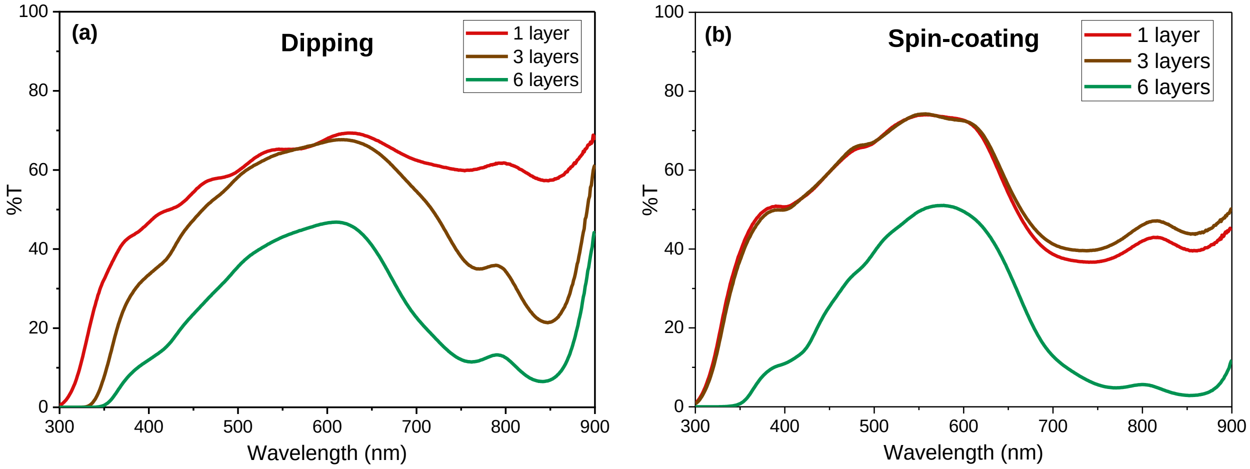

Figure 46. Transmittance (%T) as a function of wavelength for films prepared by (a) dipping and (b) spin-coating methods, with 1, 3, and 6 layers.

Analysis of the transmittance curves confirms that both methods maintain the transparency of the semiconductor at levels suitable for applications requiring aesthetic devices. The *spin coating* method, particularly for a smaller number of layers, proved to be effective in forming highly transparent photoanodes. On the other hand, the *dipping* method showed a more consistent performance in terms of transparency as the number of layers increased, which could be an advantage depending on the application. These results indicate that, regardless of the deposition method, the new fabrication process was able to generate photoanodes with high transparency. This reinforces the potential of the new method to combine photovoltaic efficiency and aesthetics and is especially promising for the development of DSSCs integrated into environments that prioritize visual neutrality and transparency.

4.2.2. Photovoltaic Performance Analysis

In the development of DSSCs using the new fabrication method, two types of deposition of the VG20-TBPF dye were explored: dipping and *spin coating*. Both methods were used to evaluate how the deposition of the dye influences the photovoltaic parameters and the overall performance of the devices. The electrical characterization of the cells was carried out in a solar simulator, and the main photovoltaic parameters are shown in Table 13.

The devices made with dip deposition showed extremely low efficiency values, 0.010% and 0.013% for 6 and 9 semiconductor layers, respectively. Despite this, the Voc values obtained, of 0.30 V and 0.28 V, are relatively good, considering the low overall efficiency. The short-circuit current density (Jsc), however, was extremely low, at 0.07 mA/cm² for 6 layers and 0.10 mA/cm² for 9 layers. These values indicate that the amount of dye adsorbed and/or the electron injection efficiency may be sub-optimal, compromising current generation.

On the other hand, the devices made using *spin coating* to apply the dye performed slightly better in terms of Jsc. For 6 and 9 layers, the Jsc values were 0.14 mA/cm^2 and 0.13 mA/cm^2, respectively. Although Voc was slightly lower than for dip-deposited cells (0.25 V and 0.24 V), the results indicate that the *spin coating* method favors higher current density. However, the fill factors (FF) for both methods remained low, between 39% and

44%, indicating that the devices present significant resistive losses or problems related to the interface between the materials.

The *J-V* curves of the fabricated (Figure 47) devices show that, although the general shape of the curves is within the expected range for DSSCs, the Jsc values are far below ideal, resulting in extremely low efficiencies. This suggests that although the fabrication method generated uniform layers, the amount of dye adsorbed and the interaction between the dye and the semiconductor were not sufficient to achieve good light capture and electron injection. These results indicate the need for adjustments in the semiconductor and dye deposition process, as well as in the formulation of the solutions used.

Although the efficiencies obtained are low, the V_{oc} values observed are relatively satisfactory. This suggests that the devices can generate reasonable charge separation but face significant losses during electron transport and collection. Limitations in performance can be attributed to factors such as low density of adsorbed dye, recombinations at the semiconductor-electrolyte interface or losses during charge transfer to the external circuit. The difference between the two dye deposition methods may be related to the uniformity and density of the dye layer formed. While immersion promotes uniform coverage along the semiconductor, *spin coating* allows greater control over deposition but can lead to a lower amount of dye adsorbed, especially when the number of semiconductor layers is reduced. In addition, the low overall efficiency of the devices may be an indication that the thinner semiconductor layers, although beneficial for electron transport, are not retaining enough dye to optimize light absorption.

In summary, the devices fabricated using the new method showed very low photovoltaic efficiencies, mainly due to the reduced J_{sc} values. However, the relatively high V_{oc} values indicate that the electrochemical potential of the devices is promising and can be optimized in future iterations. The exploration of new parameters, such as adjustments to the thickness of the semiconductor, the formulation of the dye and the control of the deposition conditions, will be crucial to improving the performance of these devices.

Table 13. Photovoltaic performance parameters of DSSCs prepared by dipping and spin-coating methods with 6 and 9 layers. The table includes open-circuit voltage (V_{OC}), short-circuit current density (J_{SC}), fill factor (FF), and efficiency (η).

Dipping				
Layers	V_{oc} (V)	J_{sc} (mA/cm^2)	FF (%)	η (%)
6	0.3	0.07	44	0.01
9	0.28	0.1	43	0.013
Spin-coating				
Layers	V_{oc} (V)	J_{sc} (mA/cm^2)	FF (%)	η (%)
6	0.25	0.14	41	0.015
9	0.24	0.13	39	0.013

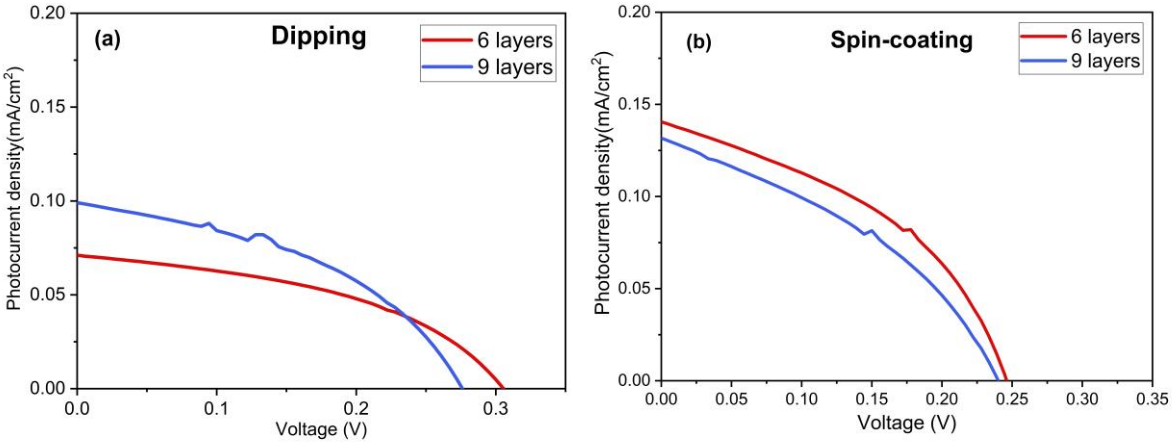

Figure 47. Evolution of J-V curves of DSSCs prepared with (a) dipping and (b) spin-coating methods for 6 and 9 layers.

4.3. Conclusion and Perspectives

This study demonstrated the successful fabrication of DSSCs using the VG20-TBPF dye by the traditional method, achieving satisfactory results in terms of photovoltaic efficiency. The fabricated cells performed well, with consistent current density (J_{SC}), open circuit voltage (V_{OC}) and efficiency (η) values, confirming the potential of VG20-TBPF as a promising dye for DSSCs. These results reinforce the viability of VG20-TBPF in traditional photovoltaic applications, especially when associated with the addition of CDCA, which contributed significantly to improving the efficiency of the devices.

Furthermore, the exploration of a new fabrication method, using thinner semiconductor layers applied via *spin coating* and different dye deposition strategies, has opened new possibilities for the development of more transparent and aesthetically pleasing DSSCs. Although the efficiency results for the cells fabricated by the new method were low, the high level of transparency observed in the photoanodes highlights the potential of this approach for specific applications, such as solar windows and building-integrated devices, where aesthetics play a key role.

Therefore, the study not only validated the efficiency of VG20-TBPF in the conventional method, but also established a promising basis for future optimizations in the new manufacturing method. Further adjustments to the formulation of the solutions, the control of layer thickness and the dye deposition strategy could lead to devices that combine high efficiency with transparency, broadening the possibilities for using DSSCs in a variety of applications. These results reinforce the importance of continuing to explore new approaches to integrating aesthetics and functionality in emerging photovoltaic technologies.

5. Chapter 3 References

[1] B. O'Regan and M. Grätzel, "A low-cost, high-efficiency solar cell based on dye-sensitized colloidal TiO2 films," *Nature*, vol. 353, no. 6346, pp. 737–740, Oct. 1991, doi: 10.1038/353737a0.

[2] E. Biyik *et al.*, "A key review of building integrated photovoltaic (BIPV) systems," *Engineering Science and Technology, an International Journal*, vol. 20, no. 3. Elsevier, pp. 833–858, Jun. 01, 2017, doi: 10.1016/j.jestch.2017.01.009.

[3] E. Franklin, V. Everett, A. Blakers, and K. Weber, "Sliver solar cells: High-efficiency, low-cost PV technology," *Adv. Optoelectron.*, vol. 2007, no. 1, p. 035383, Jan. 2007, doi: 10.1155/2007/35383.

[4] M. Biancardo *et al.*, "Characterization of microspherical semi-transparent solar cells and modules," *Sol. Energy*, vol. 81, no. 6, pp. 711–716, Jun. 2007, doi: 10.1016/j.solener.2006.10.009.

[5] K. Lee *et al.*, "Neutral-Colored Transparent Crystalline Silicon Photovoltaics," *Joule*, vol. 4, no. 1, pp. 235–246, Jan. 2020, doi: 10.1016/j.joule.2019.11.008.

[6] P. D. Sekaran and R. Marimuthu, "An Extensive Analysis of Dye-Sensitized Solar Cell (DSSC)," *Brazilian J. Phys.*, vol. 54, no. 1, pp. 1–10, Feb. 2024, doi: 10.1007/s13538-023-01375-w.

[7] S. Garcia Mayo, "Dye-Sensitized Solar Cells: the future of consumer electronics?," 2021, Accessed: Nov. 28, 2024. [Online]. Available: https://urn.kb.se/resolve?urn=urn:nbn:se:hig:diva-36993.

[8] Z. Yin *et al.*, "Graphene-Based materials for solar cell applications," *Advanced Energy Materials*, vol. 4, no. 1. John Wiley & Sons, Ltd, p. 1300574, Jan. 01, 2014, doi: 10.1002/aenm.201300574.

[9] Q. Huaulmé *et al.*, "Photochromic dye-sensitized solar cells with light-driven adjustable optical transmission and power conversion efficiency," *Nat. Energy*, vol. 5, no. 6, pp. 468–477, Jun. 2020, doi: 10.1038/s41560-020-0624-7.

[10] D. Joly *et al.*, "Metal-free organic sensitizers with narrow absorption in the visible for solar cells exceeding 10% efficiency," *Energy Environ. Sci.*, vol. 8, no. 7, pp.

2010–2018, Jul. 2015, doi: 10.1039/c5ee00444f.

[11] F. Grifoni *et al.*, “Toward Sustainable, Colorless, and Transparent Photovoltaics: State of the Art and Perspectives for the Development of Selective Near-Infrared Dye-Sensitized Solar Cells,” *Advanced Energy Materials*, vol. 11, no. 43. John Wiley & Sons, Ltd, p. 2101598, Nov. 01, 2021, doi: 10.1002/aenm.202101598.

[12] Y. Smortsova *et al.*, “Solvatochromic effects on a class of indoline derivatives organic photosensitizers: About the influence of hydrogen-bond acceptor and donor abilities parameters,” *J. Mol. Liq.*, vol. 245, pp. 76–84, Nov. 2017, doi: 10.1016/j.molliq.2017.06.052.

[13] N. Maity, P. Piatkowski, K. Polok, F. A. Miannay, and A. Idrissi, “Effect of the Mixture Composition of BmimBF4-Acetonitrile on the Excited-State Relaxation Dynamics of a Solar-Cell Dye D149: An Ultrafast Transient Absorption Study,” *J. Phys. Chem. C*, vol. 125, no. 32, pp. 17841–17852, Aug. 2021, doi: 10.1021/acs.jpcc.1c05008.

[14] D. Kuang, S. Uchida, R. Humphry-Baker, S. M. Zakeeruddin, and M. Grätzel, “Organic dye-sensitized ionic liquid based solar cells: Remarkable enhancement in performance through molecular design of indoline sensitizers,” *Angew. Chemie - Int. Ed.*, vol. 47, no. 10, pp. 1923–1927, Feb. 2008, doi: 10.1002/anie.200705225.

[15] Y. Smortsova, “Dye sensitized solar cells effciency improvement: optimization of the electrolyte using ionic liquids/molecular solvents mixture and study of the photodynamic properties of organic indolinic derivative dyes,” Universit_e de Lille, 2018.

[16] N. Maity, “Characterization of the polarity, reorientation dynamics and photophysics of indoline based solar cell dyes in ionic liquid-molecular solvent mixtures: steadystate UV-visible, EPR, time resolved fluorescence, femtosecond transient absorption and optical K,” Université de Lille, 2022.

[17] J. B. Prieto, F. L. Arbeloa, V. M. Martínez, T. A. López, and I. L. Arbeloa, “Photophysical properties of the pyrromethene 597 dye: Solvent effect,” *J. Phys. Chem. A*, vol. 108, no. 26, pp. 5503–5508, Jul. 2004, doi: 10.1021/JP0373898/ASSET/IMAGES/LARGE/JP0373898F00007.JPEG.

[18] P. W. Lohse *et al.*, “Ultrafast photoinduced relaxation dynamics of the indoline

dye D149 in organic solvents," *Phys. Chem. Chem. Phys.*, vol. 13, no. 43, pp. 19632–19640, Oct. 2011, doi: 10.1039/C1CP22429H.

[19] I. Benesperi, H. Michaels, and M. Freitag, "The researcher's guide to solid-state dye-sensitized solar cells," *Journal of Materials Chemistry C*, vol. 6, no. 44. Royal Society of Chemistry, pp. 11903–11942, Nov. 15, 2018, doi: 10.1039/c8tc03542c.

[20] S. V. Raksha, V. I. Kondrashin, E. A. Pecherskaya, and K. O. Nikolaev, "Functional Materials for Dye-sensitized Solar Cells," vol. 7, no. 4, p. 4062, 2015, Accessed: Jan. 31, 2023. [Online]. Available: https://essuir.sumdu.edu.ua/handle/123456789/44480.

[21] H. Iftikhar, G. G. Sonai, S. G. Hashmi, A. F. Nogueira, and P. D. Lund, "Progress on electrolytes development in dye-sensitized solar cells," *Materials*, vol. 12, no. 12. Multidisciplinary Digital Publishing Institute, p. 1998, Jun. 21, 2019, doi: 10.3390/ma12121998.

[22] M. K. Nazeeruddin *et al.*, "Combined experimental and DFT-TDDFT computational study of photoelectrochemical cell ruthenium sensitizers," in *Renewable Energy: Four Volume Set*, vol. 2–4, no. 48, American Chemical Society, 2018, pp. 227–251.

[23] P. Wang *et al.*, "Stable new sensitizer with improved light harvesting for nanocrystalline dye-sensitized solar cells," *Adv. Mater.*, vol. 16, no. 20, pp. 1806–1811, Oct. 2004, doi: 10.1002/adma.200400039.

[24] A. Yella *et al.*, "Porphyrin-sensitized solar cells with cobalt (II/III)-based redox electrolyte exceed 12 percent efficiency," *Science (80-.).*, vol. 334, no. 6056, pp. 629–634, Nov. 2011, doi: 10.1126/science.1209688.

[25] M. K. Nazeeruddin *et al.*, "Conversion of Light to Electricity by zyx cis-XzBis(zyxwv 2,2'-bipyridyl-4,4'-dicarboxylate)ruthenium(11) Charge-Transfer Sensitizers (X zyxw = C1-, Br-, I-, CN-, and SCN-) on Nanocrystalline Ti02 Electrodes," *J. Am. Chem. SOC. zyxw*, vol. 115, no. Ii, pp. 6382–6390, 1993.

[26] N. Papageorgiou *et al.*, "The Performance and Stability of Ambient Temperature Molten Salts for Solar Cell Applications," *J. Electrochem. Soc.*, vol. 143, no. 10, pp. 3099–3108, Oct. 1996, doi: 10.1149/1.1837171.

[27] L. A. Santa-Cruz *et al.*, "Effect of heterocyclic nitrogen ionic liquid additives on the rate of backreaction in DSSCS: An electrochemical characterization," *J. Sci. Adv. Mater. Devices*, vol. 6, no. 3, pp. 483–487, Sep. 2021, doi: 10.1016/J.JSAMD.2021.05.007.

[28] D. Kuang, S. Uchida, R. Humphry-Baker, S. M. Zakeeruddin, and M. Grätzel, "Organic Dye-Sensitized Ionic Liquid Based Solar Cells: Remarkable Enhancement in Performance through Molecular Design of Indoline Sensitizers," *Angew. Chemie*, vol. 120, no. 10, pp. 1949–1953, 2008, doi: 10.1002/ange.200705225.

[29] J. R. Reimers and L. E. Hall, "The solvation of acetonitrile," *J. Am. Chem. Soc.*, vol. 121, no. 15, pp. 3730–3744, 1999, doi: 10.1021/ja983878n.

[30] O. Quinet, B. Champagne, and V. Rodriguez, "Experimental and theoretical investigation of the Raman and hyper-Raman spectra of acetonitrile and its derivatives," *J. Chem. Phys.*, vol. 124, no. 24, p. 244312, 2006, doi: 10.1063/1.2208350.

[31] K. L. Rowlen1 and J. M. Harris, "Raman Spectroscopic Study of Solvation Structure in Acetonitrile/Water Mixtures," *Anal. Chem.*, vol. 63, no. 10, pp. 964–969, 1991, doi: 10.1021/ac00010a006.

[32] A. M. Brouwer, "Standards for photoluminescence quantum yield measurements in solution (IUPAC technical report)," *Pure Appl. Chem.*, vol. 83, no. 12, pp. 2213–2228, Aug. 2011, doi: 10.1351/PAC-REP-10-09-31/MACHINEREADABLECITATION/RIS.

[33] M. Fakis, P. Hrobárik, E. Stathatos, V. Giannetas, and P. Persephonis, "A time resolved fluorescence and quantum chemical study of the solar cell sensitizer D149," *Dye. Pigment.*, vol. 96, no. 1, pp. 304–312, Jan. 2013, doi: 10.1016/J.DYEPIG.2012.07.025.

[34] J. C. Del Valle and J. Catalán, "Kasha's rule: A reappraisal," *Phys. Chem. Chem. Phys.*, vol. 21, no. 19, pp. 10061–10069, 2019, doi: 10.1039/c9cp00739c.

[35] Y. Zhang, Y. Duan, and T. Wang, "Excited-state hydrogen-bonding dynamics of camphorsulfonic acid doped polyaniline: A theoretical study," *Phys. Chem. Chem. Phys.*, vol. 16, no. 47, pp. 26261–26265, Nov. 2014, doi: 10.1039/c4cp04267k.

[36] N. Sharma, S. K. Jain, and R. C. Rastogi, “Excited-state dipole moments of indoles using solvatochromic shift methods: An experimental and theoretical study,” *Bull. Chem. Soc. Jpn.*, vol. 76, no. 9, pp. 1741–1746, 2003, doi: 10.1246/bcsj.76.1741.

[37] T. Le Bahers, T. Pauporté, G. Scalmani, C. Adamo, and I. Ciofini, “A TD-DFT investigation of ground and excited state properties in indoline dyes used for dye-sensitized solar cells,” *Phys. Chem. Chem. Phys.*, vol. 11, no. 47, pp. 11276–11284, 2009, doi: 10.1039/b914626a.

[38] C. Wohlfahrt, “Static Dielectric Constants of Pure Liquids and Binary Mixtures,” in *Landolt-Börnstein – Group IV Physical Chemistry*, O. Madelung, Ed. 2002.

[39] C. Albrecht, “Joseph R. Lakowicz: Principles of fluorescence spectroscopy, 3rd Edition,” *Anal. Bioanal. Chem. 2007 3905*, vol. 390, no. 5, pp. 1223–1224, Jan. 2008, doi: 10.1007/S00216-007-1822-X.

[40] A. M. El-Zohry and B. Zietz, “Concentration and solvent effects on the excited state dynamics of the solar cell dye D149: The special role of protons,” *J. Phys. Chem. C*, vol. 117, no. 13, pp. 6544–6553, Apr. 2013, doi: 10.1021/jp400782g.

[41] A. M. El-Zohry and B. Zietz, “Electron Dynamics in Dye-Sensitized Solar Cells Influenced by Dye-Electrolyte Complexation,” *J. Phys. Chem. C*, vol. 124, no. 30, pp. 16300–16307, Jul. 2020, doi: 10.1021/acs.jpcc.0c03436.

[42] N. Boens *et al.*, “Fluorescence lifetime standards for time and frequency domain fluorescence spectroscopy,” *Anal. Chem.*, vol. 79, no. 5, pp. 2137–2149, Mar. 2007, doi: 10.1021/ac062160k.

[43] PicoQuant, *FluoFit: User’s Manual and Technical Data*, Version 4. .

[44] A. M. El-Zohry, D. Roca-Sanjuán, and B. Zietz, “Ultrafast twisting of the indoline donor unit utilized in solar cell dyes: Experimental and theoretical studies,” *J. Phys. Chem. C*, vol. 119, no. 5, pp. 2249–2259, Feb. 2015, doi: 10.1021/JP505649S/SUPPL_FILE/JP505649S_SI_001.PDF.

[45] A. El-Zohry, A. Orthaber, and B. Zietz, “Isomerization and aggregation of the solar cell dye D149,” *J. Phys. Chem. C*, vol. 116, no. 50, pp. 26144–26153, Dec. 2012, doi: 10.1021/jp306636w.

[46] A. M. El-Zohry, S. Agrawal, F. De Angelis, M. Pastore, and B. Zietz, “Critical

Role of Protons for Emission Quenching of Indoline Dyes in Solution and on Semiconductor Surfaces," *J. Phys. Chem. C*, vol. 124, no. 39, pp. 21346–21356, Oct. 2020, doi: 10.1021/acs.jpcc.0c07099.

[47] J. Sobuš, J. Karolczak, D. Komar, J. A. Anta, and M. Ziółek, "Transient states and the role of excited state self-quenching of indoline dyes in complete dye-sensitized solar cells," *Dye. Pigment.*, vol. 113, pp. 692–701, Feb. 2015, doi: 10.1016/j.dyepig.2014.10.008.

[48] R. Berera, R. van Grondelle, and J. T. M. Kennis, "Ultrafast transient absorption spectroscopy: Principles and application to photosynthetic systems," *Photosynthesis Research*, vol. 101, no. 2–3. Springer, pp. 105–118, Sep. 04, 2009, doi: 10.1007/s11120-009-9454-y.

[49] A. Maciejewski *et al.*, "Transient absorption experimental set-up with femtosecond time resolution. Femto- and picosecond study of DCM molecule in cyclohexane and methanol solution," in *Journal of Molecular Structure*, Nov. 2000, vol. 555, no. 1–3, pp. 1–13, doi: 10.1016/S0022-2860(00)00582-2.

[50] J. E. Ikpesu, S. E. Iyuke, M. Daramola, and A. O. Okewale, "Synthesis of improved dye-sensitized solar cell for renewable energy power generation," *Solar Energy*, vol. 206. Pergamon, pp. 918–934, Aug. 01, 2020, doi: 10.1016/j.solener.2020.05.002.

[51] N. I. A. Shukor *et al.*, "A Green Approach to Natural Dyes in Dye-Sensitized Solar Cells," *Sensors (Basel).*, vol. 23, no. 20, p. 8412, Oct. 2023, doi: 10.3390/s23208412.

[52] D. Javiya *et al.*, "Studies and comparison of natural dye-sensitized solar cells and thin-film solar cells," in *Materials Today: Proceedings*, Jan. 2023, vol. 73, pp. 545–549, doi: 10.1016/j.matpr.2022.10.222.

[53] C. L. Lee, W. H. Lee, and C. H. Yang, "High efficiency of dye-sensitized solar cells based on ruthenium and metal-free dyes," *Int. J. Photoenergy*, vol. 2013, no. 1, p. 250397, Jan. 2013, doi: 10.1155/2013/250397.

[54] S. Rahman *et al.*, "Research on dye sensitized solar cells: recent advancement toward the various constituents of dye sensitized solar cells for efficiency enhancement and future prospects," *RSC Advances*, vol. 13, no. 28. Royal Society

of Chemistry, pp. 19508–19529, Jun. 28, 2023, doi: 10.1039/d3ra00903c.

[55] B. S. Arslan *et al.*, “Optimization of fabrication parameters for efficient dye-sensitized solar cells based on dyes containing benzothiadiazole, indoline, and their co-sensitization,” *Electrochim. Acta*, vol. 458, p. 142523, Aug. 2023, doi: 10.1016/j.electacta.2023.142523.

[56] L. J. G. W. van Wilderen, C. N. Lincoln, and J. J. van Thor, “Modelling Multi-Pulse Population Dynamics from Ultrafast Spectroscopy,” *PLoS One*, vol. 6, no. 3, p. e17373, 2011, doi: 10.1371/JOURNAL.PONE.0017373.

[57] G. Nass Kovacs *et al.*, “Three-dimensional view of ultrafast dynamics in photoexcited bacteriorhodopsin,” *Nat. Commun. 2019 101*, vol. 10, no. 1, pp. 1–17, Jul. 2019, doi: 10.1038/s41467-019-10758-0.

[58] T. D. Green and K. L. Knappenberger, “Relaxation dynamics of Au25L18 nanoclusters studied by femtosecond time-resolved near infrared transient absorption spectroscopy,” *Nanoscale*, vol. 4, no. 14, pp. 4111–4118, Jun. 2012, doi: 10.1039/c2nr31080e.

[59] M. Fakis, E. Stathatos, G. Tsigaridas, V. Giannetas, and P. Persephonis, “Femtosecond decay and electron transfer dynamics of the organic sensitizer d149 and photovoltaic performance in quasi-solid-state dye-sensitized solar cells,” *J. Phys. Chem. C*, vol. 115, no. 27, pp. 13429–13437, Jul. 2011, doi: 10.1021/jp201143n.

[60] I. H. M. Van Stokkum, D. S. Larsen, and R. Van Grondelle, “Global and target analysis of time-resolved spectra,” *Biochimica et Biophysica Acta - Bioenergetics*, vol. 1657, no. 2–3. Elsevier, pp. 82–104, Jul. 09, 2004, doi: 10.1016/j.bbabio.2004.04.011.

[61] M. Ziólek, M. Lorenc, and R. Naskrecki, “Determination of the temporal response function in femtosecond pump-probe systems,” *Appl. Phys. B Lasers Opt.*, vol. 72, no. 7, pp. 843–847, 2001, doi: 10.1007/S003400100587/METRICS.

[62] J. S. Beckwith, C. A. Rumble, and E. Vauthey, “Data analysis in transient electronic spectroscopy–an experimentalist’s view,” *International Reviews in Physical Chemistry*, vol. 39, no. 2. Taylor & Francis, pp. 135–216, Apr. 02, 2020, doi: 10.1080/0144235X.2020.1757942.

[63] S. Ito *et al.*, “High-conversion-efficiency organic dye-sensitized solar cells with a novel indoline dye,” *Chem. Commun.*, no. 41, pp. 5194–5196, 2008, doi: 10.1039/b809093a.

[64] E. Rohwer *et al.*, “Ultrafast Photodynamics of the Indoline Dye D149 Adsorbed to Porous ZnO in Dye-Sensitized Solar Cells,” *ChemPhysChem*, vol. 14, no. 1, pp. 132–139, Jan. 2013, doi: 10.1002/CPHC.201200715.

[65] V. Novelli, N. Barbero, C. Barolo, G. Viscardi, M. Sliwa, and F. Sauvage, “Electrolyte containing lithium cation in squaraine-sensitized solar cells: Interactions and consequences for performance and charge transfer dynamics,” *Phys. Chem. Chem. Phys.*, vol. 19, no. 40, pp. 27670–27681, Oct. 2017, doi: 10.1039/c7cp04340f.

[66] S. Singh, Z. H. Khan, M. B. Khan, P. Kumar, and P. Kumar, “Quantum dots-sensitized solar cells: a review on strategic developments,” *Bulletin of Materials Science*, vol. 45, no. 2. Springer, pp. 1–13, Jun. 01, 2022, doi: 10.1007/s12034-022-02662-z.

[67] F. Matteocci *et al.*, “Wide bandgap halide perovskite absorbers for semi-transparent photovoltaics: From theoretical design to modules,” *Nano Energy*, vol. 101, p. 107560, Oct. 2022, doi: 10.1016/j.nanoen.2022.107560.

[68] W. Naim *et al.*, “Transparent and Colorless Dye-Sensitized Solar Cells Exceeding 75% Average Visible Transmittance,” vol. 15, p. 59, 2023, doi: 10.1021/jacsau.1c00045.

[69] A. Ebenezer Anitha and M. Dotter, “A Review on Liquid Electrolyte Stability Issues for Commercialization of Dye-Sensitized Solar Cells (DSSC),” *Energies*, vol. 16, no. 13. Multidisciplinary Digital Publishing Institute, p. 5129, Jul. 03, 2023, doi: 10.3390/en16135129.

[70] A. Agrawal, S. A. Siddiqui, A. Soni, and G. D. Sharma, “Advancements, frontiers and analysis of metal oxide semiconductor, dye, electrolyte and counter electrode of dye sensitized solar cell,” *Solar Energy*, vol. 233. Pergamon, pp. 378–407, Feb. 01, 2022, doi: 10.1016/j.solener.2022.01.027.

[71] B. K. Korir, J. K. Kibet, and S. M. Ngari, “A review on the current status of dye-sensitized solar cells: Toward sustainable energy,” *Energy Science and*

Engineering, vol. 12, no. 8. John Wiley & Sons, Ltd, pp. 3188–3226, Aug. 01, 2024, doi: 10.1002/ese3.1815.

[72] M. Grätzel, "Dye-sensitized solar cells," *J. Photochem. Photobiol. C Photochem. Rev.*, vol. 4, no. 2, pp. 145–153, Oct. 2003, doi: 10.1016/S1389-5567(03)00026-1.

[73] J. Wu *et al.*, "Counter electrodes in dye-sensitized solar cells," *Chemical Society Reviews*, vol. 46, no. 19. Royal Society of Chemistry, pp. 5975–6023, Oct. 02, 2017, doi: 10.1039/c6cs00752j.

[74] G. Richhariya, A. Kumar, A. K. Shukla, K. N. Shukla, and B. C. Meikap, "Effect of Different Counter Electrodes on Power Conversion Efficiency of DSSCs," *Journal of Electronic Materials*, vol. 52, no. 1. Springer, pp. 60–71, Jan. 01, 2023, doi: 10.1007/s11664-022-09973-1.

[75] N. A. Karim, U. Mehmood, H. F. Zahid, and T. Asif, "Nanostructured photoanode and counter electrode materials for efficient Dye-Sensitized Solar Cells (DSSCs)," *Solar Energy*, vol. 185. Pergamon, pp. 165–188, Jun. 01, 2019, doi: 10.1016/j.solener.2019.04.057.

[76] C. I. Oprea *et al.*, "Role of energy level alignment in solar cells sensitized with a metal-free organic dye: A combined experimental and theoretical approach," *Phys. Status Solidi Appl. Mater. Sci.*, vol. 208, no. 10, pp. 2467–2477, 2011, doi: 10.1002/pssa.201127083.

[77] J. Lungu *et al.*, "Heterocyclic azodyes as pigments for dye sensitized solar cells - A combined experimental and theoretical study," *J. Optoelectron. Adv. Mater.*, vol. 12, no. 9, pp. 1969–1975, 2010.

[78] L. Zhang and J. M. Cole, "Dye aggregation in dye-sensitized solar cells," *J. Mater. Chem. A*, vol. 5, no. 37, pp. 19541–19559, Sep. 2017, doi: 10.1039/C7TA05632J.

[79] F. Xu, T. T. Testoff, L. Wang, and X. Zhou, "Cause, Regulation and Utilization of Dye Aggregation in Dye-Sensitized Solar Cells," *Mol. 2020, Vol. 25, Page 4478*, vol. 25, no. 19, p. 4478, Sep. 2020, doi: 10.3390/MOLECULES25194478.

[80] A. F. Buene, D. M. Almenningen, A. Hagfeldt, O. R. Gautun, and B. H. Hoff, "First Report of Chenodeoxycholic Acid–Substituted Dyes Improving the Dye Monolayer Quality in Dye-Sensitized Solar Cells," *Sol. RRL*, vol. 4, no. 4, p.

1900569, Apr. 2020, doi: 10.1002/solr.201900569.

[81] X. Jiang, T. Marinado, E. Gabrielsson, D. P. Hagberg, L. Sun, and A. Hagfeldt, “Structural Modification of organic dyes for efficient coadsorbent-free dye-sensitized solar cells,” *J. Phys. Chem. C*, vol. 114, no. 6, pp. 2799–2805, Feb. 2010, doi: 10.1021/JP908552T/SUPPL_FILE/JP908552T_SI_005.TIF.

[82] P. Boyce, N. Eklund, S. Mangum, C. Saalfield, and L. Tang, “Minimum acceptable transmittance of glazing,” *http://dx.doi.org/10.1177/14771535950270030201*, vol. 27, no. 3, pp. 145–152, Sep. 1995, doi: 10.1177/14771535950270030201.

[83] N. Kutlu, “Investigation of electrical values of low-efficiency dye-sensitized solar cells (DSSCs),” *Energy*, vol. 199, p. 117222, May 2020, doi: 10.1016/j.energy.2020.117222.

[84] S. Sarker, H. W. Seo, and D. M. Kim, “Calculating current density-voltage curves of dye-sensitized solar cells: A straight-forward approach,” *J. Power Sources*, vol. 248, pp. 739–744, Feb. 2014, doi: 10.1016/j.jpowsour.2013.09.101.

[85] M. E. Ragoussi, M. Ince, and T. Torres, “Recent Advances in Phthalocyanine-Based Sensitizers for Dye-Sensitized Solar Cells,” *European J. Org. Chem.*, vol. 2013, no. 29, pp. 6475–6489, Oct. 2013, doi: 10.1002/EJOC.201301009.

[86] M.-E. Ragoussi *et al.*, “Carboxyethynyl Anchoring Ligands: A Means to Improving the Efficiency of Phthalocyanine-Sensitized Solar Cells,” *Angew. Chemie*, vol. 124, no. 18, pp. 4451–4454, Apr. 2012, doi: 10.1002/ANGE.201108963.

[87] M. Kimura *et al.*, “Molecular Design Rule of Phthalocyanine Dyes for Highly Efficient Near-IR Performance in Dye-Sensitized Solar Cells,” *Chem. – A Eur. J.*, vol. 19, no. 23, pp. 7496–7502, Jun. 2013, doi: 10.1002/CHEM.201300716.

[88] M. Ince *et al.*, “Peripherally and axially carboxylic acid substituted subphthalocyanines for dye-sensitized solar cells,” *Chem. - A Eur. J.*, vol. 20, no. 7, pp. 2016–2021, Feb. 2014, doi: 10.1002/CHEM.201303639.

[89] B. Verreet *et al.*, “A 4% Efficient Organic Solar Cell Using a Fluorinated Fused Subphthalocyanine Dimer as an Electron Acceptor,” *Adv. Energy Mater.*, vol. 1, no. 4, pp. 565–568, Jul. 2011, doi: 10.1002/AENM.201100137.

[90] H. Gotfredsen *et al.*, “Donor−Acceptor-Functionalized Subphthalocyanines for Dye-Sensitized Solar Cells,” *ChemPhotoChem*, vol. 2, no. 11, pp. 976–985, Nov. 2018, doi: 10.1002/CPTC.201800135.

[91] W. NAIM, “A novel approach of selective near-IR dye-sensitized solar cells as colorless and transparent photovoltaics : aesthetic evaluation and performance optimization,” Université de Picardie Jules Verne, 2022.

Final Conclusions

This thesis investigates the photophysical properties and efficacy of dye-sensitized solar cells (DSSCs), focusing primarily on transient absorption spectroscopy (TAS) as a crucial analytical instrument. I examined the behavior of the D205 dye in basic solvent combinations, uncovering dynamics that closely mirror those found in ionic liquid environments, thereby elucidating its excited-state processes. I also contributed to the creation of a software application for analyzing TAS data, facilitating the full analysis of dye solutions and DSSC devices. In addition to these foundational investigations, I assessed the performance of dye-sensitized solar cells (DSSCs) utilizing innovative dye systems, such as SubPc derivatives and VG20-TBPF, highlighting their potential for enhanced efficiency and aesthetic diversity. Chapter 2 connects the lessons from dye behavior in solution (Chapter 1) and DSSC performance (Chapter 3) by introducing the TAS-focused program. This tool was developed to analyze TAS data in both solution and device contexts, offering a cohesive framework for comprehending the interaction between molecule photophysics and device-level performance — a central emphasis of this thesis.

In Chapter 1, the photophysics of the D205 dye were studied in acetonitrile-butanol mixtures, demonstrating how solvent composition profoundly influences its properties. Increasing butanol content induced a 7 nm redshift in the absorption maximum and a 17 nm blueshift in the fluorescence maximum, accompanied by reductions in the Stokes shift and quantum yield, the latter dropping from 0.045 in acetonitrile to near zero in protic environments. These changes underscore the dominance of non-radiative deactivation mechanisms. Moreover, the relaxation times τ1 and τfluo, assessed via transient absorption spectroscopy (TAS) and time-correlated single photon counting (TCSPC), exhibited a transition from 0.15 ns in polar solvents to 1.3 ns in less polar environments, underscoring the influence of polarity and hydrogen bonding on the relaxation dynamics of D205's excited state. The findings indicate that solvent mixes, such as ionic liquids, considerably influence dye efficacy by modifying the equilibrium between radiative and non-radiative mechanisms.

This thesis incorporates transient absorption spectroscopy (TAS) as a fundamental analytical technique, with Chapter 2 detailing the creation of a Python-based software toolkit intended for the precise processing of femtosecond TAS data. The software tackles critical issues in the analysis of rapid photoinduced processes, such as group velocity dispersion (GVD) correction, by integrating mathematical models, including the Sellmeier equation and a GVD-adjusted Gaussian. These developments facilitate the accurate treatment of transitory data from dyes and dye-sensitized solar cell (DSSC) devices. The software proficiently processed pump-probe data for D205 in different solvents, revealing that the photophysical activity of D205 in ionic liquids closely resembles its behavior in organic solvents. This discovery offers a cohesive comprehension of D205 dynamics in many conditions, highlighting the reliability of the TAS software for molecular and device-level analyses. This chapter facilitates comprehensive modeling of ultrafast processes, integrating computational and experimental approaches to create a framework for examining dye photophysics and enhancing DSSC performance.

This thesis examined the efficacy of DSSCs constructed using the VG20-TBPF dye, confirming its potential as a viable sensitizer for conventional photovoltaic applications. Employing the traditional fabrication technique, DSSCs demonstrated reliable outcomes in photovoltaic efficiency, including stable current density (J_{SC}), open-circuit voltage (V_{OC}), and overall efficiency (η), especially when combined with the additive CDCA, which markedly improved device performance. A novel fabrication approach utilizing thinner semiconductor layers by spin coating and alternative dye deposition techniques was investigated. Despite their diminished efficiency, these cells demonstrated exceptional transparency in the photoanodes, highlighting their potential for applications where aesthetics, such as transparency and visual integration, are essential—such as solar windows and building-integrated photovoltaics (BIPVs). The study confirmed VG20-TBPF's potential in conventional DSSC designs and laid the groundwork for optimizing the novel fabrication method, necessitating further research to enhance layer thickness, dye deposition techniques, and solution formulations to produce devices that achieve a balance between transparency and high efficiency. These findings underscore the significance of merging aesthetics with functionality in the advancement of solar systems.

Annex Chapter 1

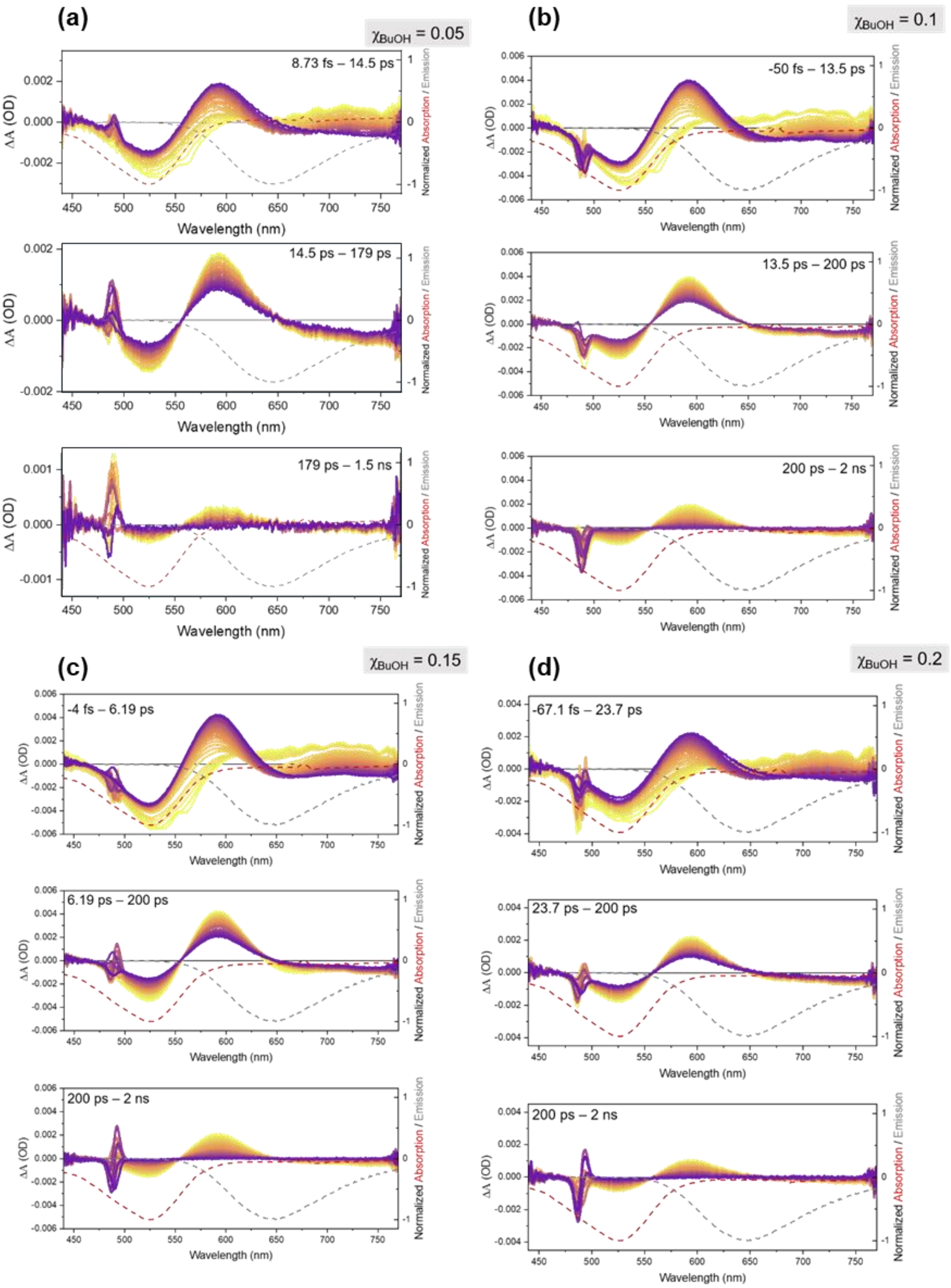

Figure A 1. D205 in a mixture ACN-BuOH with BuOH molar fraction of 0.05 (a), 0.1 (b), 0.15 (c) and 0.2 (d). Dashed lines represent steady-state absorption and emissio

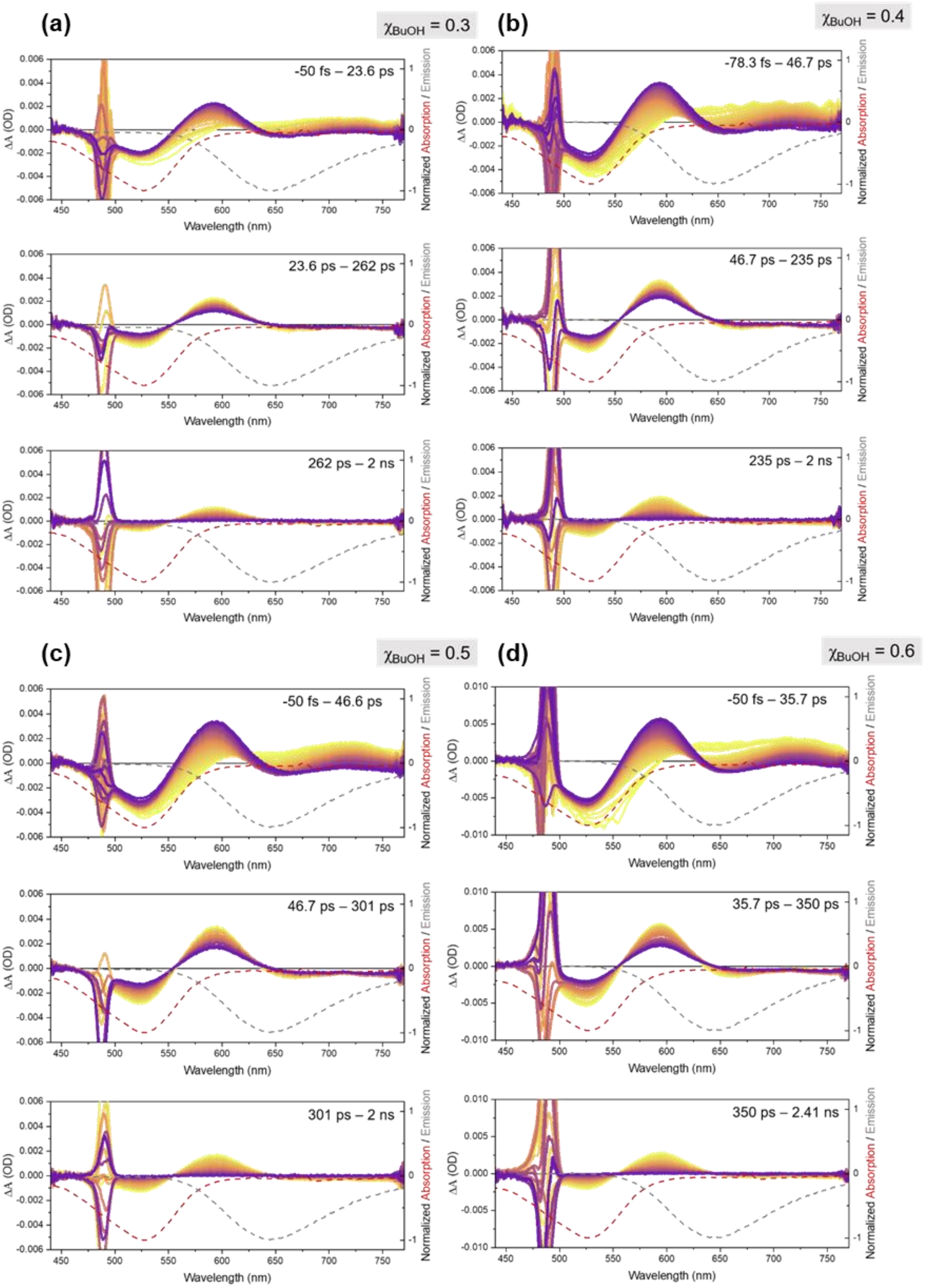

Figure A 2. D205 in a mixture ACN-BuOH with BuOH molar fraction of 0.3 (a), 0.4 (b), 0.5 (c) and 0.6 (d). Dashed lines represent steady-state absorption and emission.

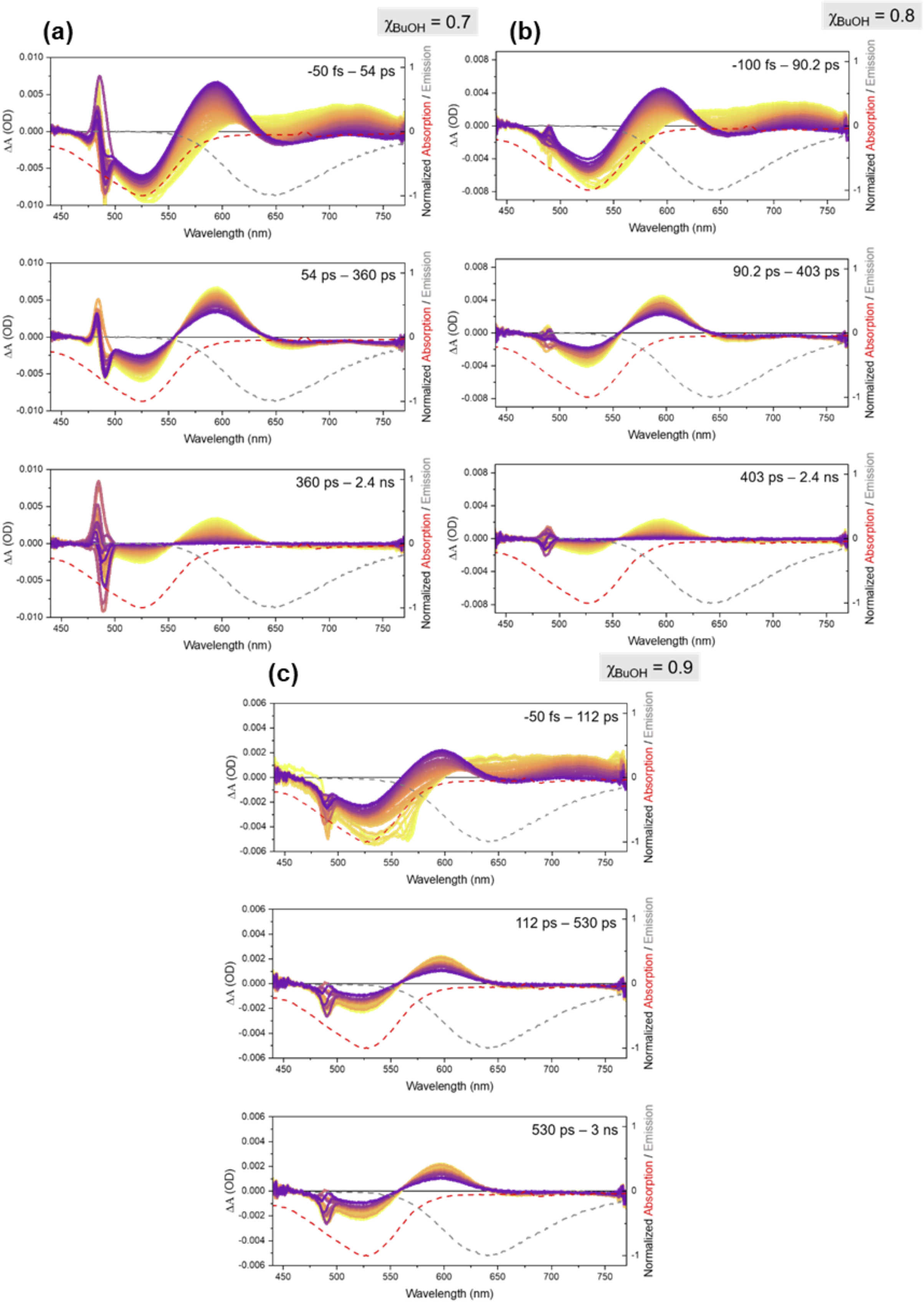

Figure A 3. D205 in a mixture ACN-BuOH with BuOH molar fraction of 0.7 (a), 0.8 (b) and 0.9 (c). Dashed lines represent steady-state absorption and emission.

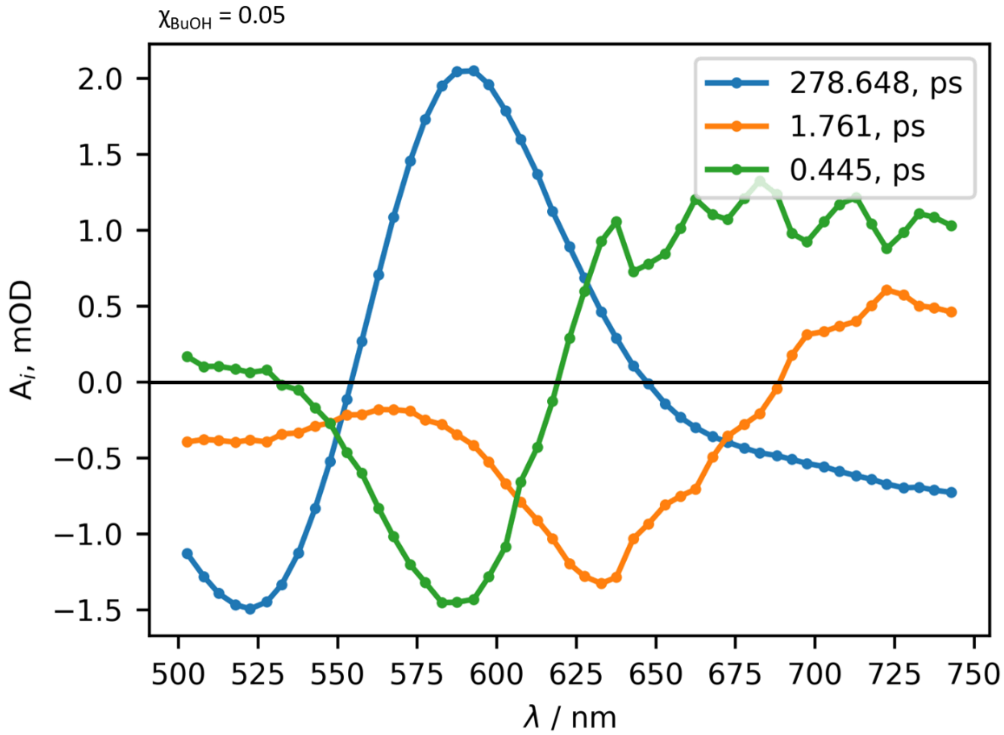

Figure A 4. Decay-associated spectra of D205 in a mixture ACN/BuOH with χBuOH = 0.05. Dashed lines represent steady-state absorption and emission.

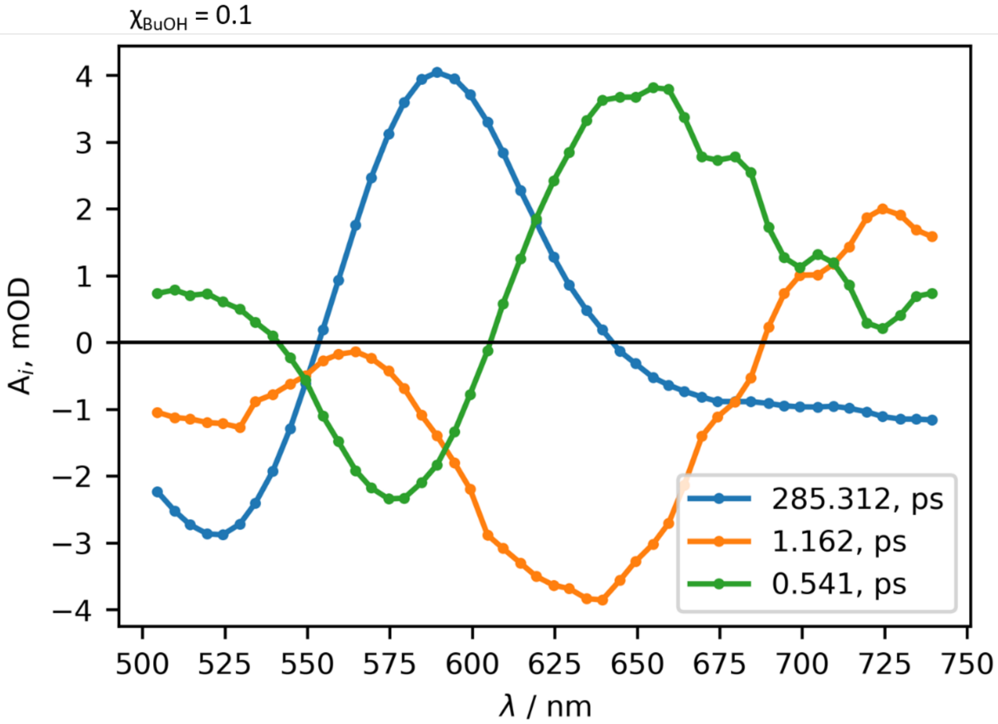

Figure A 5. Decay-associated spectra of D205 in a mixture ACN/BuOH with χBuOH = 0.1. Dashed lines represent steady-state absorption and emission.

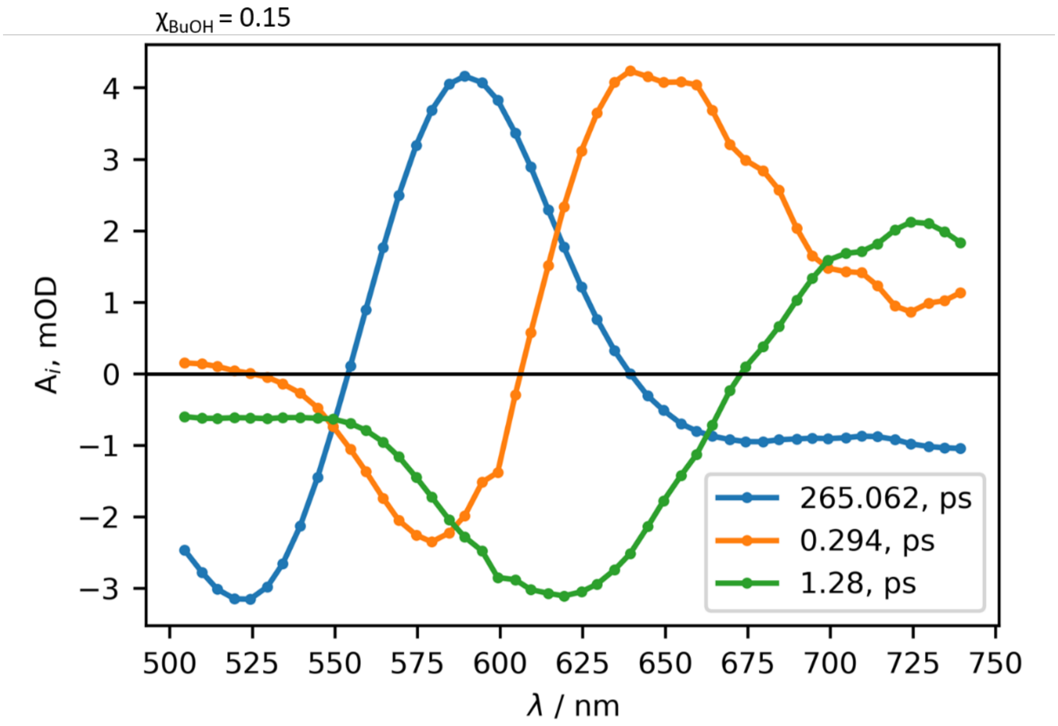

Figure A 6. Decay-associated spectra of D205 in a mixture ACN/BuOH with χBuOH = 0.15. Dashed lines represent steady-state absorption and emission.

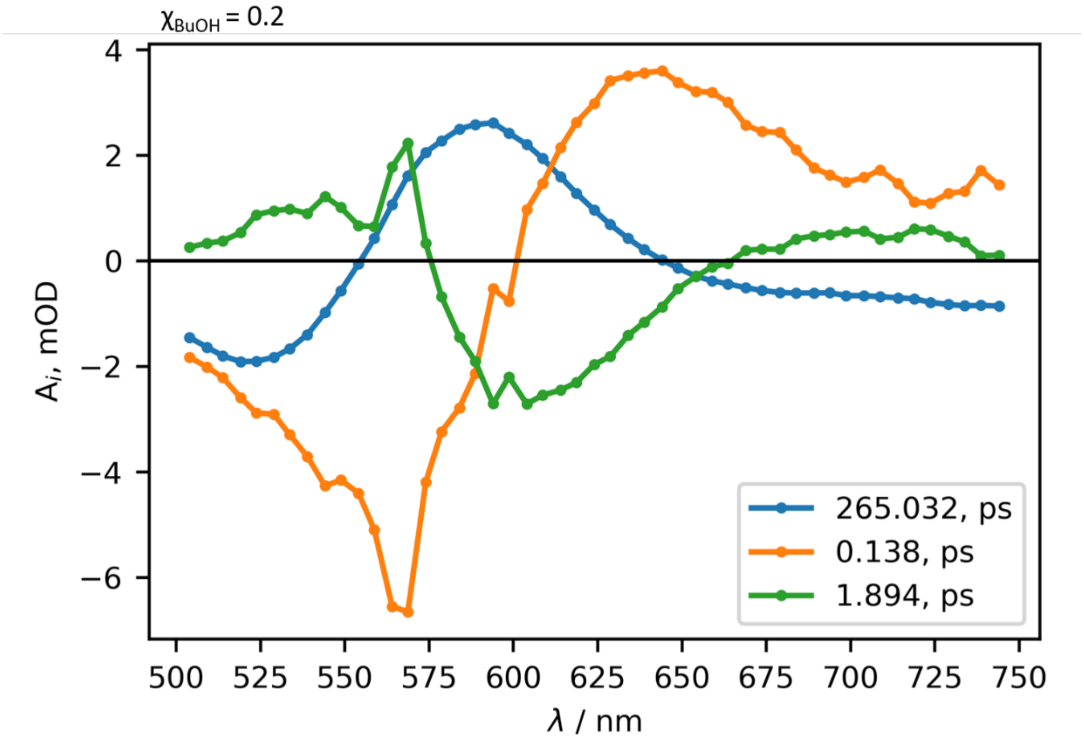

Figure A 7. Decay-associated spectra of D205 in a mixture ACN/BuOH with χBuOH = 0.2. Dashed lines represent steady-state absorption and emission.

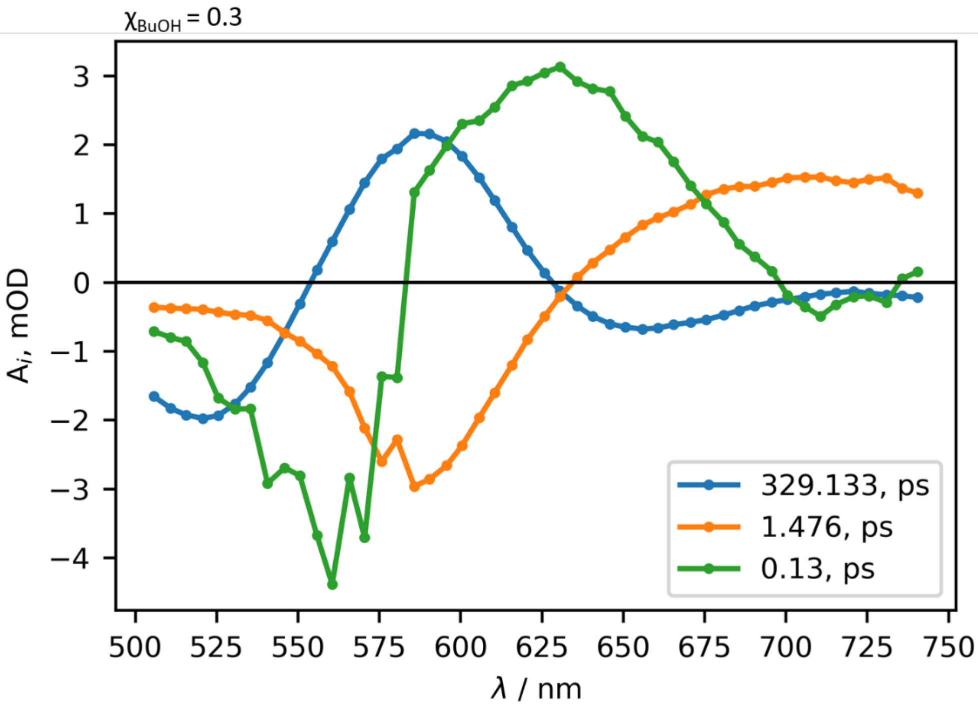

Figure A 8. Decay-associated spectra of D205 in a mixture ACN/BuOH with χBuOH = 0.3. Dashed lines represent steady-state absorption and emission.

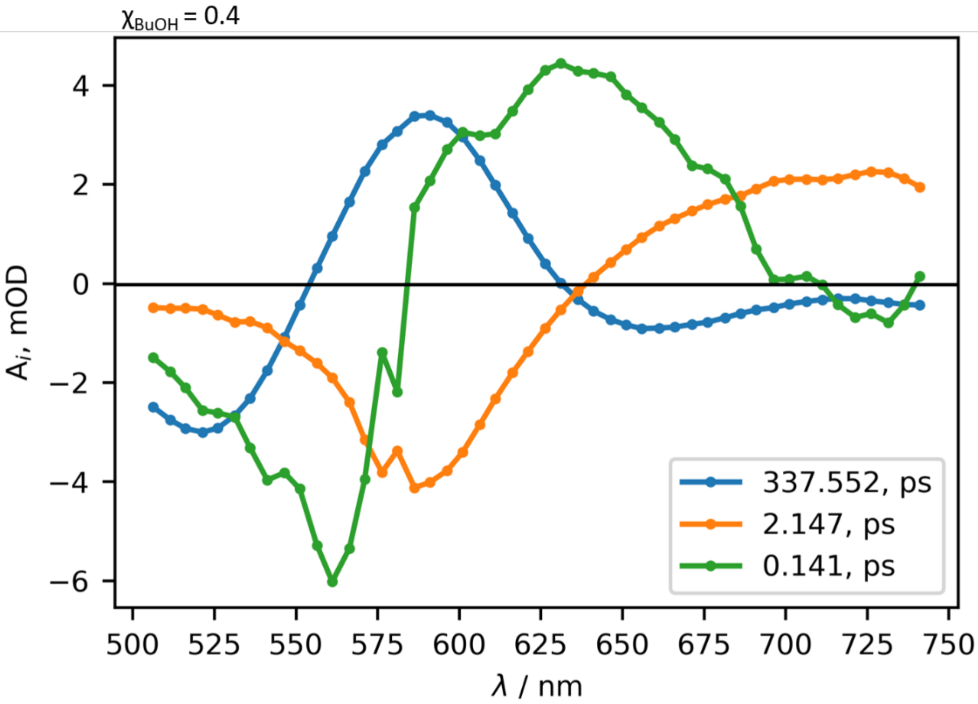

Figure A 9. Decay-associated spectra of D205 in a mixture ACN/BuOH with χBuOH = 0.4. Dashed lines represent steady-state absorption and emission.

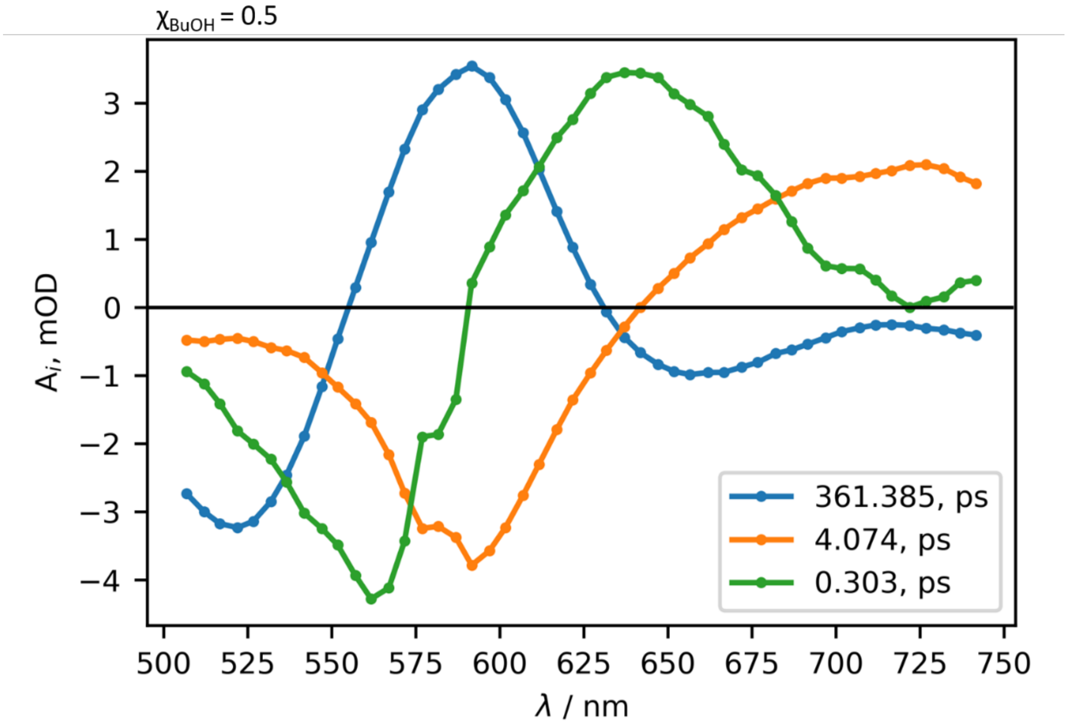

Figure A 10. Decay-associated spectra of D205 in a mixture ACN/BuOH with χBuOH = 0.5. Dashed lines represent steady-state absorption and emission.

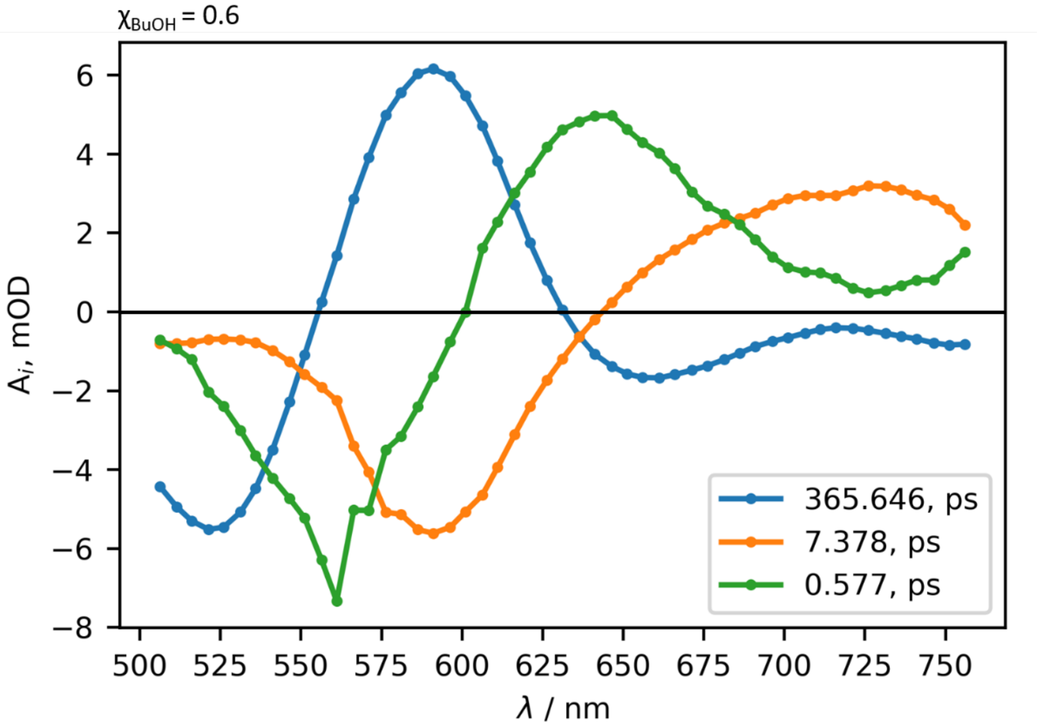

Figure A 11. Decay-associated spectra of D205 in a mixture ACN/BuOH with χBuOH = 0.6. Dashed lines represent steady-state absorption and emission.

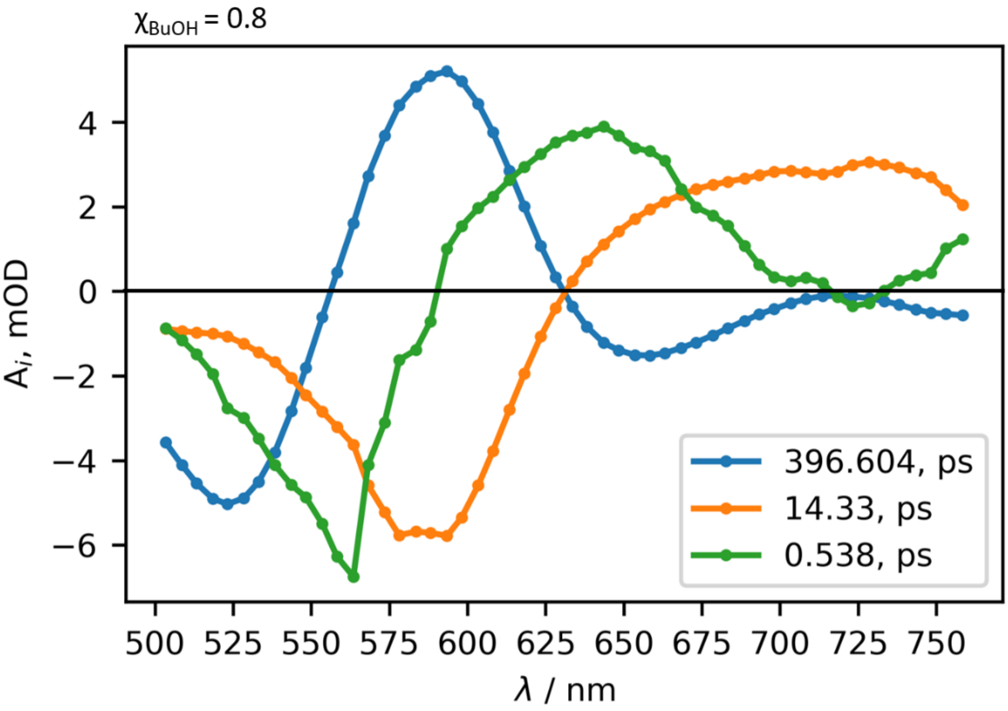

Figure A 12. Decay-associated spectra of D205 in a mixture ACN/BuOH with χBuOH = 0.8. Dashed lines represent steady-state absorption and emission.

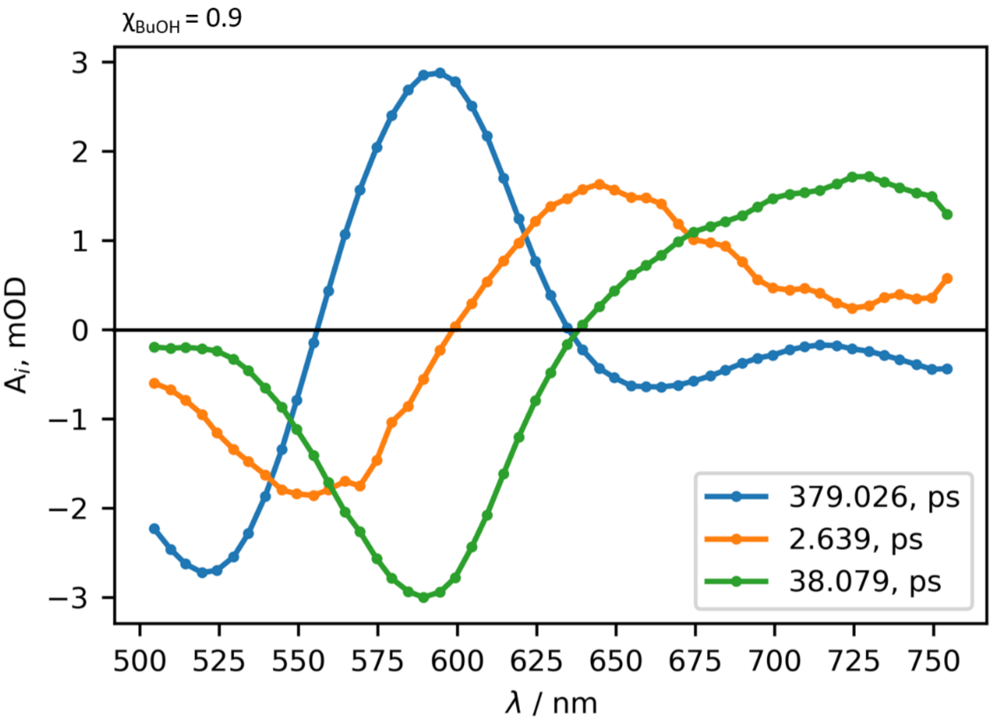

Figure A 13. Decay-associated spectra of D205 in a mixture ACN/BuOH with χBuOH = 0.9. Dashed lines represent steady-state absorption and emission.

Annex Chapter 2

GVD modified Gaussian and exponential functions convoluted with a modified Gaussian

The in-cell group velocity dispersion (GVD) is introduced based on the description provided by Ziólek *et al.* [49], [61]. This effect arises from the fact that the sample is not infinitesimally thin. As the probe pulse travels through the cell, dispersion causes different wavelengths to propagate at slightly different speeds, thereby increasing the temporal delay between the red and blue components of the probe spectrum. Consequently, the measured signal $S_{GVD}(t)$ corresponds to the sum of contributions with varying temporal delays and chirp lengths within the probe pulse.

$$S_{GVD}(t) = \frac{1}{L}\int_0^L S\left(t - \frac{x}{L}\,\tau_{GVD}\right)dx \tag{A1}$$

In Equation A1 L is the optical path length within the cell, and τ_{GVD} represents the temporal delay difference observed immediately before and after the probe pulse traverses the cell.

$$\tau_{GVD} = \frac{L}{c}\left(n_g(\lambda_{pump}) - n_g(\lambda_{probe})\right) \tag{A2}$$

Finally, Ziólek *et al.* proposed a function to the GVD-corrected Raman signal of the sample:

$$G_{GVD}(t) = G_0\, exp\left(-\frac{2.3OD}{\tau_{GVD}}\,t\right)\cdot\left[erf\left(\frac{t}{\tau} - \frac{2.3OD\,\tau}{2\,\tau_{GVD}}\right) - erf\left(\frac{t}{\tau} - \frac{2.3OD\,\tau}{2\,\tau_{GVD}} - \frac{\tau_{GVD}}{\tau}\right)\right] \tag{A3}$$

where OD is the optical density (absorbance) of the sample at the pump wavelength, and τ is related to the τ_{FWHM} of the Gaussian pulse through the expression:

$$\tau = \frac{\tau_{\mathrm{FWHM}}}{2\sqrt{\ln 2}} \tag{A4}$$

However, the analytical expression for the convolution of the exponential function with a GVD-modified Gaussian was not provided. Therefore, the integration was performed independently in the present work. For a monoexponential decay, the resulting expression is:

$$S(t) = y_0 + A_1 \cdot \sigma' \cdot \frac{\sqrt{\pi}}{2} \cdot \frac{\tau_1}{OD \cdot \tau_n \cdot \ln(10) - \tau_{GVD}} \cdot \exp\left(-\frac{(t-t_0)\cdot 2\cdot\phi}{\sigma'} + \phi^2\right) \cdot \Bigg[-\mathrm{erf}\left(\frac{\tau_{GVD}}{\sigma'} - \frac{t-t_0}{\sigma'} + \phi\right) + \mathrm{erf}\left(-\frac{t-t_0}{\sigma'} + \phi\right) - \exp\left(-\rho_1 \cdot \left(-\frac{\rho_1\cdot\sigma'^2}{4} + \tau_{GVD} - t + t_0 + \sigma' \cdot \phi\right)\right) \cdot erfc\left(\frac{-\rho_1\cdot\sigma'^2 + 2\cdot\tau_{GVD} - 2\cdot(t-t_0) + 2\cdot\sigma' \cdot\phi}{2\cdot\sigma'}\right) + \exp\left(-\rho_1 \cdot \left(-\frac{\rho_1\cdot\sigma'^2}{4} - t + t_0 + \sigma' \cdot \phi\right)\right) \cdot erfc\left(\frac{-\rho_1 \cdot\sigma'^2 - 2\cdot(t-t_0) + 2\cdot\sigma' \cdot\phi}{2\cdot\sigma'}\right)\Bigg] \tag{A5}$$

where σ' is defined as:

$$\sigma' = \frac{\tau_{\mathrm{FWHM}}}{2\sqrt{\ln 2}} \tag{A6}$$

ρ_1 is given by:

$$\rho_1 = \frac{\tau_1 \cdot OD \cdot \ln(10) - \tau_{GVD}}{\tau_1 \cdot \tau_{GVD}} \tag{A7}$$

and ϕ is defined as:

$$\phi = \frac{OD \cdot \sigma' \cdot \ln(10)}{2\cdot\tau_{GVD}} \tag{A8}$$

The fitting procedure employing up to five exponential components is available and follows the expression:

$$S(t) = y_0 + \sum_{n=1}^{n} A_n \cdot \sigma' \cdot \frac{\sqrt{\pi}}{2} \cdot \frac{\tau_n}{OD \cdot \tau_n \cdot \ln(10) - \tau_{GVD}} \cdot \exp\left(-\frac{(t-t_0)\cdot 2\cdot\phi}{\sigma'} + \phi^2\right) \cdot \Bigg[-\mathrm{erf}\left(\frac{\tau_{GVD}}{\sigma'} - \frac{t-t_0}{\sigma'} + \phi\right) + \mathrm{erf}\left(-\frac{t-t_0}{\sigma'} + \phi\right) - \exp\left(-\rho_n \cdot \left(-\frac{\rho_n\cdot\sigma'^2}{4} + \tau_{GVD} - t + t_0 + \sigma' \cdot \phi\right)\right) \cdot erfc\left(\frac{-\rho_n\cdot\sigma'^2 + 2\cdot\tau_{GVD} - 2\cdot(t-t_0) + 2\cdot\sigma' \cdot\phi}{2\cdot\sigma'}\right) + \exp\left(-\rho_n \cdot \left(-\frac{\rho_n\cdot\sigma'^2}{4} - t + t_0 + \sigma' \cdot \phi\right)\right) \cdot erfc\left(\frac{-\rho_n \cdot\sigma'^2 - 2\cdot(t-t_0) + 2\cdot\sigma' \cdot\phi}{2\cdot\sigma'}\right)\Bigg] \tag{A9}$$

The Raman contribution can also be incorporated into the GVD-modified fit. For this purpose, an expression analogous to that proposed by Ziólek *et al*. was employed:

$$S(t) = y_0 + A_R \cdot \frac{\sigma'}{\tau_{GVD}} \cdot \frac{\sqrt{\pi}}{2} \cdot exp\left(-OD \cdot \ln(10) \cdot \left(\frac{t-t_0}{\tau_{GVD}} - \frac{OD\cdot\sigma'^2 \cdot \ln(10)}{4\cdot\tau_{GVD}^2}\right)\right) \cdot \left[\mathrm{erf}\left(\frac{\tau_{GVD}}{\sigma'} - \frac{t-t_0}{\sigma'} + \frac{OD\cdot\sigma' \cdot \ln(10)}{2\cdot\tau_{GVD}}\right) - \mathrm{erf}\left(-\frac{t-t_0}{\sigma'} + \frac{OD\cdot\sigma' \cdot \ln(10)}{2\cdot\tau_{GVD}}\right)\right] \tag{A10}$$

The reliability of the function was verified by comparing the analytical expressions presented above with the numerical solution of the corresponding equations.

The parameters used in the simulation were as follows: cell thickness $L = 100$, $G_0 = 8$, t 10, $\tau_{GVD} = 100$, $t_0 = 2$, $\tau = 80$.

DMSO λ, in μm:

$$n = \sqrt{\frac{0.0442 \cdot \lambda^2}{\lambda^2 - 0.0464} + \frac{1.091 \cdot \lambda^2}{\lambda^2 - 0.01222} + 1} \quad \text{(A11)}$$

DMF λ, in nm [2]:

$$n = 2.0754 \cdot 10^{-12} \cdot \lambda^4 - 5.4485 \cdot 10^{-9} \cdot \lambda^3 + 5.4237 \cdot 10^{-6} \cdot \lambda^2 - 0.0025 \cdot \lambda + 1.8616 \quad \text{(A12)}$$

AN, TLN, MeOH, EtOH, PrOH, BuOH in μm:

$$n = c[0] + c\,[1] \cdot \lambda^{-2} + c[2] \cdot \lambda^{-4} + c[3] \cdot \lambda^{-6} \quad \text{(A13)}$$

PeOH in μm:

$$n = \sqrt{c[0] + c\,[1] \cdot \lambda^2 + c[2] \cdot \lambda^{-2} + c[3] \cdot \lambda^{-4} + c[4] \cdot \lambda^{-6}} \quad \text{(A14)}$$

Table A1. Components c[0], c[1], c[2], c[3],c[4]

Solvent	c[0]	c[1]	c[2]	c[3]	c[4]
AN	1.3321	0.0035	-0.00003	0.000002	-
TLN	1.4815	0.0042	0.0003	0.00001	-
MeOH	1.3195	0.0003	-0.00003	0.000003	-
EtOH	1.3496	0.0040	-0.00006	0.000003	-
PrOH	1.3649	0.0043	-0.00006	0.0000003	-
BuOH	1.3847	0.0050	0	0	-
PeOH	1.9543	-0.0018	0.0091	-0.0002	0.00007

Annex Chapter 3

DSSC Fabrication Process

The DSSC manufacturing process used was developed at the *Laboratoire de Réactivité et Chimie des Solides* (LRCS) in Amiens. This specific method has been refined to increase the efficiency and reproducibility of DSSCs, focusing on accurate control of materials and assembly techniques to align with the latest advances in DSSC technology.

1. Counter-Electrode Preparation

The fabrication process begins with the preparation of the counter-electrode. Using a multimeter, the conductive side of the TEC 7 glass is identified and marked for cutting. Once marked, the glass is carefully scored with a glass cutter, ensuring a precise break along the designated lines. After cutting, a small hole is drilled in the top corner of each counter-electrode using a sand-blasting machine, with the conductive side facing up during drilling. This hole will later allow for electrolyte injection into the assembled cell. Following the cutting and drilling, the counter-electrodes undergo a thorough cleaning process to eliminate any residues. The electrodes are first immersed in acetone for 15 minutes to dissolve organic contaminants, then subjected to two ultrasonic ethanol baths, each lasting 10 minutes, to ensure complete removal of impurities. After cleaning, a platinum layer is deposited by applying a few milliliters of hexachloroplatinic acid solution (H_2PtCl_6) onto the conductive side of each electrode. The electrodes are heated to 410°C for 15 minutes, decomposing the solution into platinum nanoparticles, which form a catalytic surface critical to the counter-electrode's function in the DSSC.

2. Photoanode Preparation

Preparing the photoanode involves several cleaning, treatment, and coating steps to optimize it for electron transport and dye loading. TEC 11 glass substrates are first immersed in a detergent solution and sonicated for 15 minutes to remove any contaminants. They are then rinsed with distilled water, followed by ethanol, and sonicated again in ethanol for an additional 15 minutes. After drying, the substrates are checked for residual stains to ensure no contaminants interfere with the subsequent coatings. The cleaned substrates are heated to 450°C for 30 minutes to stabilize the conductive surface, preparing it for further treatments. After cooling, a $TiCl_4$ treatment is performed by immersing the substrates in a 40 mmol/L $TiCl_4$ solution at 70°C for 30 minutes, which enhances the electron transport properties of the TiO_2 layer. Following the $TiCl_4$ treatment, a screen-printing process is used to apply three layers of 18NR-T Transparent Titania Paste (approximately 20 nm per layer) onto the substrate. Each layer is allowed to rest for 3 minutes before being heated at 170°C for 7 minutes on a hot plate, helping the TiO_2 adhere to the glass. Two additional layers of WER2-O Reflector Titania Paste (approximately 400 nm) are then printed, which enhances light scattering within the cell and increases dye loading.

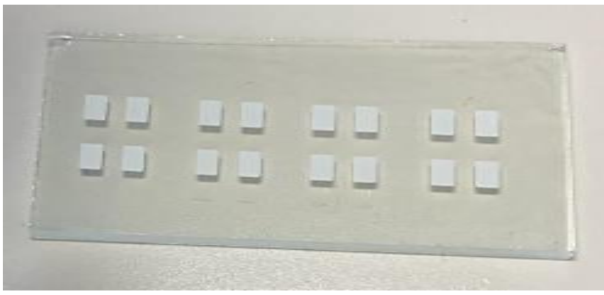

Figure A 14. Substrate after screen-printing step.

With the TiO_2 layers applied, the photoanodes are heated in stages (325°C, 375°C, 450°C, and 500°C), removing any organic additives and forming a mesoporous TiO_2 structure with a large surface area for dye adsorption. A second $TiCl_4$ treatment is performed to improve nanoparticle interconnection, which helps reduce dark current and enhances electron transport efficiency.

3. Electrolyte Solution Preparation

For the electrolyte, various chemical components are mixed in an acetonitrile and valeronitrile solution (85:15 by volume). The solution includes 500 mmol/L of tert-butylpyridine (TBP), 1 mol/L of 1,3-dimethylimidazolium iodide (DMII), 30 mmol/L of iodine (I_2), and 100 mmol/L of guanidinium thiocyanate (GuNCS). Given the hygroscopic nature of DMII and lithium iodide, they are stored in a glove box with moisture absorbers to prevent degradation and ensure solution effectiveness. This electrolyte solution is essential for regenerating the oxidized dye during cell operation, enabling continuous electron flow within the DSSC.

4. Cell Assembly

To assemble the DSSC, align the counter-electrode and photoanode with their conductive sides facing each other. A 25 μm thick Surlyn spacer is placed on the platinum-coated side of the counter-electrode, and the two electrodes are pressed together, sealing the TiO_2 and platinum layers. This assembly is briefly heated at 130°C to melt the Surlyn and bond the electrodes together. The prepared electrolyte solution is then injected into the cell through the drilled hole on the counter-electrode using a vacuum backfilling method. After filling, the hole is sealed with a small glass piece and additional Surlyn to prevent leakage. An indium/gallium alloy is then applied along the conductive inner faces of the electrodes using an ultrasonic soldering iron to enhance electrical contact. Finally, a mask with a known area (typically 0.128 cm^2) is placed over the assembled cell, preparing it for I-V measurements.

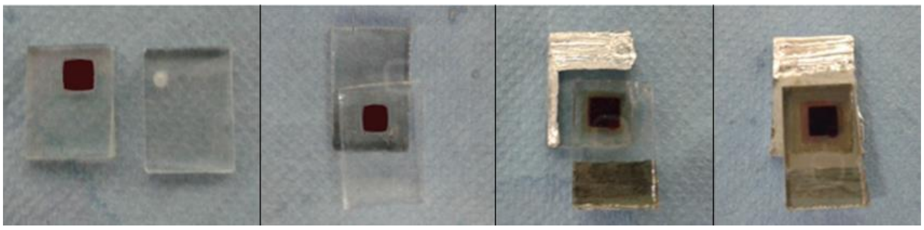

Figure A 15. Steps of assembling the electrodes into a cell.

Optical and Electrical Characterization

To measure photovoltaic performance, a black metal mask with a 0.158 cm^2 aperture was placed over the solar cells. These cells were tested under radiation at 100 mW/cm^2, generated by a 450 W xenon lamp from an Oriel solar simulator (USA). A Schott K113 Tempax sunlight filter (Prazisions Glas & Optik GmbH, Germany) was used to align the lamp's spectral output with the solar spectrum, achieving a discrepancy of less than 2%. Light intensity calibration was done using a Si reference diode with an infrared cutoff filter (KG-3, Schott). J−V curves were recorded with a Keithley 2400 source meter at a voltage scan rate of 20 mV/s.

For optical characterization, an Agilent Cary 5000 spectrophotometer was used to analyze the dye in both solution and device form. Solution measurements employed a quartz cuvette with a 1 cm light path in dual beam transmission mode, while device measurements were conducted in total transmittance mode with a 150 mm integration sphere. Background and zero adjustments were made, though external factors like glass absorption and reflection were not subtracted. Consequently, all AVT measurements reflect a comprehensive evaluation of the entire device.

Picosecond Transient Absorption Spectroscopy (TAS) Measurements

The TAS setup, optimized for picosecond resolution, was employed to study the regeneration and recombination kinetics of the dye radical cation. The setup consists of the following components: (1) a Nd laser (EKSPLA, PL2550) with a 10 Hz repetition rate and a 30 ps pulse duration, offering excitation at 532 or 355 nm. An optical parametric generator (EKSPLA, PG400) expands the excitation range to 420–2300 nm and is pumped by the Nd's third harmonic; (2) three probe systems (Hamamatsu Photonics): a Xe breakdown cell for the shortest time scales (0.5–20 ns), a Xe Flash lamp for intermediate time scales (50 ns to 2 μs), and a continuous 150 W Xe lamp for longer time scales (5 μs to 10 ms); (3) the detection unit, which includes a spectrograph (Princeton Instruments, SP2300), a high-dynamic-range streak camera (Hamamatsu Photonics, C13410) with digital readout (Hamamatsu Photonics, ORCA Flash4, C11440); (4) a delay generator (Stanford Research Systems, DG645), delay unit, and shutter control (Hamamatsu Photonics) to synchronize the setup components via HPD-TA software (Hamamatsu Photonics); and (5) optics for white light input, excitation, pump and probe shutters, a movable sample holder, and a motorized 12-position optical density filter wheel for adjusting laser pulse energy.

In TAS measurements of the DSSC, the probe light was focused perpendicularly to the sample, while the pump light was set at a 45° angle. Optical density filters (Newport or Thorlabs) were used to attenuate the probe light, which then passed through the sample. This transmitted light was directed into the spectrograph for analysis with the streak camera. The pump pulse energy in the excitation range of 810–830 nm was set to approximately 0.2 mJ. A 750 nm short pass filter (Thorlabs) was positioned before the spectrograph to block scattered pump light. Transient absorption was calculated from four streak images using the equation:

$$\Delta A = -\log\left(\frac{data - emission}{monitor - dark}\right)$$

where "data" represents the intensity when both pump and probe are active, "emission" when only the pump is active, "monitor" when only the probe is active, and "dark" when both are off, thereby correcting for stray light. Each of these four images comprised N integrated camera images, and the sequence (data, emission, monitor, dark) was repeated M times. To achieve a high signal-to-noise ratio, N was set to 500 and M to 5–10.

Intensity Modulated Photovoltage/Photocurrent Spectroscopy (IMVS/IMPS) Experiments

IMVS and IMPS are effective methods for analyzing electron transport kinetics in the photoanode and the non-geminate recombination between injected electrons in TiO_2 and the oxidized species in the electrolyte (I_3^-). These techniques operate in the frequency domain, where small amplitude light perturbations are superimposed on a continuous irradiation serving as a large bias driving force. In IMVS and IMPS measurements, a sinusoidal light perturbation of small amplitude is applied across a range of frequencies. Like in electrochemical impedance spectroscopy (EIS), the setup generally involves a primary potentiostat (PS1) equipped with a frequency response analyzer, with additional potentiostatic loops (PS2 and PS3) to manage the LED source's intensity and modulation. For enhanced accuracy, active feedback control using PS2 from a photodetector stabilizes the light intensity during measurement, while PS3 modulates the LED light intensity, which remains significantly lower than the continuous wave (cw) bias light.

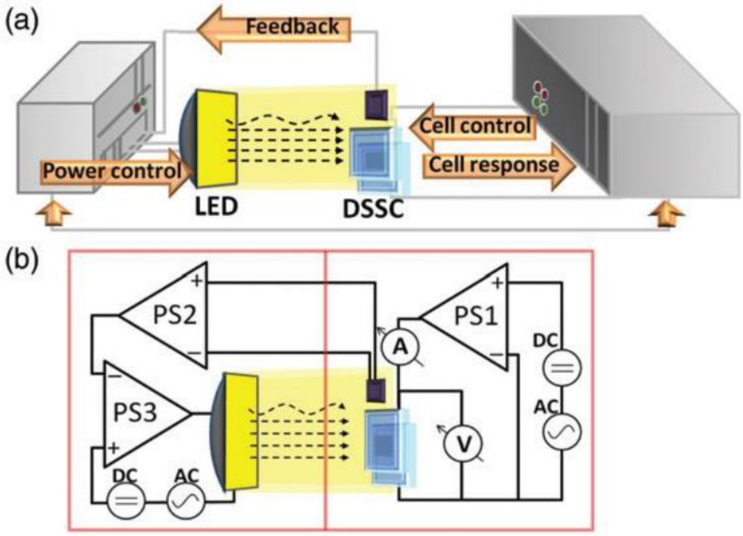

Figure A 16. Experiment for IMPS/IMVS methods: (a) schematic representation of the instrument and (b) general circuit diagram of the apparatus.PS represents a potentiostat with a built-in frequency response analyzer. The box on the right side is the master unit, and the slave unit on the left side performs small-amplitude modulation of the light intensity for IMPS/IMVS.

Kinetic data on charge transport and non-geminate recombination are acquired under two conditions: short circuit and open circuit, respectively. For a system with uniform light absorption, the quasi-Fermi level across the TiO_2 film remains constant in the open-circuit condition. In contrast, in the short-circuit condition, the Fermi level gradient across the film is represented by a curve, showing electron diffusion directly into the TCO substrate. Under short-circuit conditions, IMPS monitor the diffusion kinetics of injected electrons within the TiO_2 conduction band (CB). Under open-circuit conditions, IMVS probes the kinetics of non-geminate charge recombination.

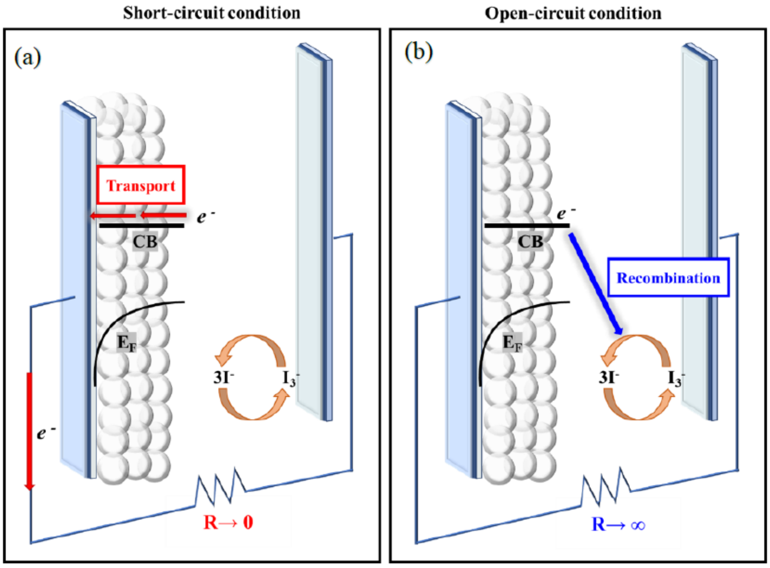

Figure A 17. Schematic representations of kinetic processes of a DSSC that are investigated via (a) intensity-modulated photocurrent spectroscopy (IMPS) under short-circuit condition and (b) intensity-modulated photovoltage spectroscopy (IMVS) under open-circuit condition. The solid arrows represent the most probable directions for electron transport (red) and charge recombination (blue) at the two extreme conditions.